Topological aspects of nodal-loop semimetals and the nature of spin-orbit coupling in $Lu_2V_2O_7$

by

Alexander Hickey

A thesis
presented to the University of Waterloo
in fulfillment of the
thesis requirement for the degree of
Master of Science
in
Physics

Waterloo, Ontario, Canada, 2021

Author's Declaration

I hereby declare that I am the sole author of this thesis. This is a true copy of the thesis, including any required final revisions, as accepted by my examiners.

I understand that my thesis may be made electronically available to the public.

Abstract

This thesis is presented in two parts: (I) understanding the topological aspects of nodal-loop semimetals in the presence of interactions and (II) exploring the nature of spin-orbit coupling in the pyrochlore oxide $Lu_2V_2O_7$. Each of these parts correspond to distinct research projects, sharing an underlying theme of topology and spin-orbit coupling.

(I) Topological nodal-loop semimetals are characterized by a symmetry protected 1D line of band touching points, dispersionless surface states, and an electromagnetic response in the form of an induced magnetization and polarization. While this characterization holds true for free fermions, there has recently been increased interest in how topological order manifests in the presence of interactions, particularly in the gapless topological semimetals. This thesis explores the effect of interactions in nodal-loop semimetals, in the framework of a mean-field BCS theory. It is found that the surface states are preserved for p-wave pairing when the gap function preserves the symmetries that protect the nodal-loop. Furthermore, it is shown that this state hosts a single Dirac mode in the core of any vortex line of odd vorticity. This result highlights that the topological order of a nodal-loop can remain stable in the presence of interactions.

(II) Pyrochlore oxides geometrically support a magnetic interaction of spin-orbit origin known as the Dzyaloshinskii-Moriya interaction, due to the lack of inversion symmetry between neighbouring magnetic ions. In magnetically ordered quantum systems, such an interaction has been shown to give rise to a thermal Hall effect of magnons, the quasiparticles arising from spin fluctuations. Such an effect was subsequently observed in thermal transport measurements of the pyrochlore oxide $Lu_2V_2O_7$, however, these measurements seem to overestimate the magnitude of the DM interaction. This draws into question the nature of spin-orbit coupling in this material. An overview of the low-energy properties of $Lu_2V_2O_7$ is presented, along with a re-investigation of the thermal transport data. This leads to an apparent discrepancy in the value of the DM interaction, motivating future investigations of this material.

Acknowledgements

I would first like to extend my sincere gratitude to my supervisors, Michel Gingras and Anton Burkov, for their consistent support and mentorship throughout my Masters' degree, despite a rather obvious inconvenience that led us to spending $\approx 75\%$ of this time corresponding remotely. I would also like to thank you both for agreeing to co-supervise me, and allowing me to pursue a wide range of research topics throughout the course of my degree.

I also thank the members of my advisory committee David Hawthorn and Roger Melko for enlightening discussions during committee meetings, and for useful feedback on this thesis at my defense. I am additionally grateful to all of the friends and colleagues that I have met in Waterloo during my studies. I am especially thankful to Daniel Lozano-Gómez, Kristian Chung, and Naman Gupta for their help in preparing for my defense.

Finally, I would like to thank my family for their support during my studies. I am particularly grateful to have spent the COVID-19 pandemic working in a makeshift home office alongside my partner Sophie and our two dogs Mocha and Luna, the best office-mates I could ask for.

Table of Contents

List of Figures

List of Abbreviations

ARPES	Angle-resolved photoemission spectroscopy
BCS	Bardeen–Cooper–Schrieffer
DFT	Density-functional theory
DM	Dzyaloshinsky-Moriya
FCC	Face-centered cubic

Part I

Topological aspects of nodal-loop semimetals

Chapter 1

Introduction

Up until the 1980's, condensed matter physicists had largely focused on classifying quantum phases of matter within the Landau paradigm – the spontaneous breaking of symmetries. For example, a ferromagnet breaks the rotational symmetry of an electronic spin by selecting a direction of magnetization [1]. Since then, there has been an exceeding interest in quantum matter that does not fit within this classification [2–4]. Rather than arising from symmetry considerations, described by a local order parameter, these materials develop non-local order described by topological invariants, that remain robust to local deformations of the system at hand. These so-called topological phases of matter can exhibit peculiar transport properties, localized edge states, fractionalized excitations, and long-range entanglement [5].

For many years, the study of topological phases was focused on materials that are characterized by both a gapped bulk spectrum, and gapless states localized to the surface. These surface states are guaranteed by a topological invariant, and are robust: they remain in the presence of perturbations, so long as the bulk gap does not close [6]. These so-called topological insulators are distinct from trivial insulators, as they are topologically distinct from the vacuum.

Subsequently, it was discovered that there are similar topological aspects in gapless systems, exhibiting nontrivial topological invariants and robust surface states. This has led to the identification of a new class of gapless phases of matter, known as topological semimetals [7]. These materials are characterized by a stable Fermi surface originating from a crossing of energy bands. In three dimensions (3D) the Fermi surface manifests as either point-nodes, corresponding to either Weyl or Dirac semimetals, or as line-nodes, corresponding to a nodal-loop semimetal.

Recently, there has been theoretical effort to move away from the characterization of topological phases using conventional band theory, which relies on the assumption that the many-body ground state of a non-interacting system can be viewed at the single-particle level. This is key to understanding how topological order manifests in interacting many-body systems, where the conventional band theory breaks down. In the case of a Weyl semimetal for example, it was recently shown that the band touching points can be gapped in the presence of strong interactions, while preserving topological order [8]. This topological order manifests in the electromagnetic response, leading to a 3D generalization of the fractional quantum Hall effect.

This motivates the question as to whether other topological phases of matter can remain robust in the presence of interactions. The first part of this thesis explores this question for the case of a nodal-loop semimetal, where the topological order manifests in the form of dispersionless surface states [9], and an electromagnetic response in the form of magnetization and polarization [10].

Part I of this thesis is outlined as follows. Chapter 2 outlines various aspects of topological band theory, including key terms and definitions, as well as a brief overview of topological insulators and topological semimetals. Chapter 3 details various properties of nodal-loop semimetals. In particular, Sec. 3.1 focuses on deriving a nodal-loop model from a topological insulator multilayer system in the presence of a magnetic field. The remaining sections focus on the topological aspects of a nodal-loop semimetal protected by a mirror symmetry. Chapter 4 considers the effect of introducing interactions to a nodal-loop semimetal, in the framework of a mean-field BCS theory, with an overarching goal of understanding the topological aspects of such a system. It is shown in Sec. 4.2 that s-wave pairing only gaps the nodal-loop in the limit of strong coupling, which corresponds to a trivial superconductor. Conversely, a chiral p-wave pairing term fully gaps the bulk at weak pairing while preserving the symmetries protecting the nodal-loop. Section 4.3 then extends the chiral p-wave state to include the presence of vortices, where it is shown that a vortex line hosts a single gapless Dirac mode, protected by the symmetries of the nodal-loop. These results highlight that the topological aspects of a nodal-loop semimetal can remain stable in the presence of interactions. Chapter 5 summarizes these results, and provides direction for future work.

Chapter 2

Aspects of topological band theory

This chapter provides an overview of some key aspects of topological band theory that is used throughout this thesis. Section 2.1 is a brief introduction to the Berry phase, which gives rise to an emergent geometry an underpins most topological phenomena. Section 2.2 is an introduction and overview to topological insulators. Finally, Sec. 2.3 is an introduction to the gapless topological phases, known as a topological semimetals.

2.1 Berry phase and an emergent geometry

The most general formulation of the Berry phase is to consider a system described by a time-dependent Hamiltonian $H(\boldsymbol{k})$, which depends on time implicitly by a set of parameters $k^\mu = k^\mu(t)$, and ask how the system evolves in the adiabatic approximation (over large timescales) [11]. Consider the orthonormal basis $\{|E_n(\boldsymbol{k})\rangle\}$ consisting of the instantaneous eigenstates of $H(\boldsymbol{k})$, given by solutions of the eigenvalue equation

$$H(\boldsymbol{k}(t))\,|E_n(\boldsymbol{k}(t))\rangle = E_n(\boldsymbol{k}(t))\,|E_n(\boldsymbol{k}(t))\rangle. \tag{2.1}$$

In the case where the energy is non-degenerate, which is assumed moving forward, this equation determines the eigenstates up to an overall phase factor. In this sense, the system has a $U(1)$ gauge symmetry. Next, suppose that the system is prepared in an initial eigenstate $|\psi(0)\rangle \equiv |E_n(\boldsymbol{k}(0))\rangle$. Generically, $\boldsymbol{k}(t)$ changes as time evolves, however, the adiabatic theorem states that the system will remain in an instantaneous eigenstate of $H(\boldsymbol{k}(t))$ [12]. The phase of this eigenstate however, is free to change as a function of time, so we have

$$|\psi(t)\rangle = e^{-i\theta(t)}\,|E_n(\boldsymbol{k}(t))\rangle. \tag{2.2}$$

Note that for the remainder of Part I of this thesis, it is assumed that we are working in units where $\hbar = 1$. Plugging Eq. (2.2) into the time-dependent Schrödinger equation

$$i \frac{\mathrm{d}}{\mathrm{d}t} |\psi(t)\rangle = H(\boldsymbol{k}(t)) |\psi(t)\rangle, \tag{2.3}$$

and multiplying by $\langle E_n(\boldsymbol{k}(t))|$ from the left, we obtain a differential equation for the time-evolution of the phase

$$\frac{\mathrm{d}}{\mathrm{d}t} \theta(t) = E_n(\boldsymbol{k}(t)) - i \langle E_n(\boldsymbol{k}(t))| \frac{\mathrm{d}}{\mathrm{d}t} |E_n(\boldsymbol{k}(t))\rangle. \tag{2.4}$$

Integrating Eq. (2.4), we get

$$\theta(t) = \int_0^t \mathrm{d}t' \, E_n(\boldsymbol{k}(t')) - i \int_0^t \mathrm{d}t' \, \langle E_n(\boldsymbol{k}(t'))| \frac{\mathrm{d}}{\mathrm{d}t'} |E_n(\boldsymbol{k}(t'))\rangle. \tag{2.5}$$

The first term on the right side of Eq. (2.5) corresponds to the standard dynamical phase, whereas the second term corresponds to the Berry phase, defined as

$$\gamma_n = -i \int_0^t \mathrm{d}t' \, \langle E_n(\boldsymbol{k}(t'))| \frac{\mathrm{d}}{\mathrm{d}t'} |E_n(\boldsymbol{k}(t'))\rangle. \tag{2.6}$$

Because the time-dependence enters implicitly in the system parameters, it can be effectively eliminated as

$$\gamma_n = -i \int_0^t \mathrm{d}t' \, \frac{\mathrm{d}k^\mu}{\mathrm{d}t'} \langle E_n(\boldsymbol{k}(t'))| \frac{\partial}{\partial k^\mu} |E_n(\boldsymbol{k}(t'))\rangle = -i \int_C \mathrm{d}k^\mu \, \langle E_n(\boldsymbol{k})| \frac{\partial}{\partial k^\mu} |E_n(\boldsymbol{k})\rangle, \tag{2.7}$$

where C is the path in parameter space traced out by evolving $\boldsymbol{k}$ in time. This expression takes the same form as the phase acquired by an electron moving in a magnetic field [13]. Following this analogy, we may define an effective vector potential, known as the *Berry connection*, as

$$A_\mu(\boldsymbol{k}) = -i \langle E_n(\boldsymbol{k})| \frac{\partial}{\partial k^\mu} |E_n(\boldsymbol{k})\rangle. \tag{2.8}$$

This quantity is not gauge invariant however, as under a $U(1)$ transformation of the eigenstate $|E_n(\boldsymbol{k})\rangle \to e^{-i\chi(\boldsymbol{k})} |E_n(\boldsymbol{k})\rangle$, the Berry connection transforms as

$$A_\mu(\boldsymbol{k}) \to A_\mu(\boldsymbol{k}) + \frac{\partial \chi}{\partial k^\mu}. \tag{2.9}$$

The Berry phase is then modified by a factor

$$\Delta\gamma = \int_C \mathrm{d}k^\mu \frac{\partial\chi}{\partial k^\mu}, \tag{2.10}$$

which at first glance vanishes for any smooth function $\chi(\boldsymbol{k})$, whenever C is a closed path in parameter space. For many years, it was thought that the Berry phase could always be eliminated by a clever choice of gauge transformation. It was pointed out by Berry however [14], that the wavefunction can remain single-valued over a closed path C, so long as the Berry phase is an integer multiple of 2π, i.e.

$$\gamma = \oint_C \mathrm{d}k^\mu A_\mu(\boldsymbol{k}) = 2\pi m \tag{2.11}$$

for some integer m, which was subsequently shown to result in observable phenomena such as the Aharonov-Bohm effect [15].

Often times, it is convenient to work with the gauge invariant *Berry curvature*, defined as

$$F_{\mu\nu}(\boldsymbol{k}) \equiv \frac{\partial A_\mu}{\partial k^\nu} - \frac{\partial A_\nu}{\partial k^\mu}. \tag{2.12}$$

This expression is analogous to the Riemann curvature tensor in the theory of differential geometry, which describes the curvature of the local geometry of a manifold. By analogy, the Berry curvature can be viewed as a manifestation of geometric properties of the eigenstates in the parameter space spanned by $\{\boldsymbol{k}\}$. The topological properties (the properties that remain invariant under smooth deformations) of this emergent geometry are the essence of topological band theory [16].

While up to this point, we have assumed that the vector $\boldsymbol{k}$ is some collection of generalized system parameters, it is usually the case in condensed matter systems that $\boldsymbol{k}$ is simply the crystal momentum of Bloch waves, spanning the first Brillouin zone. It is assumed that this is the case for the remainder of this thesis. The formalism developed in this chapter is used throughout this thesis to understand various phenomena related to topological phases of matter. Arguably the simplest class of such materials, known as topological insulators, is explored in the following section.

2.2 Topological insulators

A topological insulator is a material that has both a fully gapped bulk spectrum and gapless states localized to the edge of the material. These edge states are generally protected by a

set of symmetry operations, and they cannot be gapped by perturbations that do not break these symmetries, making them a robust property of the material. Topological insulators are considered topologically distinct from a so-called trivial insulator, as it is impossible to adiabatically transform the underlying Hamiltonian to a vacuum[1] without first closing the energy gap.

Perhaps the simplest example of a topological insulator is a 2D Chern insulator [6], which is an insulator with broken time-reversal symmetry, characterized by a nonzero $\mathbb{Z}$ topological invariant:

$$C = \frac{1}{2\pi} \int_{\text{BZ}} \mathrm{d}^2k \, F_{xy}(\boldsymbol{k}), \tag{2.13}$$

where the integral is taken over the first Brillouin zone, and $F_{xy}(\boldsymbol{k})$ is the Berry curvature defined in Eq. (2.12) for the valence band of the insulator. This topological invariant is closely linked to a measurable quantity: the Hall conductivity. In particular, a Chern insulator gives rise to a quantized electromagnetic response, in the form of the integer quantum Hall effect, with Hall conductivity $\sigma_{xy} = \frac{e^2}{h} C$ [17].

There are also examples of time-reversal invariant topological insulators, such as graphene in the presence of spin-orbit coupling [18]. Such a model is fully gapped in the bulk, but gives rise to equal and opposite Chern numbers $C = \pm 1$ for the two spin degrees of freedom. There is a $\mathbb{Z}_2$ topological invariant in this case, corresponding to the difference in Chern numbers for the different spin components, which is either zero or not. Analogous to the Chern insulator, there is an anomalous Hall effect, with Hall conductivity $\sigma_{xy} = \pm \frac{e^2}{h}$ of opposite sign for each spin component. This is known as the quantum spin Hall effect [18].

For several decades after the discovery of the integer quantum Hall effect, it was thought that topological insulators were merely a phenomenon of two-dimensions. Subsequent to the discovery of the quantum spin Hall effect in 2005 [19], 3D analogues of the quantum spin Hall state, protected by time-reversal symmetry, were predicted [20, 21]. They can be separated into two classes: weak and strong topological insulators. Weak topological insulators are distinct in the sense that they can be decoupled into a stack of 2D topological insulators, and are therefore not robust in the presence of disorder. Topological insulators in 3D are generically gapped in the bulk, and exhibit Dirac cone states on the 2D surface [22]. Weak topological insulators always exhibit an even number of Dirac cones on the surface, while strong topological insulators can harbour isolated Dirac cone surface states. An example of a strong topological insulator is Bi_2Se_3, where a single Dirac cone surface

---

[1] Here, the vacuum refers to a system with an infinite energy gap between valence and conduction bands, such that particle-hole excitations are no longer possible.

state was observed using angle-resolved photoemission spectroscopy (ARPES), governed by the low-energy Hamiltonian [23]

$$H(\boldsymbol{k}_\perp) = v_F(\hat{\boldsymbol{z}} \times \boldsymbol{\sigma}) \cdot \boldsymbol{k}_\perp, \tag{2.14}$$

where v_F is the velocity of the Dirac fermion, $\boldsymbol{\sigma}$ is a triplet of Pauli matrices, and $\boldsymbol{k}_\perp = (k_x, k_y)$ is the crystal momenta of the surface Brillouin zone. ARPES is the experimental method generally used to find evidence of topological insulators, as it directly probes for the metallic surface states and consequently, the topological invariants.

The correspondence between topological invariants and the existence of surface states is generic across many topological phases of matter. This principle is called the *bulk-boundary correspondence* [24], and holds for each of the topological insulators described in this section.

For many years after the discovery of topological phases of matter, much of the focus in this field was directed to understanding phenomena in gapped electronic systems. Recently however, interesting connections to topological order in gapless systems has been identified. For example, the surfaces of a 3D topological insulator exhibit gapless Dirac cones, analogous to a 2D semimetal. The transition between such a topological insulator and a trivial insulator passes through an intermediate phase that is gapless in the bulk [21], with low energy excitations governed by the 3D Dirac equation. If time-reversal or inversion symmetry is broken, this Dirac point splits into an even number of stable band touching points [25]. This is an example of a topological semimetal (specifically a Weyl semimetal), which is explored in more detail in the following section.

2.3 Topological semimetals

Topological semimetals are gapless electronic phases that exhibit topologically stable (subject to symmetry constraints) band crossings [9]. Various topological semimetals are distinguished by the dimensionality of band crossings (i.e. point-nodes or line-nodes), the degeneracy of band crossings, and the symmetries which protect the stable band crossing [25]. In 3D, the point-node semimetals are generally classified in terms of their low-energy excitations, corresponding to either Dirac or Weyl fermions [7].

As descried briefly in Sec. 2.2, a Dirac semimetal can arise as an intermediate phase between a 3D topological and trivial insulator [21], where the low-energy excitations correspond to the massless Dirac Hamiltonian in 3D , given by [26]

$$H(\boldsymbol{k}) = \begin{pmatrix} v_F \boldsymbol{k} \cdot \boldsymbol{\sigma} & 0 \\ 0 & -v_F \boldsymbol{k} \cdot \boldsymbol{\sigma} \end{pmatrix}. \tag{2.15}$$

This can equivalently be viewed as two copies of a 3D Hamiltonian describing Weyl fermions of opposite chirality, given by

$$H_{\pm}(\boldsymbol{k}) = \pm v_F \boldsymbol{k} \cdot \boldsymbol{\sigma}. \qquad (2.16)$$

These two copies of Weyl points arise necessarily at the same point in the first Brillouin zone from the presence of both time-reversal and inversion symmetries [25]. By breaking at least one of these symmetries however, the two Weyl points become stable and separate in momentum space. In the case where time-reversal symmetry is broken, it is guaranteed that there is at least two Weyl points, while when inversion symmetry is broken, there is at least four [25]. These Weyl points always appear in pairs, such that the net chirality vanishes. An example of the spectrum for a Weyl semimetal with two Weyl points is depicted in Fig. 2.1. Weyl nodes are robust are extraordinarily robust, they may only be removed by a perturbation large enough to bring two nodes of opposite chirality to the same point in momentum space. Furthermore, Weyl semimetals exhibit Fermi arc surface states, corresponding to a line of surface states connecting the projection of the two nodes on the surface Brillouin zone.

In 3D, another type of topological semimetal exists, which has band touching points in the form of a line. Topological line-nodes have continuous lines of band touching points that form a closed loop in the first Brillouin zone, an example of such a spectrum is depicted in Fig. 2.2. While Weyl nodes are generically stable, line-nodes are not. Imposing certain discrete symmetries, however, can stabilize line nodes, and they remain stable with respect to all perturbations that do not violate these symmetries [27]. These are referred to as nodal-loop semimetals, and are the subject of Chapters 3 and 4 of this thesis.
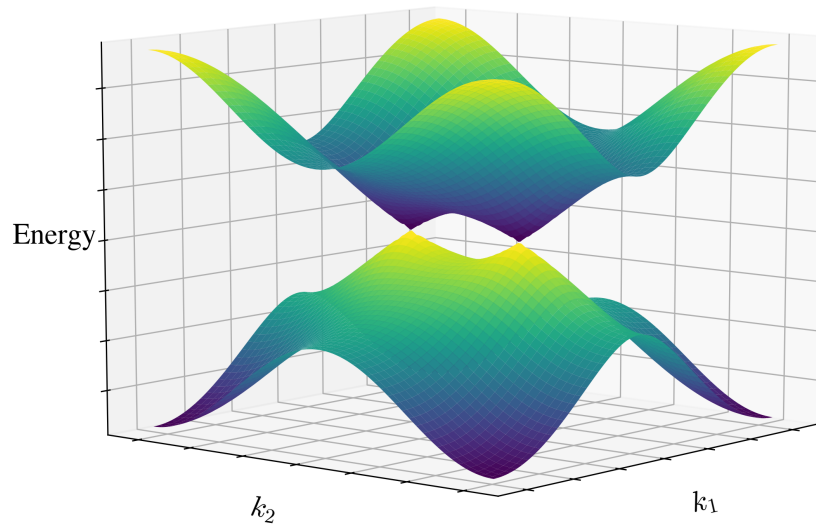
Figure 2.1: Example of the spectrum for a Weyl semimetal with broken time-reversal symmetry, where the two bands touch at isolated points in the first Brillouin zone. The vertical axis corresponds to energy in arbitrary units, while the in plane axes correspond to two of the three crystal momentum components.
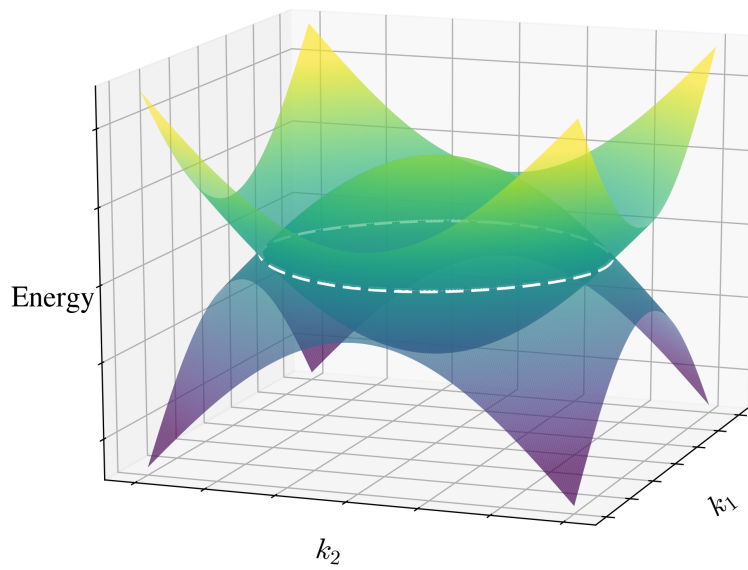
Figure 2.2: Example of the spectrum for a nodal-loop semimetal, where the two bands touch along a continuous closed line first Brillouin zone. The loop of band touching points is depicted by the white dashed line. The vertical axis corresponds to energy in arbitrary units, while the in plane axes correspond to two of the three crystal momentum components.

Chapter 3

Nodal-loop semimetals

This chapter motivates and outlines some of they key topological aspects of nodal-loop semimetals. Section 3.1 motivates a minimal model for a nodal-loop semimetal in the presence of spin-orbit coupling. Section 3.2 subsequently discusses in detail the symmetries that stabilize this nodal-loop. Section 3.3 and Sec. 3.4 outline the topological aspects of nodal-loop semimetals, including topological invariants, surface states, and the associated electromagnetic response. Section 3.5 describes a connection between the minimal nodal-loop model and a 2D Fermi liquid. This is found to be particularly useful to motivate the calculation of vortex core states in Sec. 4.3. Finally, Sec. 3.6 is an overview of the current experimental evidence for candidate nodal-loop materials.

3.1 Model of a nodal-loop semimetal

With the qualitative picture of a nodal-loop semimetal in Sec. 2.3, we now look at how a nodal-loop model may be realized. This section outlines a derivation of the first theoretically proposed model of a topological nodal-loop, which emerges from a topological insulator multi-layer system [9, 28, 29].

The starting point for this model is to consider a slab of 3D topological insulator material in the $xz-$plane, with finite extent in the $y-$direction. We assume that that the surface states of this insulator correspond to massless Dirac fermions, such as those observed in Bi_2Se_3 [23], described by the Hamiltonian

$$H_\pm(\boldsymbol{k}_\perp) = \pm v_F(\hat{\boldsymbol{y}} \times \boldsymbol{\sigma}) \cdot \boldsymbol{k}_\perp, \tag{3.1}$$
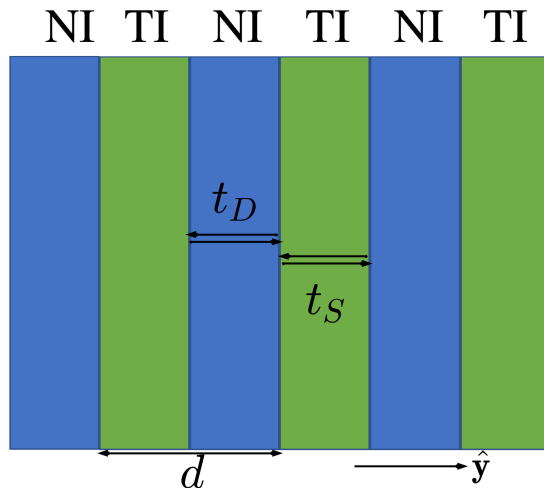
Figure 3.1: Schematic of the topological insulator (TI) - normal insulator (NI) multilayer system described by Eq. (3.3), by stacking thin films along the $y-$axis. The tunneling amplitude between surface states of the same (neighbouring) topological insulator(s) is t_S (t_D).

where v_F is the velocity of the Dirac fermion, $\hat{\boldsymbol{y}}$ is the unit vector in the $y-$direction, and $\boldsymbol{k}_\perp = (k_x, k_z)$ is the crystal momentum in the surface Brillouin zone. The sign appearing in front of Eq. (3.1) flips under a reflection about the $xz-$plane, and thus describes the surface states of the top and bottom surfaces respectively. By including an additional degree of freedom to account for the top and bottom surfaces of the thin film, we may write Eq. (3.1) more compactly as

$$H(\boldsymbol{k}_\perp) = v_F \tau_z (\hat{\boldsymbol{y}} \times \boldsymbol{\sigma}) \cdot \boldsymbol{k}_\perp. \tag{3.2}$$

Here, $\boldsymbol{\tau} \equiv (\tau_x, \tau_y, \tau_z)$ denote the Pauli matrices acting on the top/bottom surface degree of freedom. The Hamiltonian in Eq. (3.2) thus describes the top and bottom surface states of a single topological insulator slab.

Next, we may form a topological insulator multi-layer by stacking these thin films with spacer layers consisting of a normal (i.e. trivially) insulating material. Assuming that the normal insulator layers are sufficiently thin, we may assume that states on the surface of a topological insulator can tunnel to a neighbouring surface. A schematic of this multilayer

system is depicted in Fig. 3.1, and is described by the tight-binding Hamiltonian

$$H = \sum_{\boldsymbol{k}_\perp, i, j} c_{\boldsymbol{k}_\perp, i}^\dagger \left[v_F \tau_z (\hat{\boldsymbol{y}} \times \boldsymbol{\sigma}) \cdot \boldsymbol{k}_\perp \delta_{i,j} + t_S \tau_x \delta_{i,j} + \frac{1}{2} t_D \tau_+ \delta_{i+1,j} + \frac{1}{2} t_D \tau_- \delta_{i-1,j} \right] c_{\boldsymbol{k}_\perp, j}, \quad (3.3)$$

where the i, j indices label the topological insulator layers along the $y-$direction, and t_S (t_D) correspond to the tunneling amplitude between surfaces of the same (different) topological insulator layer. The first term in Eq. (3.3) corresponds to the top and bottom surface states of a single topological insulator layer. The second term corresponds to the tunneling process between the top and bottom surface states of the same topological insulator, with the τ_x operator accounting for the surface degree of freedom. The remaining terms correspond to tunneling between different topological insulator layers. For simplicity, we set the distance between two topological insulator layers to unity, $d = 1$. Carrying out a Fourier transform of Eq. (3.3) along the multi-layer growth direction $\hat{\boldsymbol{y}}$, we get

$$H = \sum_{\boldsymbol{k}} c_{\boldsymbol{k}}^\dagger \left[v_F \tau_z \left(-k_x \sigma_z + k_z \sigma_x \right) + (t_S + t_D \cos k_y) \tau_x - t_D \sin k_y \tau_y \right] c_{\boldsymbol{k}}, \quad (3.4)$$

where $\boldsymbol{k} = (k_x, k_y, k_z)$ is the crystal momentum of the full 3D Brillouin zone.

Next, we consider the effect of the spins coupling to an external field via a Zeeman term $\boldsymbol{b} \cdot \boldsymbol{\sigma}$. For now, we assume that the field lies in the plane of the topological insulator thin film $\boldsymbol{b} = b\hat{\boldsymbol{z}}$, and the effect of an out of plane field is discussed in Sec. 3.2. The Hamiltonian for a fixed value of $\boldsymbol{k}$ is then given by

$$H(\boldsymbol{k}) = -v_F k_x \tau_z \sigma_z + v_F k_z \tau_z \sigma_x + (t_S + t_D \cos k_y) \tau_x - t_D \sin k_y \tau_y + b\sigma_z. \quad (3.5)$$

Performing a canonical transformation, consisting of the similarity transformation

$$\sigma_\pm \to \tau_z \sigma_\pm \qquad \tau_\pm \to \tau_\pm \sigma_z, \quad (3.6)$$

followed by a rotation of the spin quantization axes

$$\sigma_x \to \sigma_y \qquad \sigma_y \to \sigma_z \qquad \sigma_z \to \sigma_x, \quad (3.7)$$

brings Eq. (3.5) to the form

$$H(\boldsymbol{k}) = \left[-v_F k_x \tau_z + (t_S + t_D \cos k_y) \tau_x - t_D \sin k_y \tau_y + b \right] \sigma_x + v_F k_z \sigma_y. \quad (3.8)$$

Note that the canonical transformation amounts to a change of basis in the full four-dimensional Hilbert space. This Hamiltonian is then readily block-diagonalized to the form $H(\boldsymbol{k}) = H_-(\boldsymbol{k}) \oplus H_+(\boldsymbol{k})$, where

$$H_\pm(\boldsymbol{k}) = m_\pm(\boldsymbol{k})\sigma_x + v_F k_z \sigma_y \quad (3.9)$$

14

and
$$m_{\pm}(\boldsymbol{k}) \equiv b \pm \sqrt{(t_S + t_D \cos k_y)^2 + t_D^2 \sin^2 k_y + v_F^2 k_x^2}. \tag{3.10}$$

Assuming that $b > 0$, any information about the band touching points is fully contained in the $H_-(\boldsymbol{k})$ block of Eq. (3.9). To be more precise, there is a two-fold degeneracy in the first Brillouin zone, at $k_z = 0$ and any solution to the equation $m_-(\boldsymbol{k}) = 0$. Generically, this equation relates two of the three crystal momentum components, and thus describes a one-dimensional line-node. To further simplify, assume that $t_D = -t_S \equiv v_F$ for convenience. In this case the band touching points, where the coefficients of Eq. (3.9) vanish, are depicted in Fig. 3.2. We see from Fig. 3.2 that the line-node forms a closed loop in the $xy-$plane, i.e. a nodal-loop. Setting $m_-(\boldsymbol{k}) = 0$ and expanding around small $\boldsymbol{k}$, we find that there is a circular nodal-loop defined by $k_z = 0$ and

$$k_x^2 + k_y^2 = \frac{b^2}{v_F^2}.$$

While this specific model of a nodal-loop semimetal may seem fine tuned, it is worth noting that these specific parameter choices were chosen out of convenience. For example, choosing $t_D \neq v_F$ leaves the nodal-loop intact, and makes it approximately elliptical. In fact, the precise functional form of $m_-(\boldsymbol{k})$ is unimportant, and describes a nodal-loop semimetal as long as the equation $m_-(\boldsymbol{k}) = 0$ describes a closed loop in the first Brillouin zone at $k_z = 0$. Because of this, it is convenient for the rest of this thesis to choose a simpler functional form of a nodal-loop model, which we take to be the lattice model given by

$$H_0(\boldsymbol{k}) = \left(Q^2 - 3 + \cos k_x + \cos k_y + \cos k_z\right)\sigma_x + v_F \sin k_z \sigma_y. \tag{3.11}$$

By setting $Q = b/v_F$, this model reproduces the same low-energy theory as Eq. (3.9), describing a circular nodal-loop in the $xy-$plane of radius Q. A more detailed discussion of the stability of a nodal-loop is discussed in Sec. 3.2.

3.2 Symmetry considerations

With an explicit minimal model for a nodal-loop semimetal motivated in Sec. 3.1, it is now important to address whether such a configuration is stable or fine-tuned. To do so, we can first look at the band touching points from a very general point of view, following the

15
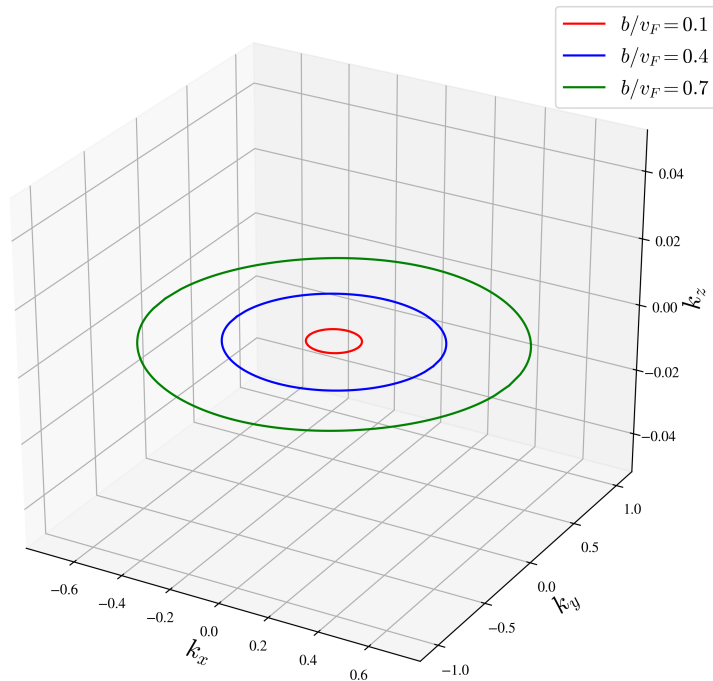
Figure 3.2: Plot of the band touching points for the $H_-(\boldsymbol{k})$ block of Eq. (3.9) for $t_D = -t_S = v_F$. The line-node is plotted for various values of b/v_F, and forms a closed loop in momentum space, i.e. a nodal-loop.

argument in Ref. [9]. A minimal two-band model can always be written in the form [1]

$$H(\boldsymbol{k}) = h_0(\boldsymbol{k}) + h_1(\boldsymbol{k})\sigma_x + h_2(\boldsymbol{k})\sigma_y + h_3(\boldsymbol{k})\sigma_z, \qquad (3.12)$$

and the corresponding dispersion is given by the two bands

$$E_\pm(\boldsymbol{k}) = h_0(\boldsymbol{k}) \pm \sqrt{h_1^2(\boldsymbol{k}) + h_2^2(\boldsymbol{k}) + h_3^2(\boldsymbol{k})}. \qquad (3.13)$$

---

[1]Any two-band model can be written in this general form as the Pauli matrices form a basis for Hermitian operators on a two-dimensional Hilbert space. In this case, the operators act on the degree of freedom corresponding to the two energy eigenstates at each value of the crystal momentum.

The two bands therefore touch whenever $h_1(\boldsymbol{k}) = h_2(\boldsymbol{k}) = h_3(\boldsymbol{k}) = 0$ for some crystal momentum $\boldsymbol{k}$. In 3D, the solution to $h_1(\boldsymbol{k}) = 0$ generically corresponds to a 2D surface, the solution to $h_1(\boldsymbol{k}) = h_2(\boldsymbol{k}) = 0$ generically corresponds to a 1D line, and the solution to $h_1(\boldsymbol{k}) = h_2(\boldsymbol{k}) = h_3(\boldsymbol{k}) = 0$ generically corresponds to a collection of zero-dimensional points, i.e. Weyl nodes. This implies that point-nodes are generic in 3D, without enforcing specific crystallographic symmetries, while line-nodes are not. In particular, a line-node can only be stable to the addition of perturbations if there is a crystallographic symmetry, in addition to the translational symmetry, enforcing that only two of the three Pauli operators appear in Eq. (3.12).

Returning back to the topological insulator multilayer model in Eq. (3.4), we can understand the symmetries protecting the nodal-loop by repeating the derivation of the effective model in the case where the spin-splitting field $\boldsymbol{b}$ has components in the direction of the crystal growth axis. In this case, the presence of a spin-splitting term $\boldsymbol{b} \cdot \boldsymbol{\sigma}$ explicitly breaks time-reversal symmetry. We introduce an angle θ that measures the canting of the spin-splitting field away from the multilayer planes, such that

$$\boldsymbol{b} = b \cos \theta \hat{\boldsymbol{z}} + b \sin \theta \hat{\boldsymbol{y}}. \tag{3.14}$$

In this case, the multilayer model Eq. (3.4) becomes

$$H(\boldsymbol{k}) = -v_F k_x \tau_z \sigma_z + v_F k_z \tau_z \sigma_x + (t_S + t_D \cos k_y)\, \tau_x - t_D \sin k_y \tau_y + b \cos \theta \sigma_z + b \sin \theta \sigma_y. \tag{3.15}$$

Next, we rotate the spin quantization axis to be parallel with the applied field

$$\sigma_x \to \sigma_x \qquad \sigma_y \to \cos \theta \sigma_y + \sin \theta \sigma_z \qquad \sigma_z \to -\sin \theta \sigma_y + \cos \theta \sigma_z, \tag{3.16}$$

which brings the Hamiltonian to

$$H(\boldsymbol{k}) = v_F k_z \tau_z \sigma_x + v_F k_x \sin \theta \tau_z \sigma_y - v_F k_x \cos \theta \tau_z \sigma_z + (t_S + t_D \cos k_y)\, \tau_x - t_D \sin k_y \tau_y + b \sigma_z. \tag{3.17}$$

Performing the same canonical transformation as in Eq. (3.6) and Eq. (3.7), consisting of the similarity transformation

$$\sigma_\pm \to \tau_z \sigma_\pm \qquad \tau_\pm \to \tau_\pm \sigma_z, \tag{3.18}$$

followed by a rotation of the spin quantization axes

$$\sigma_x \to \sigma_y \qquad \sigma_y \to \sigma_z \qquad \sigma_z \to \sigma_x, \tag{3.19}$$

17

brings Eq. (3.17) to the form

$$H(\boldsymbol{k}) = [b - v_F k_x \cos\theta\tau_z + (t_S + t_D \cos k_y)\,\tau_x - t_D \sin k_y \tau_y]\,\sigma_x + v_F k_z \sigma_y + v_F k_x \sin\theta\sigma_z.$$
(3.20)

This Hamiltonian can subsequently be block-diagonalized to the form $H(\boldsymbol{k}) = H_-(\boldsymbol{k}) \oplus H_+(\boldsymbol{k})$, where

$$H_\pm(\boldsymbol{k}) = \tilde{m}_\pm(\boldsymbol{k})\sigma_x + v_F k_z \sigma_y + v_F k_x \sin\theta\sigma_z,$$
(3.21)

and

$$\tilde{m}_\pm(\boldsymbol{k}) \equiv b \pm \sqrt{(t_S + t_D \cos k_y)^2 + t_D^2 \sin^2 k_y + v_F^2 \cos^2\theta k_x^2}.$$
(3.22)

The last two terms in Eq. (3.21) vanish when $k_x = k_z = 0$, in which case the band touching points can be solved for by setting $\tilde{m}_-(\boldsymbol{k}) = 0$, which has no solution for any $b \neq 0$. The nodal-loop is therefore gapped for any field with $\theta \neq 0$ with a component in the multilayer growth direction. This can be understood by noting that when $\theta = 0$, the spin-splitting field lies perpendicular to a mirror plane, whereas when $\theta \neq 0$ this is no longer the case. This implies that the crystallographic symmetry protecting the nodal-loop is a mirror/reflection symmetry. Indeed, such a symmetry is present in nodal-loop models Eq. (3.9) and Eq. (3.11), given by

$$\sigma_x H(\mathcal{R}_z \boldsymbol{k})\sigma_x = H(\boldsymbol{k}),$$
(3.23)

where $\mathcal{R}_z \boldsymbol{k} \equiv (k_x, k_y, -k_z)$. This corresponds to a mirror/reflection symmetry about the $xy-$plane, with the nodal-loop lying in the mirror plane $k_z = 0$.

While a mirror symmetry is sufficient to stabilize a nodal-loop for a system with spin-orbit coupling, which is the focus of this thesis, this is not a unique mechanism. Other models have been explored in both theory and experiment, consisting of two-fold degenerate nodal-loops protected a screw rotation/glide symmetry [30–32], as well as a combination of time-reversal, inversion and $SU(2)$ symmetries [33–36]. In the latter case, the double nodal-loop can be decoupled into single nodal-loops corresponding to each spin degree of freedom, so it is often treated as a single nodal-loop of spinless fermions in the literature.

3.3 Topological aspects of a nodal-loop semimetal

Central to the characterization of topological phases of matter is the existence of a topological invariant associated with the transport properties of a system. In the example of a Chern insulator discussed in Sec. 2.2, there is a $\mathbb{Z}$ topological invariant corresponding to

18
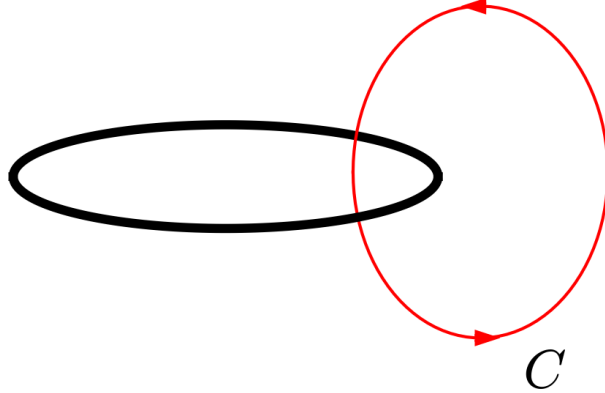
Figure 3.3: The path C (in red) taken for the $\mathbb{Z}_2$ topological invariant defined in Eq. (3.24), encircling the line-node (in black). The Berry phase around C is $\pm\pi$ for a topological line-node protected by time-reversal and inversion symmetries, and vanishes otherwise.

the Hall conductivity σ_{xy} [37]. Another example is the case of a Weyl semimetal, where the topological invariant corresponds to the existence of chiral Fermi-arc surface states [7].

A topological invariant for a nodal-loop was first discussed by Fang *et al.* in Ref. [31], who argued that a nodal-loop protected by time-reversal and inversion symmetries is characterized by a $\mathbb{Z}_2$ topological invariant. In particular, such a topological nodal-loop admits a Berry phase of π

$$\oint_C dk^\mu \, A_\mu(\boldsymbol{k}) = \pm\pi \tag{3.24}$$

around any closed path C that encircles the line-node, depicted in Fig. 3.3. The sign on the right-hand side of Eq. (3.24) is unphysical, it merely represents the circulation of the path C, defined by the choice of coordinate system. As explored in Sec. 3.4, a non-zero Berry phase encircling the nodal-loop corresponds to the existence of localized surface states.

An important consequence of the $\mathbb{Z}_2$ invariant defined in Eq. 3.24, is that a topological line-node is only possible when the line-node forms a closed loop in the first Brillouin zone. To see this, consider the contour C depicted in Fig. 3.3 surrounding an open line-node (i.e. it does not form a closed loop). The contour C can then be adiabatically deformed (without crossing a band touching point) to be removed from encircling the line-node, and subsequently shrunk down to a single point, which clearly has a vanishing Berry phase.

In the case where the nodal-loop is protected by a mirror symmetry, which is relevant to Eq. (3.11), the nodal-loop carries a $\mathbb{Z}$ topological invariant [38]. In this case, each eigenstate within the mirror-invariant plane $k_z = 0$ is also an eigenstate of the reflection operator $\mathcal{R}_z = \sigma_x$, with eigenvalues ± 1. The corresponding $\mathbb{Z}$ topological invariant is then defined as

$$\zeta \equiv N_A - N_B, \tag{3.25}$$

where N_A and N_B are the number of filled bands with reflection eigenvalue $+1$ at two different points A and B on the mirror-invariant plane with the same band filling [38]. The magnitude $|\zeta|$ of the invariant is then interpreted as the number of nodal-loops intersecting the line connecting A and B.

Another interesting aspect of topological order in 3D semimetals concerns the response in the presence of an external electromagnetic field $a_\mu(\boldsymbol{r}, \boldsymbol{t}) \equiv (a_0(\boldsymbol{r}, \boldsymbol{t}), \boldsymbol{a}(\boldsymbol{r}, \boldsymbol{t}))$, where a_0 and $\boldsymbol{a}$ denote the corresponding scalar and vector potentials. In the case of a Weyl semimetal consisting of a single pair of point-nodes, it is well established [39] that the topological response is characterized by a differential 1-form b_μ, which is determined solely by the geometry of the Weyl nodes, i.e. the separation of the nodes in energy and momentum. In this case, it was first shown in Ref. [40] that the electromagnetic field couples to b_μ to produce an effective action

$$S_{\text{Weyl}} = -\frac{e^2}{2\pi h} \int \mathrm{d}^4 x \, \epsilon^{\mu\nu\lambda\rho} b_\mu a_\nu \partial_\lambda a_\rho, \tag{3.26}$$

where the integral is taken over Minkowski spacetime, and $\epsilon^{\mu\nu\lambda\rho}$ is the completely anti-symmetric tensor. The electric 4-current is then given by the functional derivative of the action with respect to the electromagnetic potential

$$j^\mu = \frac{\delta S_{\text{Weyl}}}{\delta a_\mu}. \tag{3.27}$$

Combining this with Eq. 3.26, we see that the presence of Weyl nodes leads to an anomalous Hall conductivity proportional to the separation between Weyl nodes in momentum space

$$\sigma_{ij} = \frac{e^2}{2\pi h} \epsilon^{ij\ell} b_\ell, \tag{3.28}$$

whenever the two nodes coincide with the Fermi energy. While the anomalous Hall conductivity arises from the existence of topological Weyl nodes, the response differs from the case of a 2D quantum Hall insulator [37] as the value is not quantized. In fact, the quantized topological response in 2D topological insulators arises directly from the lack

of band touching points. The unquantized topological response is therefore a generic property of topological semimetals in 3D, and for this reason it is often referred to as a "quasi-topological response".

In the case of a nodal-loop semimetal, it was first suggested by Ramamurthy and Hughes that the electromagnetic response is characterized by a differential 2-form $B_{\mu\nu}$, described by the shape and orientation of the nodal-loop in the first Brillouin zone [10]. The electromagnetic field couples to $B_{\mu\nu}$ to produce an effective action

$$S_{\mathrm{NL}} = \frac{e}{16\pi^2} \int \mathrm{d}^4x \, \epsilon^{\mu\nu\lambda\rho} B_{\mu\nu} F_{\lambda\rho}, \tag{3.29}$$

where $F_{\lambda\rho} \equiv \partial_\rho a_\lambda - \partial_\lambda a_\rho$ is the electromagnetic field tensor. The 2-form in Eq. (3.29) couples to an external field in the same way as the magnetization/polarization tensor [41]. We can thus interpret the response as an intrinsic magnetization $\boldsymbol{M}$ and electric polarization $\boldsymbol{P}$, related to the geometric 2-form as

$$B_{0i} = \frac{4\pi^2}{e} M_a$$
$$B_{ij} = \frac{4\pi^2}{e} \epsilon^{ij\ell} P_\ell. \tag{3.30}$$

Another important consequence of the non-trivial topology in many phases of matter is the existence of gapless surface states that are qualitatively different than those of the bulk, i.e. the bulk-boundary correspondence [24, 42]. This correspondence holds in the case of nodal-loop semimetals, and is explored in detail in Sec. 3.4.

3.4 Drumhead surface states

The existence of gapless surface states in nodal-loop semimetals was first pointed out in Ref. [9], and has recently been measured using angle-resolved photoemission spectroscopy (ARPES) in the nodal-loop candidate SrAs$_3$ [43]. In particular, when the $\mathbb{Z}_2$ topological invariant in Eq. (3.24) is non-zero, a bound state is expected at any interface between two systems with a different topological invariant. The simplest example of this would be to consider the interface between a nodal-loop semimetal and the (topologically trivial) vacuum. In this section, we look at how the localized surface states can be computed from the model motivated in Sec. 2.3, using a method first introduced by Jackiw and Rebbi [44].
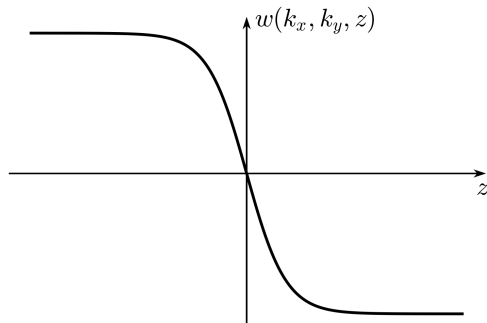
Figure 3.4: Example of the functional form of $w(k_x, k_y, z)$ in Eq. (3.32) at an interface. The precise functional form is not important, as long as it changes sign at the $z = 0$ interface.

The starting point is a low-energy theory of Eq. (3.11), obtained by expanding about $k_z = 0$ to linear order

$$H(\boldsymbol{k}) = w(k_x, k_y)\sigma_x + v_F k_z \sigma_y, \tag{3.31}$$

where $w(k_x, k_y) \equiv Q^2 - 2 + \cos k_x + \cos k_y$. The key to finding the bound state in this low-energy theory is to note that $w(k_x, k_y)$ changes sign when crossing the nodal-loop, where $w(k_x, k_y) = 0$, indicating a change in topology.

Assume now that the nodal-loop semimetal occupies the region $z < 0$ below the xy−plane, such that $z = 0$ corresponds to an interface between a topological semimetal and a trivial insulator (i.e. a vacuum). This change in topologies can be modeled by replacing $w(k_x, k_y)$ with a z-dependent function $w(k_x, k_y, z)$ that changes sign at $z = 0$. In this case, we have that $w(k_x, k_y, z) > 0$ for $z < 0$ and any k_x, k_y bounded by the nodal-loop. An example of such a function is depicted in Fig. 3.4.

As there is no longer a discrete translational symmetry in the z-direction, k_z is no longer a good quantum number. This can be accounted for by mapping the momentum k_z to a real-space momentum operator $k_z \to -i\frac{\partial}{\partial z}$. The Hamiltonian in Eq. (3.31) becomes

$$H(k_x, k_y, z) = w(k_x, k_y, z)\sigma_x - iv_F \sigma_y \frac{\partial}{\partial z}. \tag{3.32}$$

We would then like to find a zero energy mode $|\chi(k_x, k_y, z)\rangle$, given by the solution to

$$H(k_x, k_y, z) |\chi(k_x, k_y, z)\rangle = 0. \tag{3.33}$$

22

Making an ansatz for the form of the solution

$$|\chi(k_x, k_y, z)\rangle = ie^{F(k_x, k_y, z)} \sigma_y |a\rangle \tag{3.34}$$

for some function $F(k_x, k_y, z)$ and spinor $|a\rangle$, Eq. (3.33) simplifies to

$$\left(-w(k_x, k_y, z)\sigma_z + v_F \frac{\partial F}{\partial z} \right) |a\rangle = 0. \tag{3.35}$$

This equation has a single normalizable solution for $|a\rangle = |\sigma_z = 1\rangle$, the eigenvector of σ_z with eigenvalue 1, and

$$F(k_x, k_y, z) = \frac{1}{v_F} \int_0^z \mathrm{d}z' \, w(k_x, k_y, z'). \tag{3.36}$$

There is thus a single bound state localized at the interface, given by

$$|\chi(k_x, k_y, z)\rangle = \exp\left(\frac{1}{v_F} \int_0^z \mathrm{d}z' \, w(k_x, k_y, z') \right) |\sigma_z = -1\rangle. \tag{3.37}$$

This solution satisfies Eq. (3.33) for all k_x, k_y in the region bounded by the projection of the nodal-loop onto the surface Brillouin zone, implying the existence of a dispersionless bound state. Because the surface states are dispersionless over a finite area of the surface Brillouin zone, they are colloquially referred to as "drumhead" surface states. An important note that was made in Ref. [9], is that in real materials, the energy of a nodal-loop may not entirely coincide with the Fermi level, due to an inherent particle-hole asymmetry or only an approximate mirror plane arising from structural distortions. This can be accounted for in our model by the addition of a weakly dispersing term proportional to the identity $H(\boldsymbol{k}) \to H(\boldsymbol{k}) + h_0(\boldsymbol{k})\sigma_0$. Even in the presence of this additional term, the drumhead surface states remain intact, although they acquire a dispersion proportional to $h_0(\boldsymbol{k})$.

We can additionally look for evidence of drumhead surface states by numerically diagonalizing the Hamiltonian in Eq. (3.11) in the presence of open boundaries along the $z-$axis. Starting with the full nodal-loop lattice Hamiltonian

$$H = \sum_{\boldsymbol{k}} c_{\boldsymbol{k}}^\dagger \left[\left(Q^2 - 3 + \cos k_x + \cos k_y + \cos k_z \right) \sigma_x + v_F \sin k_z \sigma_y \right] c_{\boldsymbol{k}}, \tag{3.38}$$

where $c_{\boldsymbol{k}} = \begin{pmatrix} c_{\boldsymbol{k}\uparrow} & c_{\boldsymbol{k}\downarrow} \end{pmatrix}^T$, we can transform to real space along the z-axis by a Fourier transform

$$c_{\boldsymbol{k}} = \frac{1}{\sqrt{N_z}} \sum_j e^{ik_z z_j} c_{\boldsymbol{k}_\parallel, j}, \tag{3.39}$$

with $\boldsymbol{k}_\parallel = (k_x, k_y)$, N_z the number of sites in the z-direction and j the respective coordinate label. Plugging this transformation into Eq. (3.38), we get

$$
\begin{aligned}
H = &\sum_{\boldsymbol{k}_\parallel, j} c^\dagger_{\boldsymbol{k}_\parallel, j}(Q^2 - 3 + \cos k_x + \cos k_y)\sigma_x c_{\boldsymbol{k}_\parallel, j} \\
&+ \frac{1}{2} \sum_{\boldsymbol{k}_\parallel, j} \left[c^\dagger_{\boldsymbol{k}_\parallel, j} \left(\sigma_x + i v_F \sigma_y \right) c_{\boldsymbol{k}_\parallel, j+1} + c^\dagger_{\boldsymbol{k}_\parallel, j+1} \left(\sigma_x - i v_F \sigma_y \right) c_{\boldsymbol{k}_\parallel, j} \right].
\end{aligned}
\tag{3.40}
$$

We can then define a generalized spinor

$$
c_{\boldsymbol{k}_\parallel} \equiv \begin{pmatrix} c_{\boldsymbol{k}_\parallel, 1} & c_{\boldsymbol{k}_\parallel, 2} & \cdots & c_{\boldsymbol{k}_\parallel, N_z} \end{pmatrix}^T,
\tag{3.41}
$$

in which case the Hamiltonian becomes

$$
H = \sum_{\boldsymbol{k}_\parallel} c^\dagger_{\boldsymbol{k}_\parallel} \mathcal{M}_d(\boldsymbol{k}_\parallel) c_{\boldsymbol{k}_\parallel},
\tag{3.42}
$$

with

$$
\mathcal{M}_d(\boldsymbol{k}_\parallel) \equiv \begin{pmatrix}
Z(\boldsymbol{k}_\parallel) & Y & 0 & \cdots & 0 \\
Y^\dagger & Z(\boldsymbol{k}_\parallel) & Y & \ddots & \vdots \\
0 & Y^\dagger & Z(\boldsymbol{k}_\parallel) & \ddots & 0 \\
\vdots & \ddots & \ddots & \ddots & Y \\
0 & \cdots & 0 & Y^\dagger & Z(\boldsymbol{k}_\parallel)
\end{pmatrix}
\tag{3.43}
$$

a $2N_z \times 2N_z$ matrix with blocks defined by $Y \equiv (\sigma_x + i v_F \sigma_y)\tau_z/2$ and

$$
Z(\boldsymbol{k}_\parallel) \equiv (Q^2 - 3 + \cos k_x + \cos k_y)\sigma_x.
\tag{3.44}
$$

The band structure for a fixed system length N_z can then be obtained by numerically diagonalizing the matrix $\mathcal{M}_d(\boldsymbol{k}_\parallel)$. An example of this for $N_z = 31$ sites is shown in Fig. 3.5. As expected, the finite system bands show a dispersionless zero energy state bounded by the projection of the bulk nodal-loop.

A natural question to ask at this point is why the drumhead are dispersionless. Is this a necessary consequence from the symmetries protecting the nodal-loop? The answer is yes, the dispersionless surface states are a direct consequence of the mirror symmetry protecting the topological order of the nodal-loop. This is explored in detail in Sec. 3.5.
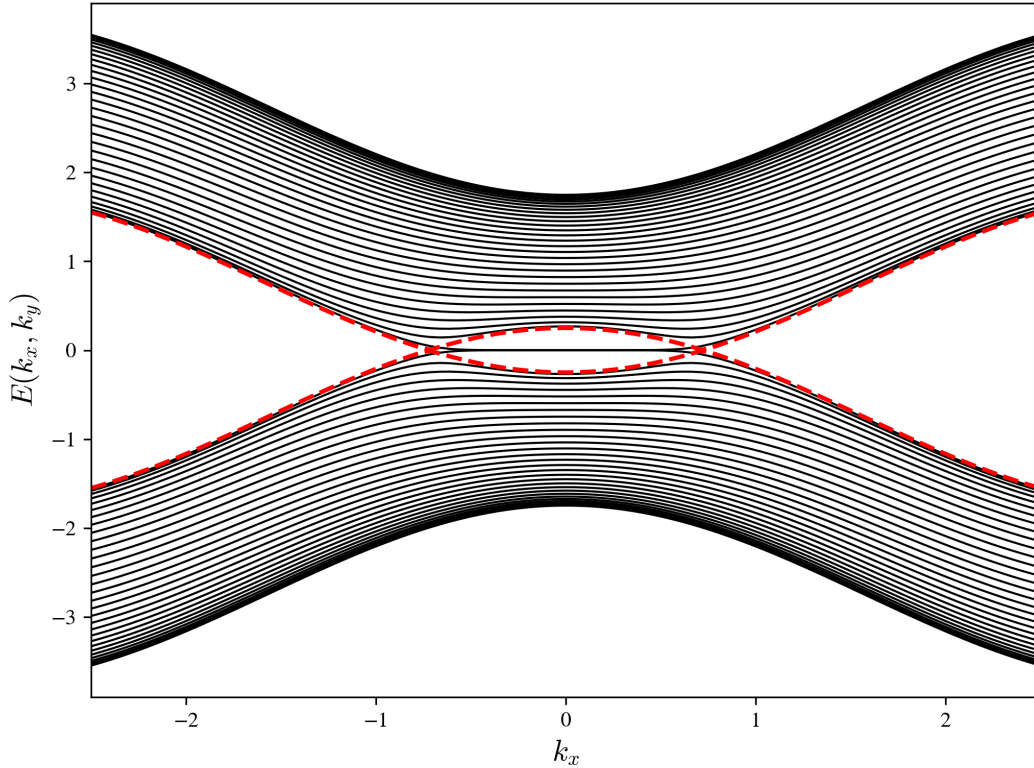
Figure 3.5: Energy spectrum for the nodal-loop semimetal in the presence of open boundaries along the $z-$axis, as defined in Eq. (3.40). The dispersionless drumhead surface are bounded by the projection of the nodal-loop onto the surface Brillouin zone. The bands are plotted for $N_z = 31$ sites, and with $Q = 1/2$, $v_F = 1$, $k_y = 0$. The bulk bands for $k_z = 0$ are superimposed in red.

3.5 Relation to the 2D Fermi liquid

Next, we look at an interesting connection between the 3D nodal-loop semimetal and a 2D Fermi liquid, as the result of explicitly breaking the symmetry protecting the topological nodal-loop. As discussed in Sec. 3.2, a topological line-node is protected by a mirror symmetry about the plane parallel to the nodal-loop. Consider a low-energy theory of Eq. (3.11) with the addition of a mirror symmetry breaking term $m\sigma_z$, described by the

(a)   (b)
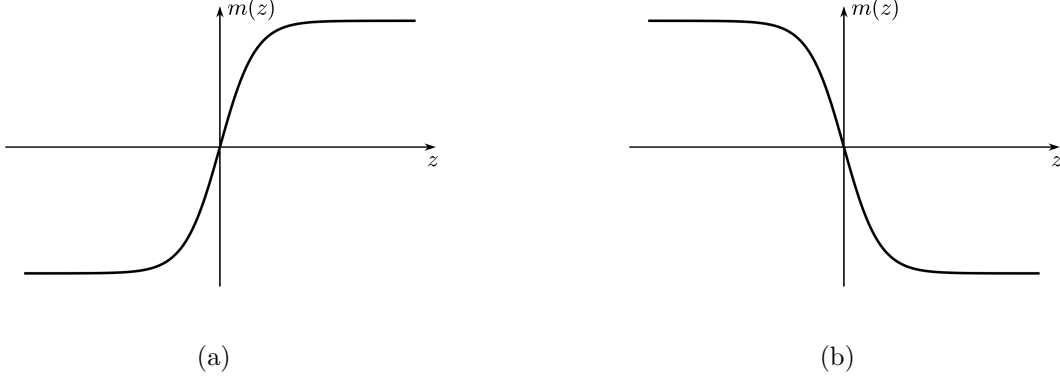
Figure 3.6: Example of the mirror symmetry breaking mass $m(z)$ in Eq. (3.46) at an interface for (a) mass changing from negative to positive and (b) mass changing from positive to negative. The precise functional form of $m(z)$ is not important, as long as it is integrable and changes sign at the interface.

Hamiltonian

$$H(\boldsymbol{k}) = (Q^2 - k_x^2 - k_y^2)\sigma_x + v_z k_z \sigma_y + m\sigma_z. \tag{3.45}$$

The eigenvalues of Eq. (3.45) are then given by

$$E_\pm(\boldsymbol{k}) = \pm\sqrt{(Q^2 - k_x^2 - k_y^2)^2 + v_z^2 k_z^2 + m^2},$$

and thus the spectrum is fully gapped for any $m \neq 0$. Since the gap closes and the nodal-loop is restored at precisely $m = 0$, there is a possibility that the $m > 0$ and $m < 0$ regimes correspond to topologically distinct phases. To see whether this is the case, we may look for localized eigenstates of Eq. (3.45) at an interface where the mirror symmetry breaking mass m changes sign. Imposing such an interface at the $z = 0$ boundary breaks translational symmetry along the z-axis, meaning that k_z is no longer a useful quantum number. This may be accounted for in Eq. (3.45) by making the substitutions $k_z \to -i\frac{\partial}{\partial z}$ and $m \to m(z)$, where $m(z)$ is an integrable function which changes sign at $z = 0$ (see Fig. 3.6), resulting in the Hamiltonian

$$H'(\boldsymbol{k}_\parallel, z) = (Q^2 - k_x^2 - k_y^2)\sigma_x - iv_z\sigma_y\frac{\partial}{\partial z} + m(z)\sigma_z, \tag{3.46}$$

where $\boldsymbol{k}_\parallel \equiv (k_x, k_y)$ are the crystal momentum components in the xy-plane.

26

We begin by looking for zero-energy solutions in the case where $k_x^2 + k_y^2 = Q^2$, where the Schrödinger equation reads

$$\left(-iv_z\sigma_y\frac{\partial}{\partial z} + m(z)\sigma_z\right)|\Psi(z)\rangle = 0. \tag{3.47}$$

First, consider the case of Fig. 3.6(a) where $m(z) > 0$ for $z > 0$. Making the ansatz

$$|\Psi(z)\rangle = e^{F(z)}\sigma_y|\chi\rangle \tag{3.48}$$

for some spinor $|\chi\rangle$, Eq. (3.47) simplifies to

$$\left(v_z\frac{\partial F}{\partial z} + m(z)\sigma_x\right)|\chi\rangle = 0.$$

This equation admits a single normalizable solution for $|\chi\rangle = |\sigma_x = 1\rangle$, the eigenstate of σ_x with eigenvalue 1, and

$$F(z) = -\int_0^z dz'\frac{m(z')}{v_z}.$$

It is then clear in the case where $m(z) > 0$ for $z > 0$, that $F(z) < 0$ for all z. Plugging this solution back into Eq. (3.48), we find that $\langle\Psi(z)|\Psi(z)\rangle \propto \exp\left(2F(z)\right)$ and

$$H'(\boldsymbol{k}_\parallel, z)|\Psi(z)\rangle = (k_x^2 + k_y^2 - Q^2)|\Psi(z)\rangle,$$

meaning that the resulting eigenstate is exponentially localized at the interface and disperses quadratically. This surface state therefore corresponds to a 2D Fermi liquid with a *particle-like* Fermi surface.

Next, consider the alternate case of Fig. 3.6(b) where $m(z) < 0$ for $z > 0$. A similar calculation yields a single normalizable solution

$$|\Psi(z)\rangle = \exp\left(\int_0^z dz'\frac{m(z')}{v_z}\right)\sigma_y|\sigma_x = -1\rangle,$$

which is similarly localized at the interface. In this case however, we have

$$H'(\boldsymbol{k}_\parallel, z)|\Psi(z)\rangle = (Q^2 - k_x^2 - k_y^2)|\Psi(z)\rangle,$$

therefore this surface state corresponds to a 2D Fermi liquid with a *hole-like* Fermi surface.

The existence of Fermi liquid surface states establishes that the nodal-loop (at $m = 0$) separates two topologically distinct regimes, and reaffirms the viewpoint of a topological

semimetal as a gapless phase which separates a topological and trivial insulator as described in Ref. [39]. To establish a direct connection between the 2D Fermi liquid and the 3D nodal-loop semimetal, we now consider the case where these surface states are stacked along the z direction.

Consider a multilayer system of 2D Fermi liquids, with alternating particle-like and hole-like Fermi surfaces separated by a distance $d/2$, each of which is connected by nearest-neighbour hopping. Here, t_1 denotes the hopping amplitude between surface states in the same unit cell, and t_2 the hopping between surface states in different unit cells. A schematic of this system is depicted in Fig. 3.7, and is described by the tight-binding Hamiltonian

$$H = \sum_{\boldsymbol{k}_\parallel, i, j} c_{\boldsymbol{k}_\parallel, i}^\dagger \left[\left(k_x^2 + k_y^2 - Q^2 \right) \sigma_z + t_1 \sigma_x \delta_{i,j} + \frac{t_2}{2} \sigma_+ \delta_{i,j-1} + \frac{t_2}{2} \sigma_- \delta_{i,j+1} \right] c_{\boldsymbol{k}_\parallel, j}, \qquad (3.49)$$

where i, j label the various surfaces, and the Pauli operators now act on the orbital degree of freedom, resulting from the 2-site periodicity of the multilayer. A Fourier transform in the $z-$direction results in the momentum space Hamiltonian

$$H(\boldsymbol{k}_\parallel, k_z) = (t_1 + t_2 \cos(k_z d)) \, \sigma_x - t_2 \sin(k_z d) \sigma_y + \left(k_x^2 + k_y^2 - Q^2 \right) \sigma_z. \qquad (3.50)$$

To restore the nodal-loop, we must impose that the system exhibit a mirror symmetry about the xy-plane, given by

$$\sigma_x H(\boldsymbol{k}_\parallel, k_z) \sigma_x = H(\boldsymbol{k}_\parallel, -k_z),$$

which holds only when $t_1/t_2 = \pm 1$. Assuming that $t_1 = -t_2 \equiv v_z$, $d = 1$, and expanding Eq. (3.50), the low-energy Hamiltonian becomes

$$H(\boldsymbol{k}_\parallel, k_z) = - \left(k_x^2 + k_y^2 - Q^2 \right) \sigma_z + v_z k_z \sigma_y,$$

which is the same low-energy Hamiltonian for the nodal-loop in Eq. (3.11), up to a unitary transformation. A nodal-loop can therefore be viewed as a stack of weakly coupled 2D Fermi liquids, protected by a mirror symmetry about the xy-plane.

3.6 Experimental evidence for nodal-loop semimetals

Since the first theoretical proposal of a nodal-loop semimetal [9], there has been a large number of proposed material realizations. As discussed in Sec. 3.2, nodal-loops in 3D are
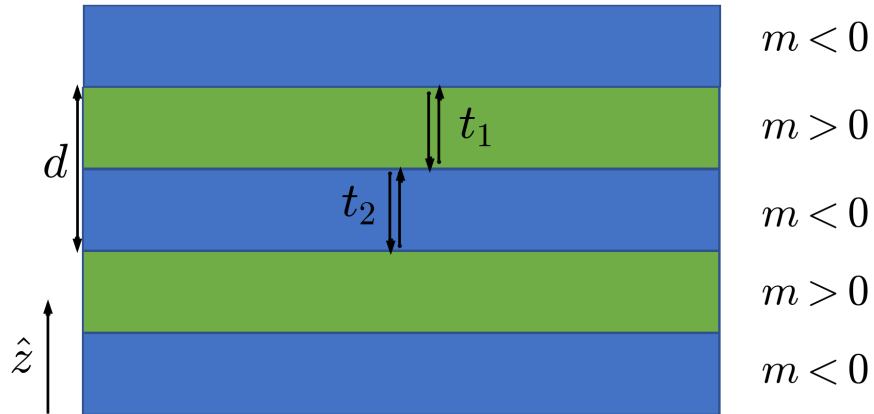
Figure 3.7: Schematic of the multilayer system described by Eq. (3.49).

stabilized by crystalline symmetries in addition to translational symmetry, such as a mirror symmetry or a combination of inversion and time-reversal symmetries.

In the case where the nodal-loop is protected by both inversion and time-reversal symmetries, the topology is characterized by the $\mathbb{Z}_2$ invariant defined in Eq. (3.24). Several materials have been theoretically identified in this class of nodal-loop semimetals, with experimental realizations in ZrSiS [45] and ZrSnTe [46].

Several mirror symmetric nodal-loop semimetal candidates have also been explored recently, including evidence of nodal-loops in ARPES measurements of CaAgAs [47, 48] and HfSiS [49]. The material TlTaSe$_2$ has also been proposed theoretically as mirror symmetric nodal-loop candidate [50].

In the case of materials with strong spin-orbit coupling, which is relevant to the models considered in this thesis, the first experimental evidence for topological nodal-loop states was by ARPES measurements of the superconducting compound PbTaSe$_2$ [51]. A unit cell

in this material consists of one Pb, one Ta and two Se atoms, each of which reside on a quasi-2D hexagonal layer (see Fig. 3.8(**a**)). The out of plane geometry can be understood as a set of alternating Pb and $TaSe_2$ layers along the $z-$axis. This material lacks full inversion symmetry, however the existence of a mirror plane stabilizes a nodal-loop (see Fig. 3.8).

The result of these ARPES measurements is shown in Fig. 3.9, along with corresponding density-functional theory (DFT) calculations of the band structure along the (001)-projected surface. The bands labelled by SS2 in Fig. 3.9 correspond to a set of three surface modes connecting the projection of the bulk nodal-loop, i.e. the drumhead surface states. The band labelled SS1 in Fig. 3.9 corresponds to a surface Dirac mode, which has been suggested to be evidence for chiral p-wave pairing in this compound [52]. This finding motivates the treatment of electronic interactions in Chapter 4, in the framework of a generalized BCS theory.
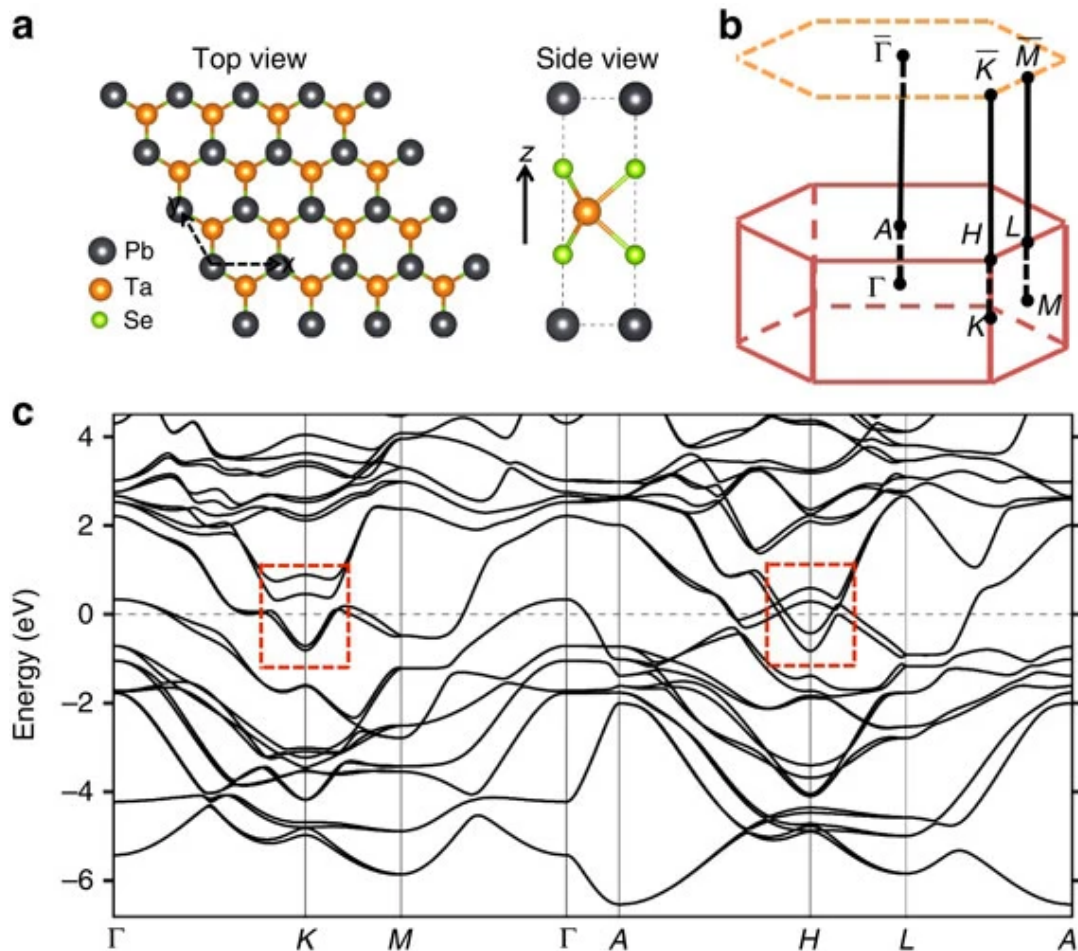
Figure 3.8: Lattice structure and bulk energy bands of PbTaSe$_2$. (**a**) The lattice consists of quasi-2D hexagonal layers, stacked along the z-axis. (**b**) The Brillouin zone and high symmetry points of the bulk (in red) and (001)-projected surface (in orange). (**c**) Bulk band structure, calculating using a generalized gradient approximation. The mirror symmetry stabilizes nodal-loops near the Fermi level around the K and H high symmetry points, outlined in red. Figure reprinted from Ref. [51] under the terms of a Creative Commons CC BY license.
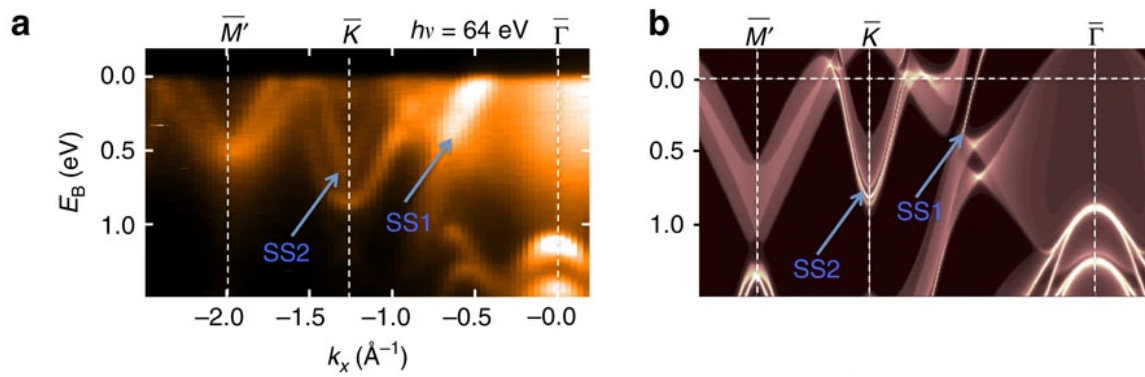
Figure 3.9: ARPES (**a**) and DFT calculations (**b**) of the (001)-projected surface bands of PbTaSe$_2$. (**a**) ARPES spectra taken along the $\overline{M} - \overline{K} - \overline{\Gamma}$ path. (**b**) DFT calculations for the projected bulk bands and surface bands. Figure reprinted from Ref. [51] under the terms of a Creative Commons CC BY license.

Chapter 4

Electronic interactions in nodal-loop semimetals

This chapter explores the effect of interactions in a nodal-loop semimetal, in the context of a mean-field BCS theory. Section 4.1 motivates the framework of a generalized BCS theory by applying a mean-field approximation to a general spin-dependent attractive interaction. Section 4.2 subsequently investigates the effect of both s-wave and chiral p-wave pairing to the nodal-loop model. Section 4.3 generalizes the chiral p-wave state to include vortices, where we find a single Dirac mode protected by a mirror symmetry.

4.1   Interactions and BCS theory

Superconductivity – the vanishing of electrical resistance below a critical temperature – was first discovered in mercury by Kamerlingh Onnes in 1911. After this, it took nearly five decades to develop a microscopic theory of this phenomenon [53]. This highly celebrated theory by Bardeen, Cooper and Schrieffer is commonly referred to as BCS theory, and describes superconductivity as arising from the condensation of electron pairs, known as *Cooper pairs*.

Superconducting mercury is now referred to as a conventional superconductor: it is well described by the original formulation of BCS theory, where Cooper pairs correspond to pairs of time-reversed electrons, brought on by an effective attractive interaction due to distortions in the surrounding crystal lattice. Since then, this theory has been generalized to so-called unconventional superconductors, where Cooper pairs are stabilized by a momentum dependent pairing mechanism.

This generalized BCS theory can be understood as the mean-field theory of a general attractive interaction, where electron pairs scatter with zero net momentum [54]:

$$H_{\text{int}} = \frac{1}{2} \sum_{\boldsymbol{k}\boldsymbol{k}'} \sum_{\sigma_1\sigma_2\sigma_3\sigma_4} U_{\sigma_1\sigma_2\sigma_3\sigma_4}(\boldsymbol{k}, \boldsymbol{k}') c^\dagger_{\boldsymbol{k}\sigma_1} c^\dagger_{-\boldsymbol{k}\sigma_2} c_{-\boldsymbol{k}'\sigma_3} c_{\boldsymbol{k}'\sigma_4}, \tag{4.1}$$

where $c^\dagger_{\boldsymbol{k}\sigma}$ ($c_{\boldsymbol{k}\sigma}$) are electron creation (annihilation) corresponding to momentum $\boldsymbol{k}$ and spin σ. By defining a "pair fluctuation operator"

$$f^\dagger_{\sigma_1\sigma_2}(\boldsymbol{k}) \equiv c^\dagger_{\boldsymbol{k}\sigma_1} c^\dagger_{-\boldsymbol{k}\sigma_2} - \left\langle c^\dagger_{\boldsymbol{k}\sigma_1} c^\dagger_{-\boldsymbol{k}\sigma_2} \right\rangle,$$

where $\langle ... \rangle$ denotes the expectation value in the ground state, we can rewrite Eq. (4.1) as

$$H_{\text{int}} = \frac{1}{2} \sum_{\boldsymbol{k}\boldsymbol{k}'} \sum_{\sigma_1\sigma_2\sigma_3\sigma_4} U_{\sigma_1\sigma_2\sigma_3\sigma_4}(\boldsymbol{k}, \boldsymbol{k}') \left(f^\dagger_{\sigma_1\sigma_2}(\boldsymbol{k}) + \left\langle c^\dagger_{\boldsymbol{k}\sigma_1} c^\dagger_{-\boldsymbol{k}\sigma_2} \right\rangle \right) \left(f_{\sigma_4\sigma_3}(\boldsymbol{k}') + \left\langle c_{-\boldsymbol{k}'\sigma_3} c_{\boldsymbol{k}'\sigma_4} \right\rangle \right).$$

A mean-field approximation is then obtained by ignoring all terms that are second order in the fluctuation operators, i.e. the terms proportional to $f^\dagger_{\sigma_1\sigma_2}(\boldsymbol{k}) f_{\sigma_4\sigma_3}(\boldsymbol{k}')$. The mean-field Hamiltonian is then given by

$$H_\Delta = \frac{1}{2} \sum_{\boldsymbol{k}\boldsymbol{k}'} \sum_{\sigma_1\sigma_2\sigma_3\sigma_4} U_{\sigma_1\sigma_2\sigma_3\sigma_4}(\boldsymbol{k}, \boldsymbol{k}') \left(c^\dagger_{\boldsymbol{k}\sigma_1} c^\dagger_{-\boldsymbol{k}\sigma_2} \left\langle c_{-\boldsymbol{k}'\sigma_3} c_{\boldsymbol{k}'\sigma_4} \right\rangle + \left\langle c^\dagger_{\boldsymbol{k}\sigma_1} c^\dagger_{-\boldsymbol{k}\sigma_2} \right\rangle c_{-\boldsymbol{k}'\sigma_3} c_{\boldsymbol{k}'\sigma_4} \tag{4.2}$$

$$- \left\langle c^\dagger_{\boldsymbol{k}\sigma_1} c^\dagger_{-\boldsymbol{k}\sigma_2} \right\rangle \left\langle c_{-\boldsymbol{k}'\sigma_3} c_{\boldsymbol{k}'\sigma_4} \right\rangle \right).$$

We may then define the superconducting gap matrix

$$\Delta_{\sigma\sigma'}(\boldsymbol{k}) \equiv \frac{1}{2} \sum_{\boldsymbol{k}'} \sum_{\sigma_3\sigma_4} U_{\sigma\sigma'\sigma_3\sigma_4}(\boldsymbol{k}, \boldsymbol{k}') \left\langle c^\dagger_{\boldsymbol{k}\sigma_3} c^\dagger_{-\boldsymbol{k}\sigma_4} \right\rangle, \tag{4.3}$$

which may be interpreted as the wavefunction of a Cooper pair at a fixed momentum $\boldsymbol{k}$. This leads to the familiar form of the BCS Hamiltonian

$$H_\Delta = \sum_{\boldsymbol{k}} \sum_{\sigma\sigma'} \left(\Delta_{\sigma\sigma'}(\boldsymbol{k}) c^\dagger_{\boldsymbol{k}\sigma} c^\dagger_{-\boldsymbol{k}\sigma'} + \Delta^*_{\sigma\sigma'}(\boldsymbol{k}) c_{-\boldsymbol{k}\sigma'} c_{\boldsymbol{k}\sigma} \right) + \mathcal{E}_0, \tag{4.4}$$

where

$$\mathcal{E}_0 \equiv -\frac{1}{2} \sum_{\boldsymbol{k}\boldsymbol{k}'} \sum_{\sigma_1\sigma_2\sigma_3\sigma_4} U_{\sigma_1\sigma_2\sigma_3\sigma_4}(\boldsymbol{k}, \boldsymbol{k}') \left\langle c^\dagger_{\boldsymbol{k}\sigma_1} c^\dagger_{-\boldsymbol{k}\sigma_2} \right\rangle \left\langle c_{-\boldsymbol{k}'\sigma_3} c_{\boldsymbol{k}'\sigma_4} \right\rangle$$

34

is a constant energy term that can generally be omitted.

The gap matrix in Eq. (4.3) can be parametrized further, by noting that angular momentum is a good quantum number for the orbital part of the Cooper pair wavefunction. In particular, given that a Cooper pair carries integer spin, the orbital part of the gap matrix may be decomposed into a superposition of spherical harmonics $Y_\ell^m(\hat{\boldsymbol{k}})$ where $\hat{\boldsymbol{k}}$ is a unit vector pointing in the direction of the momentum $\boldsymbol{k}$, and ℓ is the angular momentum quantum number. Note that the spherical harmonics have the property $Y_\ell^m(-\hat{\boldsymbol{k}}) = (-1)^\ell Y_\ell^m(\hat{\boldsymbol{k}})$, therefore fermion statistics guarantee that the gap matrix $\Delta_{\sigma\sigma'}(\boldsymbol{k})$ must be antisymmetric whenever ℓ is even, and symmetric whenever ℓ is odd. These cases are referred to as *singlet* and *triplet* pairing respectively. In the case of singlet pairing , we can thus parametrize the gap matrix in terms of the only antisymmetric Pauli matrix

$$\Delta(\boldsymbol{k}) = d_0(\boldsymbol{k})i\sigma_y,$$

where $d_0(\boldsymbol{k})$ is a function referred to as the singlet order parameter. In the case of triplet pairing , we can parametrize the gap matrix in terms of the three symmetric Pauli matrices

$$\Delta(\boldsymbol{k}) = (\boldsymbol{d}(\boldsymbol{k}) \cdot \boldsymbol{\sigma})\, i\sigma_y,$$

where $\boldsymbol{d}(\boldsymbol{k})$ is a 3-component vector referred to as the triplet order parameter. It is standard to refer to the angular momentum quantum number in terms of the spdf-notation. For example, s-wave pairing corresponds to a singlet order parameter with $d_0(\boldsymbol{k}) \propto Y_0^0(\hat{k}) =$ constant, and p-wave pairing corresponds to a triplet order parameter with each component related to a combination of $\ell = 1$ spherical harmonics.

4.2   Electron pairing in nodal-loop semimetals

We may now examine the effects of electron interactions in a nodal-loop semimetal within the framework of BCS theory developed in Sec. 4.1. Consider the nodal-loop model Eq. (3.11) with the addition of a BCS pairing term

$$
\begin{aligned}
H = \sum_{\boldsymbol{k}} c_{\boldsymbol{k}}^\dagger & \left[(Q^2 - 3 + \cos k_x + \cos k_y + \cos k_z)\sigma_x + v_F \sin k_z \sigma_y \right] c_{\boldsymbol{k}} \\
& + \sum_{\boldsymbol{k}} \sum_{\sigma\sigma'} \left(\Delta_{\sigma\sigma'}(\boldsymbol{k}) c_{\boldsymbol{k}\sigma}^\dagger c_{-\boldsymbol{k}\sigma'}^\dagger + \Delta_{\sigma\sigma'}^*(\boldsymbol{k}) c_{-\boldsymbol{k}\sigma'} c_{\boldsymbol{k}\sigma} \right).
\end{aligned}
\tag{4.5}
$$

The typical procedure to diagonalize a quadratic many-body Hamiltonian is to simply diagonalize the coefficient matrix in a single-particle subspace. While the BCS Hamiltonian

35

in Eq. (4.4) is quadratic in fermion operators, it contains anomalous terms proportional to two creation/annihilation operators. To diagonalize such a Hamiltonian, one must effectively double the degrees of freedom by introducing a Nambu spinor

$$\Psi_{\boldsymbol{k}} \equiv \begin{pmatrix} c_{\boldsymbol{k}\uparrow} \\ c_{\boldsymbol{k}\downarrow} \\ c_{-\boldsymbol{k}\uparrow}^{\dagger} \\ c_{-\boldsymbol{k}\downarrow}^{\dagger} \end{pmatrix}, \tag{4.6}$$

where the last two components can be interpreted equivalently as creating an electron with momentum $-\boldsymbol{k}$, or annihilating a hole with momentum $\boldsymbol{k}$. This interpretation follows from the fact that the Nambu spinor itself satisfies the fermionic anticommutator relations $\{[\Psi_{\boldsymbol{k}}]_a, [\Psi_{\boldsymbol{k}'}]_b\} = 0$ and $\{[\Psi_{\boldsymbol{k}}]_a, [\Psi_{\boldsymbol{k}'}^{\dagger}]_b\} = \delta_{\boldsymbol{k}\boldsymbol{k}'}\delta_{ab}$. The Nambu representation in Eq. (4.6) can then be used to bring the Hamiltonian to the so-called Bogoliubov-de Gennes form as

$$H = \frac{1}{2} \sum_{\boldsymbol{k}} \Psi_{\boldsymbol{k}}^{\dagger} H_{\text{BdG}}(\boldsymbol{k}) \Psi_{\boldsymbol{k}}, \tag{4.7}$$

where the factor of $1/2$ accounts for doubling the degrees of freedom. The Hamiltonian may then be diagonalized by applying an appropriate linear transformation to the Nambu operators $\Psi_{\boldsymbol{k}}$, known as a Bogoliubov transformation, that must preserve the fermionic anticommutator rules. In this case, the Bogoliubov-de Gennes form of Eq. (4.5) is given by

$$H_{\text{BdG}}(\boldsymbol{k}) = \begin{pmatrix} H_0(\boldsymbol{k}) & \Delta(\boldsymbol{k}) \\ \Delta^{\dagger}(\boldsymbol{k}) & -H_0^T(-\boldsymbol{k}) \end{pmatrix}, \tag{4.8}$$

with $H_0(\boldsymbol{k}) = (Q^2 - 3 + \cos k_x + \cos k_y + \cos k_z)\sigma_x + v_F \sin k_z \sigma_y$ the nodal-loop Hamiltonian, and $\Delta(\boldsymbol{k})$ the 2×2 gap matrix with components $\Delta_{\sigma\sigma'}(\boldsymbol{k})$. This can be written in a more compact notation by defining a triplet of Pauli operators $\boldsymbol{\tau}$ which act on the particle/hole degree of freedom in the Nambu space. In particular, by defining

$$\tau_x \equiv \begin{pmatrix} 0 & \mathbb{I} \\ \mathbb{I} & 0 \end{pmatrix} \qquad \tau_y \equiv \begin{pmatrix} 0 & -i\mathbb{I} \\ i\mathbb{I} & 0 \end{pmatrix} \qquad \tau_z \equiv \begin{pmatrix} \mathbb{I} & 0 \\ 0 & -\mathbb{I} \end{pmatrix},$$

with $\mathbb{I}$ the 2×2 identity matrix, the Bogoliubov-de Gennes Hamiltonian can be written as

$$H_{\text{BdG}}(\boldsymbol{k}) = (Q^2 - 3 + \cos k_x + \cos k_y + \cos k_z)\sigma_x\tau_z + v_F \sin k_z \sigma_y\tau_z + \frac{1}{2}\Delta(\boldsymbol{k})\tau_+ + \frac{1}{2}\Delta^{\dagger}(\boldsymbol{k})\tau_-, \tag{4.9}$$

with $\tau_{\pm} \equiv \tau_x \pm i\tau_y$. To find the eigenvalues of Eq. (4.9), we must solve the eigenvalue equation

$$\det(H_{\text{BdG}}(\boldsymbol{k}) - E(\boldsymbol{k})\sigma_0\tau_0) = 0, \tag{4.10}$$

36

for $E(\boldsymbol{k})$ to obtain a set of four particle/hole energy bands. In general, this would involve finding the roots of a 4th order polynomial. In this work, we consider cases in which the Hamiltonian has a particle-hole symmetry, in which case this calculation can be simplified.

At this point it is convenient to define a particle/hole conjugation operator

$$\mathcal{P} \equiv \mathcal{K}\tau_x, \tag{4.11}$$

where $\mathcal{K}$ is the complex conjugation operator. A Bogoliubov-de Gennes Hamiltonian is then said to have a particle-hole symmetry when

$$\mathcal{P}H_{\text{BdG}}(\boldsymbol{k})\mathcal{P}^{-1} = -H_{\text{BdG}}(\boldsymbol{k}). \tag{4.12}$$

Now, suppose that $|E(\boldsymbol{k})\rangle$ is an eigenstate of $H_{\text{BdG}}(\boldsymbol{k})$ with energy $E(\boldsymbol{k})$. If the particle-hole symmetry defined in Eq. (4.12) is satisfied, then it follows that

$$H_{\text{BdG}}(\boldsymbol{k})\mathcal{P}\,|E(\boldsymbol{k})\rangle = -\mathcal{P}H_{\text{BdG}}(\boldsymbol{k})\,|E(\boldsymbol{k})\rangle = -E(\boldsymbol{k})\mathcal{P}\,|E(\boldsymbol{k})\rangle\,, \tag{4.13}$$

therefore $\mathcal{P}\,|E(\boldsymbol{k})\rangle$ is also an eigenstate of $H_{\text{BdG}}(\boldsymbol{k})$ with energy $-E(\boldsymbol{k})$. The particle-hole symmetry enforces that eigenstates of the Bogoliubov-de Gennes Hamiltonian come in pairs with opposite energy. In cases with particle-hole symmetry, it turns out to be much simpler to solve for the eigenvalues of the square of $H_{\text{BdG}}(\boldsymbol{k})$, given by

$$
\begin{aligned}
H_{\text{BdG}}^2(\boldsymbol{k}) = {}& H_0^2(\boldsymbol{k}) + \frac{1}{2}\{\Delta(\boldsymbol{k}), \Delta^\dagger(\boldsymbol{k})\} + \frac{1}{2}\big[\Delta(\boldsymbol{k}), \Delta^\dagger(\boldsymbol{k})\big]\tau_z \\
& + \frac{1}{2}[H_0(\boldsymbol{k}), \Delta(\boldsymbol{k})]\tau_+ + \frac{1}{2}\big[\Delta^\dagger(\boldsymbol{k}), H_0(\boldsymbol{k})\big]\tau_-,
\end{aligned}
\tag{4.14}
$$

as each eigenvalue $E^2(\boldsymbol{k})$ is then ensured to be at least doubly degenerate.

The goal now is to find a pairing mechanism for the nodal-loop which fully gaps the band structure, but preserves the non-trivial topological nature, to result in a topological superconductor. As explored in Sec. 3.2, a topological nodal-loop is symmetry protected by a reflection about the plane parallel to the nodal-loop. Any pairing mechanism that breaks this symmetry therefore gaps the nodal-loop into a trivial superconductor. The rest of this section is focused on discerning the topological properties of a nodal-loop superconductor in two cases: s-wave and chiral p-wave pairing, each of which preserve the mirror symmetry protecting the topological nodal-loop.

4.2.1 Nodal-loop with s-wave pairing

We first consider band structure in the case of s-wave pairing, often referred to as *conventional superconductivity*. In this case, the gap matrix is antisymmetric, and the singlet order parameter is proportional to the $\ell = 0$ spherical harmonic (a constant). Setting $\Delta(\boldsymbol{k}) = id_0\sigma_y$ with d_0 a complex number, the corresponding Bogoliubov-de Gennes Hamiltonian is then given by

$$H_{\text{BdG}}(\boldsymbol{k}) = h_x(\boldsymbol{k})\sigma_x\tau_z + v_F \sin k_z \sigma_y\tau_z + \frac{i}{2}d_0\sigma_y\tau_+ - \frac{i}{2}d_0^*\sigma_y\tau_-, \tag{4.15}$$

where $h_x(\boldsymbol{k}) \equiv Q^2 - 3 + \cos k_x + \cos k_y + \cos k_z$ is defined for convenience. This Hamiltonian has a particle-hole symmetry as defined in Eq. (4.12), as well as a mirror symmetry about the xy-plane. In this case, we have $\{\Delta(\boldsymbol{k}), \Delta^\dagger(\boldsymbol{k})\} = 2|d_0|^2$, $\left[\Delta(\boldsymbol{k}), \Delta^\dagger(\boldsymbol{k})\right] = 0$, and $[H_0(\boldsymbol{k}), \Delta(\boldsymbol{k})] = -d_0 h_x(\boldsymbol{k})\sigma_z$. It follows from Eq. (4.14) that

$$H_{\text{BdG}}^2(\boldsymbol{k}) = h_x^2(\boldsymbol{k}) + v_F^2 \sin^2 k_z + |d_0|^2 - \frac{1}{2}h_x(\boldsymbol{k})\left[(d_0 + d_0^*)\tau_x + i(d_0 - d_0^*)\tau_y\right]\sigma_z. \tag{4.16}$$

This form of $H_{\text{BdG}}^2(\boldsymbol{k})$ can be readily block-diagonalized to the form $H_{\text{BdG}}^2(\boldsymbol{k}) = A_+(\boldsymbol{k}) \oplus A_-(\boldsymbol{k})$ with

$$A_\pm(\boldsymbol{k}) = h_x^2(\boldsymbol{k}) + v_F^2 \sin^2 k_z + |d_0|^2 \pm 2h_x(\boldsymbol{k})|d_0|\sigma_z.$$

Each block can then be diagonalized individually to obtain the dispersion

$$E_\pm^2(\boldsymbol{k}) = (h_x(\boldsymbol{k}) \pm |d_0|)^2 + v_F^2 \sin^2 k_z, \tag{4.17}$$

which can then be mapped to the respective particle and hole bands, that come in pairs due to the particle-hole symmetry. The band structure is shown in Fig. 4.1, where we see that the nodal-loop is preserved but shifted to finite energy above the Fermi level. It is clear from Eq. (4.17) that this energy shift in the band touching points is equal to the s-wave order parameter $|d_0|$.

From the dispersion in Eq. (4.17), we can also see that s-wave pairing leads to the formation of an additional nodal-loop at zero energy, when the order parameter d_0 is small in magnitude. This occurs at $k_z = 0$, and at k_x, k_y given by the solution of the equation

$$Q^2 + |d_0| - 2 + \cos k_x + \cos k_y = 0.$$

This nodal-loop is expected to be non-topological however, as one can adiabatically increase $|d_0|$ until the nodes are gapped while preserving the mirror symmetry. To understand this more explicitly, we can look for surface states in the presence of an open boundary along the
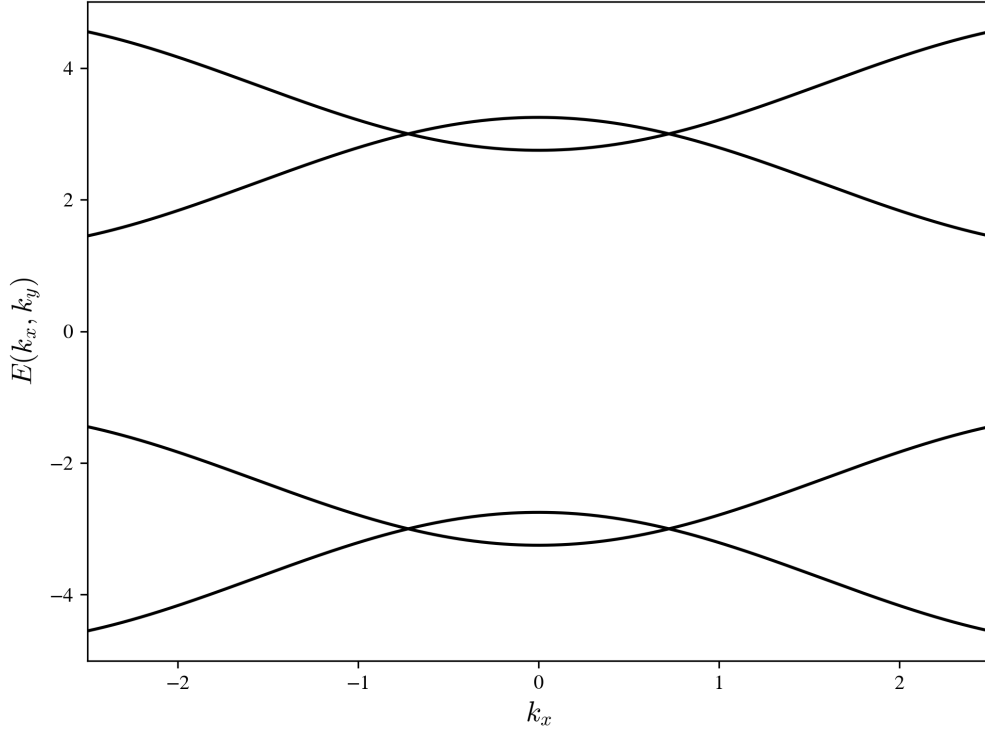
Figure 4.1: Energy spectrum for the nodal-loop semimetal with s-wave pairing defined in Eq. (4.15). The nodal-loop remains intact, but is shifted to finite energy $|d_0|$. The bands are plotted for $d_0 = 3$, $Q = 1/2$, $v_F = 1$, $k_y = k_z = 0$.

z-axis, similar to the calculation of the drumhead surface states in Sec. 3.4. Since k_z is no longer be a good quantum number with open boundary conditions, we must first transform z-component of the Bogoliubov-de Gennes Hamiltonian to real space, by defining a Nambu spinor

$$\Psi_{\boldsymbol{k}} = \frac{1}{\sqrt{N_z}} \sum_j e^{ik_z z_j} \Psi_{\boldsymbol{k}_\parallel, j}, \tag{4.18}$$

where $\boldsymbol{k}_\parallel = (k_x, k_y)$ and j labels the N_z coordinates along the z-axis. Plugging this

transformation into Eq. (4.7) and combining with Eq. (4.15), the Hamiltonian is given by

$$H = \frac{1}{2} \sum_{\boldsymbol{k}_\parallel,j} \Psi^\dagger_{\boldsymbol{k}_\parallel,j} \left((Q^2 - 3 + \cos k_x + \cos k_y)\sigma_x \tau_z + \frac{i}{2} d_0 \sigma_y \tau_+ - \frac{i}{2} d_0^* \sigma_y \tau_- \right) \Psi_{\boldsymbol{k}_\parallel,j}$$
$$+ \frac{1}{4} \sum_{\boldsymbol{k}_\parallel,j} \left[\Psi^\dagger_{\boldsymbol{k}_\parallel,j} \left(\sigma_x + i v_F \sigma_y \right) \tau_z \Psi_{\boldsymbol{k}_\parallel,j+1} + \Psi^\dagger_{\boldsymbol{k}_\parallel,j+1} \left(\sigma_x - i v_F \sigma_y \right) \tau_z \Psi_{\boldsymbol{k}_\parallel,j} \right]. \tag{4.19}$$

Assuming that there are N_z sites along the z-axis with open boundaries, we can define a generalized Nambu spinor

$$\Psi_{\boldsymbol{k}_\parallel} \equiv \begin{pmatrix} \Psi_{\boldsymbol{k}_\parallel,1} & \Psi_{\boldsymbol{k}_\parallel,2} & \dots & \Psi_{\boldsymbol{k}_\parallel,N_z} \end{pmatrix}^T, \tag{4.20}$$

in which case the Hamiltonian becomes

$$H = \frac{1}{2} \sum_{\boldsymbol{k}_\parallel} \Psi^\dagger_{\boldsymbol{k}_\parallel} \mathcal{M}_s(\boldsymbol{k}_\parallel) \Psi_{\boldsymbol{k}_\parallel}, \tag{4.21}$$

with

$$\mathcal{M}_s(\boldsymbol{k}_\parallel) \equiv \begin{pmatrix} X(\boldsymbol{k}_\parallel) & Y & 0 & \dots & 0 \\ Y^\dagger & X(\boldsymbol{k}_\parallel) & Y & \ddots & \vdots \\ 0 & Y^\dagger & X(\boldsymbol{k}_\parallel) & \ddots & 0 \\ \vdots & \ddots & \ddots & \ddots & Y \\ 0 & \dots & 0 & Y^\dagger & X(\boldsymbol{k}_\parallel) \end{pmatrix} \tag{4.22}$$

a $4N_z \times 4N_z$ Hermitian matrix with blocks defined by $Y \equiv (\sigma_x + i v_F \sigma_y)\tau_z/2$ and

$$X(\boldsymbol{k}_\parallel) \equiv (Q^2 - 3 + \cos k_x + \cos k_y)\sigma_x \tau_z + \frac{i}{2} d_0 \sigma_y \tau_+ - \frac{i}{2} d_0^* \sigma_y \tau_-. \tag{4.23}$$

The band structure for a fixed system length N_z can then be obtained by diagonalizing the matrix $\mathcal{M}_s(\boldsymbol{k}_\parallel)$. An example of this for $N_z = 31$ sites is shown in Fig. 4.2. As expected, there is no zero energy surface state corresponding to the nodal-loop formed by weak s-wave pairing. The dispersionless drumhead surface states become gapped with energy $\pm|d_0|$, existing everywhere within the projection of the nodal-loop onto the surface Brillouin zone. The surface state involved with s-wave pairing therefore corresponds to a 2D gapped trivial superconductor. An analytic expression for these gapped surface states can be derived by considering a low-energy theory of Eq. (4.15) at an interface, in the same way that was outlined in Sec. 3.4. The functional form of these states is almost exactly the same as the non-interacting case, with the result being multiplied by a τ_z eigenstate, corresponding to the respective particle and hole degrees of freedom.
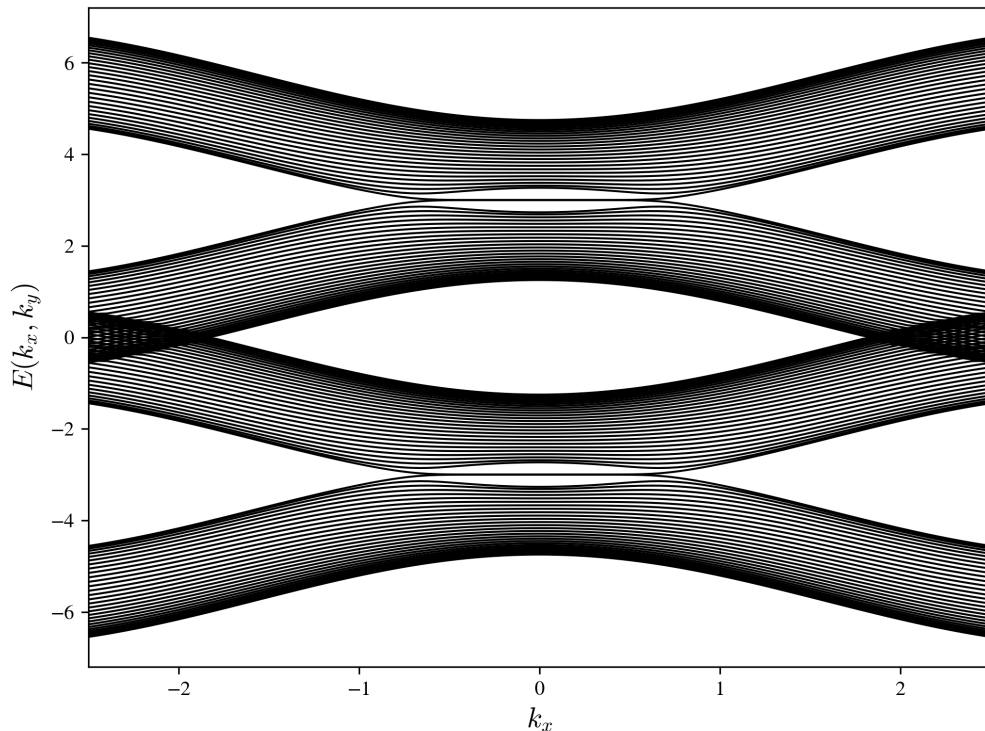
Figure 4.2: Energy spectrum for the nodal-loop semimetal with s-wave pairing defined in Eq. (4.19). The dispersionless drumhead surface states are gapped with energy $|d_0|$. The bands are plotted for $N_z = 31$ sites with open boundaries along the $z-$axis, and with $d_0 = 3$, $Q = 1/2$, $v_F = 1$, $k_y = 0$.

4.2.2 Nodal-loop with chiral p-wave pairing

Next, we consider the case of a chiral p-wave pairing [55], where the triplet order parameter takes the form $\boldsymbol{d}(\boldsymbol{k}) = -i\Delta_0(\sin k_x + i \sin k_y)\hat{\boldsymbol{y}}$, with Δ_0 a constant that may be determined self-consistently by the mean-field equations. This gap matrix has been well studied in the context of a 2D Fermi liquid, leading to a topological superconductor with Majorana quasiparticles in the presence of vortices [56, 57]. Coupled to a nodal-loop, the

corresponding Bogoliubov-de Gennes Hamiltonian is given by

$$
\begin{aligned}
H_{\mathrm{BdG}}(\boldsymbol{k}) = {} & (Q^2 - 3 + \cos k_x + \cos k_y + \cos k_z)\sigma_x\tau_z + v_F \sin k_z \sigma_y\tau_z \\
& + \frac{1}{2}\Delta_0(\sin k_x + i \sin k_y)\tau_+ + \frac{1}{2}\Delta_0^*(\sin k_x - i \sin k_y)\tau_-.
\end{aligned} \tag{4.24}
$$

Similar to the case of s-wave pairing, this Hamiltonian has a particle-hole symmetry as defined in Eq. (4.12), as well as a mirror symmetry about the xy-plane. In this case, we have $\{\Delta(\boldsymbol{k}), \Delta^\dagger(\boldsymbol{k})\} = 2|\Delta_0|^2(\sin^2 k_x + \sin^2 k_y)$, $[\Delta(\boldsymbol{k}), \Delta^\dagger(\boldsymbol{k})] = 0$, and $[H_0(\boldsymbol{k}), \Delta(\boldsymbol{k})] = 0$. Again using $h_x(\boldsymbol{k}) = Q^2 - 3 + \cos k_x + \cos k_y + \cos k_z$, it follows from Eq. (4.14) that

$$
H_{\mathrm{BdG}}^2(\boldsymbol{k}) = h_x^2(\boldsymbol{k}) + v_F^2 \sin^2 k_z + |\Delta_0|^2(\sin^2 k_x + \sin^2 k_y), \tag{4.25}
$$

which is conveniently already in diagonal form. This Hamiltonian therefore has two doubly degenerate bands, that disperse as

$$
E_\pm(\boldsymbol{k}) = \pm\sqrt{h_x^2(\boldsymbol{k}) + v_F^2 \sin^2 k_z + |\Delta_0|^2(\sin^2 k_x + \sin^2 k_y)}. \tag{4.26}
$$

The band structure is shown in Fig. 4.3 for $k_y = k_z = 0$, where we see that the nodal-loop is fully gapped, leading to the formation of an avoided crossing. It is clear from Eq. (4.26) that for weak pairing, this gap is proportional to the magnitude of the p-wave order parameter $|\boldsymbol{d}(\boldsymbol{k})| = |\Delta_0|\sqrt{\sin^2 k'_x + \sin^2 k'_y}$ evaluated with k'_x and k'_y along the nodal-loop of the non-interacting model.

As the chiral p-wave pairing fully gaps the nodal loop while preserving the mirror symmetry about the xy-plane, it is expected that the resulting superconductor is topologically non-trivial and exhibit gapless surface states. We can look for evidence of these surface states in the presence of an open boundary along the z-axis, similar to the calculation in Sec. 4.2.1. The Fourier transform of the Bogoliubov-de Gennes Hamiltonian Eq. (4.24) along the z-axis is given by

$$
\begin{aligned}
H = {} & \frac{1}{2}\sum_{\boldsymbol{k}_\parallel, j} \Psi_{\boldsymbol{k}_\parallel, j}^\dagger \left((Q^2 - 3 + \cos k_x + \cos k_y)\sigma_x\tau_z + \frac{1}{2}\Delta_0(\sin k_x + i \sin k_y)\tau_+ \right. \\
& \left. \hspace{6cm} + \frac{1}{2}\Delta_0^*(\sin k_x - i \sin k_y)\tau_- \right) \Psi_{\boldsymbol{k}_\parallel, j} \\
& + \frac{1}{4}\sum_{\boldsymbol{k}_\parallel, j} \left[\Psi_{\boldsymbol{k}_\parallel, j}^\dagger \left(\sigma_x + iv_F\sigma_y\right) \tau_z \Psi_{\boldsymbol{k}_\parallel, j+1} + \Psi_{\boldsymbol{k}_\parallel, j+1}^\dagger \left(\sigma_x - iv_F\sigma_y\right) \tau_z \Psi_{\boldsymbol{k}_\parallel, j} \right].
\end{aligned} \tag{4.27}
$$
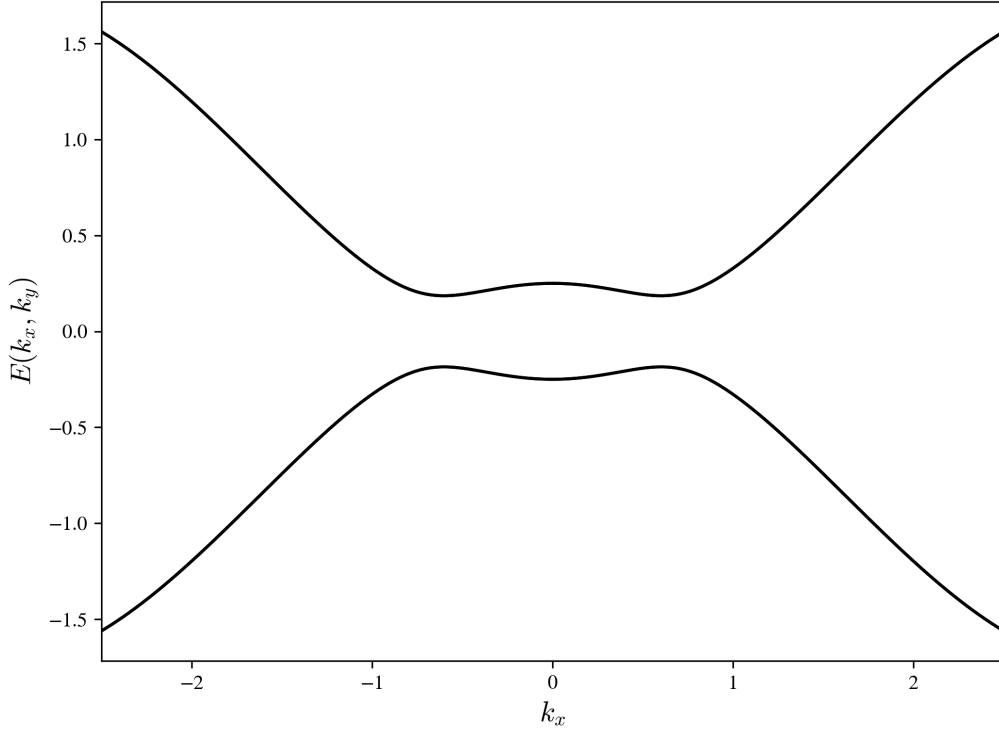
Figure 4.3: Energy spectrum for the nodal-loop semimetal with chiral p-wave pairing defined in Eq. (4.24). The nodal-loop is fully gapped while preserving the mirror symmetry about the xy-plane. The bands are plotted for $\Delta_0 = 0.3$, $Q = 1/2$, $v_F = 1$, $k_y = k_z = 0$.

Defining a generalized Nambu spinor in the same way as Eq. (4.20), the Hamiltonian becomes

$$H = \frac{1}{2} \sum_{\boldsymbol{k}_\parallel} \Psi^\dagger_{\boldsymbol{k}_\parallel} \mathcal{M}_p(\boldsymbol{k}_\parallel) \Psi_{\boldsymbol{k}_\parallel}, \tag{4.28}$$

43

with

$$\mathcal{M}_p(\boldsymbol{k}_\parallel) \equiv \begin{pmatrix} X'(\boldsymbol{k}_\parallel) & Y & 0 & \cdots & 0 \\ Y^\dagger & X'(\boldsymbol{k}_\parallel) & Y & \ddots & \vdots \\ 0 & Y^\dagger & X'(\boldsymbol{k}_\parallel) & \ddots & 0 \\ \vdots & \ddots & \ddots & \ddots & Y \\ 0 & \cdots & 0 & Y^\dagger & X'(\boldsymbol{k}_\parallel) \end{pmatrix} \tag{4.29}$$

a $4N_z \times 4N_z$ Hermitian matrix with blocks defined by $Y \equiv (\sigma_x + iv_F\sigma_y)\tau_z/2$ and

$$X'(\boldsymbol{k}_\parallel) \equiv (Q^2 - 3 + \cos k_x + \cos k_y)\sigma_x\tau_z + \frac{1}{2}\Delta_0(\sin k_x + i\sin k_y)\tau_+ + \frac{1}{2}\Delta_0^*(\sin k_x - i\sin k_y)\tau_-. \tag{4.30}$$

The band structure for a fixed system length N_z can then be obtained by diagonalizing the matrix $\mathcal{M}_p(\boldsymbol{k}_\parallel)$. An example of this for $N_z = 31$ sites is shown in Fig. 4.4. We see that in fact, a zero energy state exists in the presence of an open boundary in the $z-$direction, implying that the p-wave superconductor retains the topological order of the nodal-loop, despite being fully gapped in the bulk, i.e. a topological superconductor. These surface states however, have acquired a linear dispersion from the p-wave pairing, with surface states of opposite chirality appearing as a consequence of the particle-hole symmetry of Eq. (4.24). To see this explicitly, we can generalize the calculation of the bound state from Sec. 3.4 to a low-energy theory of the Bogoliubov-de Gennes Hamiltonian in Eq. (4.24)

$$H_{\mathrm{BdG}}(\boldsymbol{k}) \approx w(k_x, k_y)\sigma_x\tau_z + v_F k_z\sigma_y\tau_z + \frac{1}{2}\Delta_0(\sin k_x + i\sin k_y)\tau_+ + \frac{1}{2}\Delta_0^*(\sin k_x - i\sin k_y)\tau_-, \tag{4.31}$$

obtained by expanding about $k_z = 0$ to linear order and defining $w(k_x, k_y) = Q^2 - 2 + \cos k_x + \cos k_y$. Making the canonical transformation

$$\sigma_\pm \to \sigma_\pm\tau_z \qquad \tau_\pm \to \sigma_z\tau_\pm, \tag{4.32}$$

the Hamiltonian becomes

$$H_{\mathrm{BdG}}(\boldsymbol{k}) = w(k_x, k_y)\sigma_x + v_F k_z\sigma_y + \left(\frac{1}{2}\Delta_0(\sin k_x + i\sin k_y)\tau_+ + \frac{1}{2}\Delta_0^*(\sin k_x - i\sin k_y)\tau_-\right)\sigma_z, \tag{4.33}$$

which is readily block diagonalized into the form $H_{\mathrm{BdG}}(\boldsymbol{k}) = H_+(\boldsymbol{k}) \oplus H_-(\boldsymbol{k})$ where

$$H_\pm(\boldsymbol{k}) = w(k_x, k_y)\sigma_x + v_F k_z\sigma_y \pm |\Delta_0|\sqrt{\sin^2 k_x + \sin^2 k_y}\,\sigma_z. \tag{4.34}$$

44
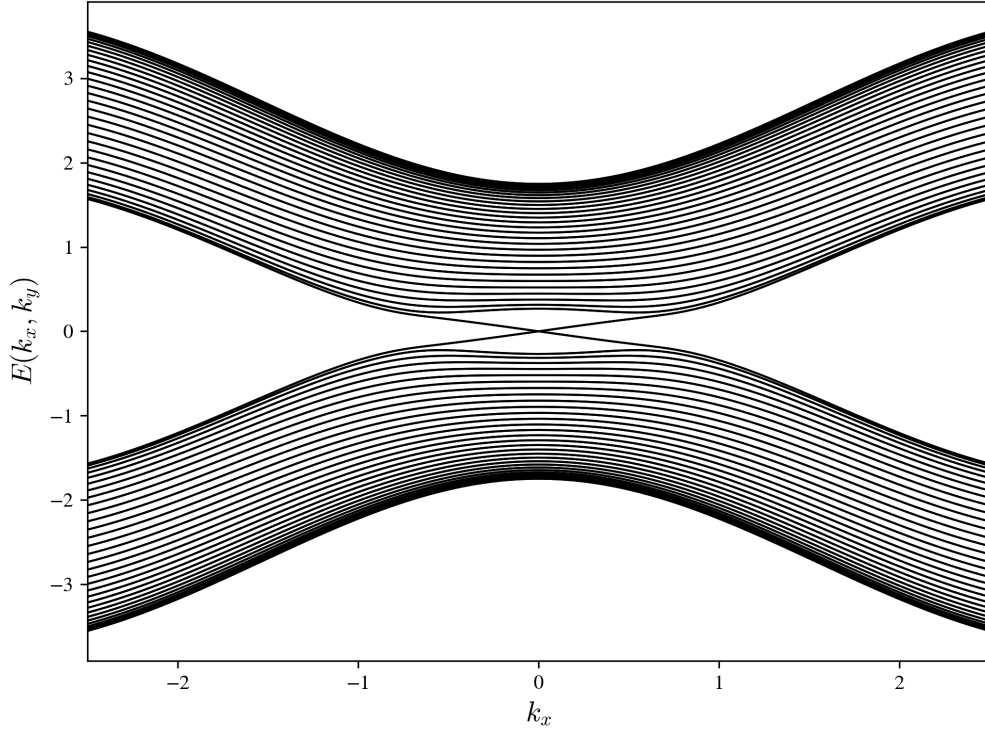
Figure 4.4: Finite system spectrum for the nodal-loop semimetal with chiral p-wave pairing defined in Eq. (4.27). The drumhead surface states acquire a linear dispersion with velocity proportional to the gap function $|\Delta_0|$. The bands are plotted for $N_z = 31$ sites with open boundaries along the $z-$axis, and with $\Delta_0 = 0.3$, $Q = 1/2$, $v_F = 1$, $k_y = 0$.

At this point, we can repeat the same bound state calculation as for the drumhead surface states in Sec. 3.4 individually for each block of $H_{\mathrm{BdG}}(\boldsymbol{k})$. By mapping $w(k_x, k_y) \rightarrow w(k_x, k_y, z)$, a function that changes sign at $z = 0$ (see Fig. (3.4)) and $k_z \rightarrow -i\frac{\partial}{\partial z}$, the Hamiltonian of each block becomes

$$H_{\pm}(\boldsymbol{k}_{\parallel}, z) = w(k_x, k_y, z)\sigma_x - v_F\sigma_y\frac{\partial}{\partial z} \pm |\Delta_0|\sqrt{\sin^2 k_x + \sin^2 k_y}\sigma_z. \qquad (4.35)$$

By taking the same bound state solution for the drumhead states in Eq. (3.37), it follows

45

that

$$H_\pm(\boldsymbol{k}_\parallel, z) \left|\chi(k_x, k_y, z)\right\rangle = \pm|\Delta_0|\sqrt{\sin^2 k_x + \sin^2 k_y}\left|\chi(k_x, k_y, z)\right\rangle. \qquad (4.36)$$

The surface of a nodal-loop with chiral p-wave pairing thus admits two normalizable bound states, which disperse linearly as $\pm|\Delta_0\boldsymbol{k}_\parallel|$ for small $|\boldsymbol{k}_\parallel|$, and are related by particle-hole symmetry. Note that once again, this bound state solution only remains valid for $\boldsymbol{k}_\parallel$ in the region bounded by the nodal-loop in the surface Brillouin zone.

4.3 Vortices

In the presence of a magnetic field, a type-II superconductor can form vortices of super-current to lower the free energy, circulating around a quantum of magnetic flux [58]. The superconducting order parameter Δ_0 vanishes at the center of a vortex, known as the vortex core (see Fig. 4.5), and acquires a phase $2\pi\ell$ around a path surrounding it, where ℓ is an integer referred to as the *vorticity*. When a gapped superconductor is topological, in the sense that it exhibits gapless surface states, it can additionally support gapless states localized at a vortex core, where the superconducting gap vanishes [55]. This is particular well studied in the context of a 2D Fermi liquid with chiral p-wave pairing, which is known to host a single zero energy Majorana mode in each vortex core of odd vorticity [56, 57, 59, 60]. This section generalizes these calculations to show the existence of Majorana modes localized at the vortex core of a nodal-loop semimetal with chiral p-wave pairing.

Consider a low-energy Hamiltonian for a nodal-loop in the presence of chiral p-wave pairing, obtained by expanding Eq. (4.24) for small $\boldsymbol{k}$, given by

$$H_{\mathrm{BdG}}(\boldsymbol{k}) \approx (Q^2 - k_x^2 - k_y^2)\sigma_x\tau_z + v_F k_z \sigma_y \tau_z + \frac{1}{2}\Delta_0(k_x + ik_y)\tau_+ + \frac{1}{2}\Delta_0^*(k_x - ik_y)\tau_-. \quad (4.37)$$

First, we may look for zero energy states in a vortex core for the case when $k_z = 0$. Recall from Sec. 3.5, that gapping the nodal-loop with an inversion breaking perturbation leads to 2D Fermi liquid surface states. The effective Hamiltonian for the top and bottom Fermi liquid surface states corresponds to the first term in Eq. (4.37), with the σ_x operator now interpreted as acting on the top/bottom surface degree of freedom. By making this correspondence, we can view the system at $k_z = 0$ as a set of two decoupled Fermi liquids with chiral p-wave pairing, each of which is expected have a zero energy Majorana mode for each vortex core of odd vorticity $\ell = 2n - 1$.

46
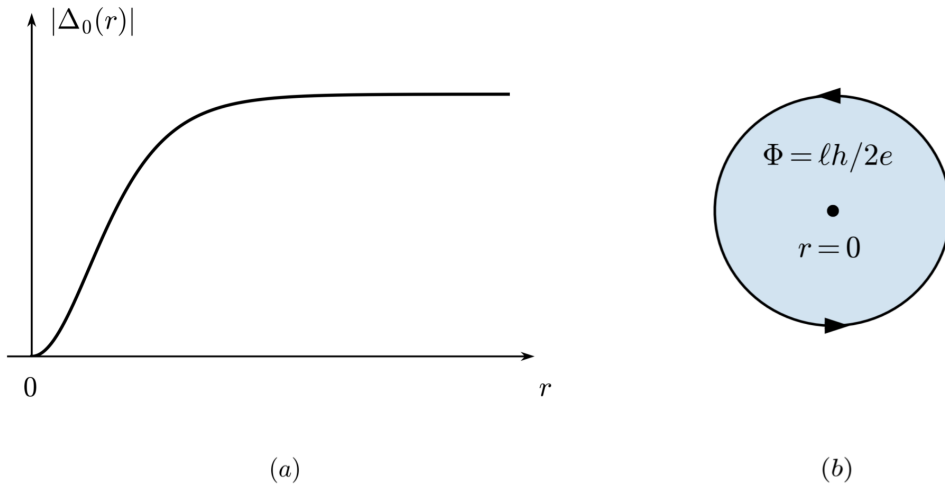
Figure 4.5: Configuration of a symmetric vortex centered at radial coordinate $r = 0$. (a) The superconducting gap $|\Delta_0|$ goes to zero at the vortex core. (b) A vortex of vorticity ℓ encircles a quantum of magnetic flux $\Phi = \ell h/2e$. This corresponds to the gap function acquiring a phase of $2\pi\ell$ around any path encircling the vortex core.

To compute the vortex core states at $k_z = 0$ explicitly, consider a slab of material with 2D chiral p-wave Fermi liquid surface states on the top and bottom surfaces, with a symmetric vortex line of vorticity ℓ penetrating the slab in the $z-$direction. This configuration is depicted in Fig. 4.6, and can be modeled by a position-dependant gap function

$$\Delta_0 \to \Delta_0(r, \theta) \equiv i|\Delta_0(r)|e^{i\ell\theta}, \tag{4.38}$$

where $r = \sqrt{x^2 + y^2}$ and $\tan\theta = y/x$ are the polar coordinates relative to the vortex core. The vortex breaks translational symmetry, which can be accounted for by mapping $k_x \to -i\frac{\partial}{\partial x}$ and $k_y \to -i\frac{\partial}{\partial y}$.

There is one important subtlety when making this transformation, as the chiral p-wave order parameter now depends on both the coordinate and momentum, which do not commute with each other. The standard way to circumvent this complication is to replace any product of coordinate and momentum with the anticommutator of the two [61], i.e.

$$\Delta_0(r, \theta)\partial_\mu \to \frac{1}{2}\{\Delta_0(r, \theta), \partial_\mu\}$$
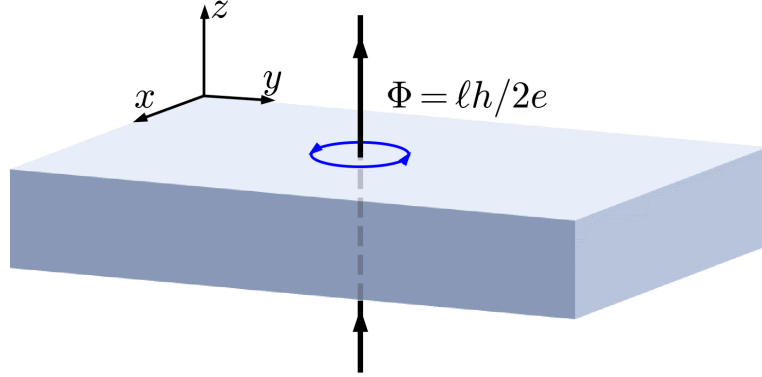
Figure 4.6: Configuration of a symmetric vortex line of vorticity ℓ penetrating a 3D slab with 2D chiral p-wave surface states, as described by Eq. (4.39). The vortex line carries a magnetic flux quantum $\Phi = \ell h/2e$. This configuration is equivalent to the chiral p-wave nodal-loop semimetal when $k_z = 0$.

for any differential operator ∂_μ, which puts the two non-commuting operators on equal footing. With all of this in mind, Eq. (4.37) becomes

$$H_{\mathrm{BdG}} = \sigma_x \tau_z (Q^2 + \boldsymbol{\nabla}^2) + \frac{1}{2}\left(\tau_+ \Delta_0 \frac{\partial}{\partial \alpha} - \tau_- \Delta_0^* \frac{\partial}{\partial \alpha^*}\right) + \frac{1}{4}\left(\tau_+ \frac{\partial \Delta_0}{\partial \alpha} - \tau_- \frac{\partial \Delta_0^*}{\partial \alpha^*}\right), \quad (4.39)$$

where the complex coordinate $\alpha = x + iy$ has been introduced for convenience. We may now look for a zero energy state in the vortex core as a solution to the equation $H_{\mathrm{BdG}} |\gamma(r,\theta)\rangle = 0$. Since the top and bottom Fermi liquid surface states are decoupled, we can assume that $|\gamma(r,\theta)\rangle$ is an eigenstate of σ_x with eigenvalue $\sigma_x' = \pm 1$, i.e. $|\gamma(r,\theta)\rangle = |\sigma_x = \sigma_x'\rangle |\eta(r,\theta)\rangle$. Combining Eq. (4.38) and Eq. (4.39), the eigenvalue equation for the zero energy state

becomes

$$\sigma'_x \tau_z (Q^2 + \boldsymbol{\nabla}^2) \left| \eta(r, \theta) \right\rangle + \frac{1}{2} \sqrt{|\Delta_0(r)|} e^{i\ell\theta/2} \frac{\partial}{\partial \alpha} \left(e^{i\ell\theta/2} \sqrt{|\Delta_0(r)|} \tau_+ \left| \eta(r, \theta) \right\rangle \right) \quad (4.40)$$
$$- \frac{1}{2} \sqrt{|\Delta_0(r)|} e^{-i\ell\theta/2} \frac{\partial}{\partial \alpha^*} \left(e^{-i\ell\theta/2} \sqrt{|\Delta_0(r)|} \tau_- \left| \eta(r, \theta) \right\rangle \right) = 0.$$

This equation has been studied in detail for a fixed value of σ'_x in Ref. [57], where it was shown that there are no even vorticity solutions (i.e. when $\ell = 2n$), as an appropriate change of basis brings it to a form that is adiabatically connected to a system without vortices. Assuming that the vorticity is odd $\ell = 2n - 1$, we can expand the solution in the basis of τ_z as

$$\left| \eta(r, \theta) \right\rangle = u(r, \theta) e^{in\theta} \left| \tau_z = 1 \right\rangle + v(r, \theta) e^{-in\theta} \left| \tau_z = -1 \right\rangle \quad (4.41)$$

for some position dependent functions u and v. The condition for this state to be a Majorana quasiparticle is that it be invariant under the particle-hole conjugation operator $\mathcal{P} \left| \eta(r, \theta) \right\rangle = \left| \eta(r, \theta) \right\rangle$, with $\mathcal{P} = \mathcal{K} \tau_x$, meaning that $u^*(r, \theta) = v(r, \theta)$. We henceforth look for bound state solutions of this form. Transforming to polar coordinates using the relations

$$\frac{\partial}{\partial x} \pm i \frac{\partial}{\partial y} = e^{\pm i\theta} \left(\frac{\partial}{\partial r} \pm \frac{i}{r} \frac{\partial}{\partial \theta} \right) \quad (4.42)$$

and

$$\boldsymbol{\nabla}^2 = \frac{\partial^2}{\partial r^2} + \frac{1}{r} \frac{\partial}{\partial r} + \frac{1}{r^2} \frac{\partial^2}{\partial \theta^2}, \quad (4.43)$$

Eq. (4.40) simplifies to a single differential equation

$$\sigma'_x \frac{\partial^2 u}{\partial r^2} + \frac{\sigma'_x}{r^2} \frac{\partial^2 u}{\partial \theta^2} + \frac{\sigma'_x}{r} \frac{\partial u}{\partial r}$$
$$+ |\Delta_0(r)| \frac{\partial u^*}{\partial r} + \frac{i}{r} |\Delta_0(r)| \frac{\partial u^*}{\partial \theta} + \frac{|\Delta_0(r)|}{2r} u^* + \frac{1}{2} \frac{\partial |\Delta_0(r)|}{\partial r} u^* + \sigma'_x \left(Q^2 - \frac{n^2}{r^2} \right) u = 0. \quad (4.44)$$

Assuming a θ independent localized solution of the form

$$u(r) = \xi(r) \exp \left(-\frac{1}{2} \int_0^r \mathrm{d}r' \, |\Delta_0(r')| \right), \quad (4.45)$$

Eq. (4.44) simplifies further as

$$
\sigma_x' \frac{\mathrm{d}^2 \xi}{\mathrm{d}r^2} + \frac{\sigma_x'}{r} \frac{\mathrm{d}\xi}{\mathrm{d}r} + \sigma_x' \left(Q^2 - \frac{n^2}{r^2} \right) \xi
$$
$$
+ \frac{|\Delta_0(r)|^2}{4} (\sigma_x' \xi - 2\xi^*) + \left(\frac{|\Delta_0(r)|}{2r} + \frac{1}{2} \frac{\mathrm{d}|\Delta_0(r)|}{\mathrm{d}r} + |\Delta_0(r)| \frac{\mathrm{d}}{\mathrm{d}r} \right) (\xi^* - \sigma_x' \xi) = 0.
$$

(4.46)

For the top/bottom Fermi liquid surface states, the eigenvalue of σ_x is given by $\sigma_x' = \pm 1$. For a given surface, Eq. (4.46) can be simplified by letting $\xi^*(r) = \sigma_x' \xi(r)$, to the equation

$$
-\frac{\mathrm{d}^2 \xi}{\mathrm{d}r^2} - \frac{1}{r} \frac{\mathrm{d}\xi}{\mathrm{d}r} + \left(\frac{1}{4} |\Delta_0(r)| - Q^2 + \frac{n^2}{r^2} \right) \xi(r) = 0.
$$

(4.47)

This is equivalent to the Schrödinger equation for a particle in a 2D radial potential $V(r) = \frac{1}{4} |\Delta_0(r)|^2 - Q^2$ with angular momentum quantum number n. This equation admits a normalizable solution for any $Q > 0$, although the exact functional form depends on the gap function $\Delta_0(r)$. Within the simplest approximation of a uniform gap function $\Delta_0(r) = \Delta_0$ at all r except inside an infinitesimally small vortex core, Eq. (4.47) simplifies to Bessel's equation, with normalizable solutions given by

$$
\xi_n(r) = I_n \left(r \sqrt{Q^2 - \frac{|\Delta_0|^2}{4}} \right),
$$

(4.48)

a modified Bessel function of the first kind in the case of weak pairing $|\Delta_0|^2 < 4Q^2$, and

$$
\xi_n(r) = J_n \left(r \sqrt{\frac{|\Delta_0|^2}{4} - Q^2} \right),
$$

(4.49)

a Bessel function of the first kind in the case of strong pairing $|\Delta_0|^2 > 4Q^2$. There is therefore two localized Majorana zero modes at $k_z = 0$ for each vortex line with odd vorticity $\ell = 2n - 1$, given by

$$
|\gamma_\pm(r, \theta)\rangle = \xi_n(r) \exp \left(-\frac{1}{2} \int_0^r \mathrm{d}r' \, |\Delta_0(r')| \right) |\sigma_x = \pm 1\rangle \left(e^{in\theta} |\tau_z = 1\rangle \pm e^{-in\theta} |\tau_z = -1\rangle \right).
$$

(4.50)

An example of the radial probability amplitude for a an $\ell = 1$ vorticity Majorana mode is shown in Fig. 4.7 within the approximation of an infinitesimally small vortex core, in the case of both weak and strong pairing.

With the general solution for the Majorana zero modes given by Eq. (4.50), we may generalize this calculation to the case when $k_z \neq 0$, corresponding to a low-energy theory of the full nodal-loop model. This model can be obtained from the 3D slab configuration depicted in Fig. 4.6, by stacking the slabs along the $z-$direction and linking the surface states by tunneling. Recall from Sec. 3.5, that such a multilayer system restores the translational and mirror symmetries that protect the nodal-loop in the case of alternating tunneling amplitudes of equal magnitude $\pm v_F$. The resulting low-energy theory is equivalent to Eq. (4.37), so it is expected that the full nodal-loop model stabilizes vortex core states.

Considering again a vortex line configuration with odd vorticity along the $z-$axis, the low energy model is simply obtained by modifying Eq. (4.39) as $H_{\text{BdG}} \rightarrow H_{\text{BdG}} + v_F k_z \sigma_y \tau_z$. Applying this Hamiltonian to the solution for the Majorana zero modes in Eq (4.50), they now transform as

$$H_{\text{BdG}} \left|\gamma_{\pm}(r,\theta)\right\rangle = \mp i v_F k_z \left|\gamma_{\mp}(r,\theta)\right\rangle, \tag{4.51}$$

therefore, the low-energy Hamiltonian in the Majorana basis is simply

$$H_{\text{BdG}} = v_F k_z \sigma_y. \tag{4.52}$$

This corresponds to two linearly dispersing states for each value of k_z along the vortex line, with energy $E_{\pm}(k_z) = \pm v_F |k_z|$. In particular, the eigenstates of this Hamiltonian are given by $\left|d_{\pm}(r,\theta)\right\rangle = \left|\gamma_+(r,\theta)\right\rangle \pm i \left|\gamma_-(r,\theta)\right\rangle$, which are related by particle-hole symmetry $\mathcal{P} \left|d_{\pm}(r,\theta)\right\rangle = \left|d_{\mp}(r,\theta)\right\rangle$. Therefore for $k_z \neq 0$, the two Majorana modes on a vortex line are paired to form a particle/hole pair of 1D relativistic Dirac fermions. This Dirac mode is stable, and is protected by the same mirror symmetry that protects the surface states.
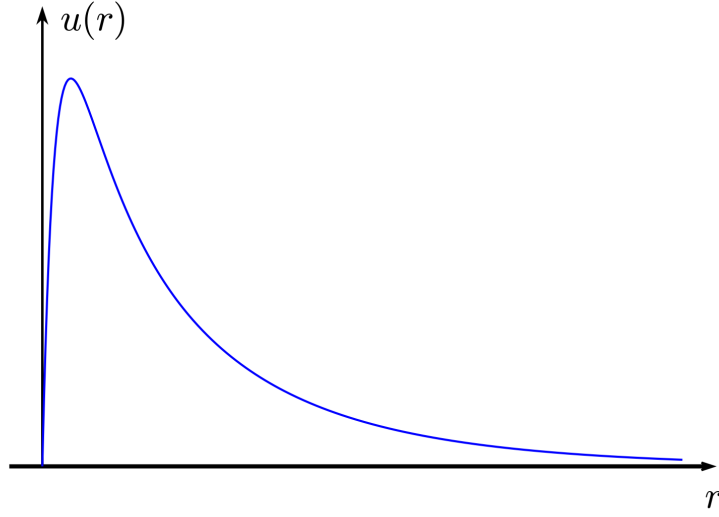
(a)
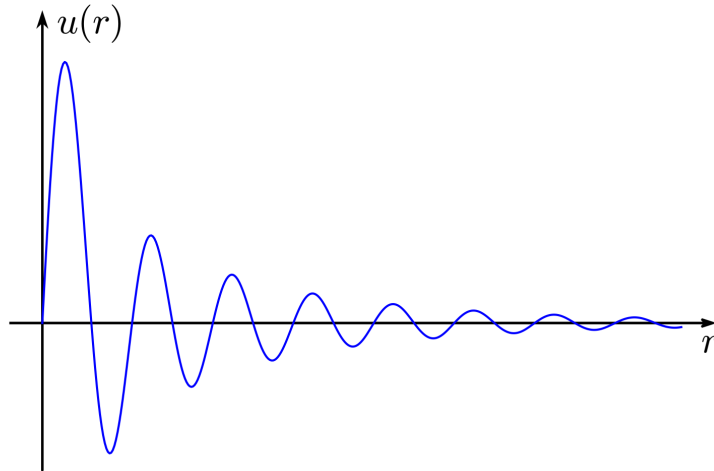
(b)

Figure 4.7: Radial amplitude $u(r)$ of the Majorana zero modes in a chiral p-wave nodal-loop semimetal. The amplitude is given by Eq. (4.45) and is plotted in the cases of (a) weak pairing $|\Delta_0|^2 < 4Q^2$ and (b) strong pairing $|\Delta_0|^2 > 4Q^2$ in the approximation of an infinitesimally small vortex core with vorticity $\ell = 1$ (see Eqs. (4.48),(4.49)).

Chapter 5

Conclusion

In Part I of this thesis, the effect of electronic pairing interactions at the BCS mean-field level was investigated. In Sec. 4.2, it was found that s-wave pairing only gaps the nodal-loop in the limit of strong coupling, resulting in a topologically trivial gapped superconductor. On the other hand, a chiral p-wave pairing term fully gaps the nodal-loop at weak pairing, while preserving the mirror symmetry that protects the drumhead surface states. It was then shown in Sec. 4.3 the chiral p-wave state hosts a gapless Dirac mode at the core of a vortex line, protected by the same mirror symmetry. This result highlights that the topological order of a nodal-loop can remain stable in the presence of interactions.

A natural next step would be to investigate the electromagnetic response of the nodal-loop with chiral p-wave pairing. As discussed in Sec. 3.3, the topological response corresponds to an induced magnetization and polarization, characterized by the geometry of the nodal-loop. It is thus expected that such a response would persist in the chiral p-wave state.

Part II

The nature of spin-orbit coupling in $Lu_2V_2O_7$

Chapter 6

Introduction

Since the early days of materials science, physicists have been interested in understanding the magnetic properties of materials. This progress was accelerated with the development of quantum mechanics in the past century, which provided a microscopic descriptions of the origin of magnetism. Since then, the study of magnetism has been a pervasive topic the field of condensed matter physics. Central to much of the phenomenology in this field is the concept of magnetic ordering, where magnetic moments of ions in an insulator will typically order in some arrangement at low temperature.

Of particular interest in the last several decades are the rare-earth pyrochlore oxides, described by the chemical formula $A_2B_2O_7$. This class of materials host many exotic phases of matter that typically arise from geometrically frustrated magnetic interactions, where a system is unable so simultaneously minimize a collection of local interactions [62]. Another geometric feature of the pyrochlore oxides are the crystallographic symmetries, or rather lack thereof, which allow for a spin-orbit effect known as the Dzyaloshinskii-Moriya (DM) interaction [63, 64]. This interaction has been associated with a variety of magnetic phenomena, such as spiral magnetic ordering and magnetoelectric effects [65].

In magnetically ordered materials, thermal fluctuations lead to deviations of the local magnetic order, which can propagate through the material. These so-called spin waves carry angular momentum and energy, and in cases where quantum fluctuations are relevant, these waves are canonically quantized to quasiparticles known as magnons. When translational symmetry is present, these magnons have a well defined spectrum and corresponding Block wavefunctions. It was first predicted by Katsura *et al.*, that the DM interaction is a route to magnons acquiring topological order, in the form of a non-zero Berry curvature of the Bloch wavefunctions, and an associated anomalous Hall effect [66].

While magnons are electrically neutral, such an effect is observable in thermal transport measurements, as a transverse heat current in response to a thermal gradient.

This prediction of a thermal Hall effect of magnons [66] was confirmed by Onose *et al.* through thermal transport measurements of the ferromagnetic pyrochlore oxide $Lu_2V_2O_7$ [67]. Additionally, this provided the first experimental evidence of the DM interaction in this material. Given that the only magnetic ions of this material are the V^{4+} ions, a transition metal where spin-orbit effects are weak, it was surprising that fitting the thermal transport measurements predicted a relatively large DM interaction: approximately 32% of the ferromagnetic Heisenberg exchange.

The magnitude of the DM interaction in $A_2B_2O_7$ was further called into question when subsequent density-functional theory (DFT) calculations [68, 69] and inelastic neutron scattering measurements [70] reported a DM interaction in the range of $5 - 18\%$ of the Heisenberg exchange. Furthermore, it was pointed out later by Matsumoto and Murakami [71, 72], that the calculation of the thermal Hall conductivity used by Onose *et al.* [67] was missing a term corresponding to the orbital motion of the magnons. This calls for a re-investigation of the thermal conductivity data from Ref. [67] to try and resolve this apparent discrepancy regarding the magnitude of the DM interaction in $Lu_2V_2O_7$ between thermal conductivity measurements, inelastic neutron scattering measurements [70], and DFT calculations [68, 69], which is the focus for the remainder of this thesis.

Part II of this thesis is outlined as follows. Chapter 7 provides a general overview of the magnetic properties of $Lu_2V_2O_7$ and motivate an effective low-energy model. In addition, Sec. 7.3 provides a general overview of the DM interaction in pyrochlore magnets. Chapter 8 details the magnon Hall effect in $Lu_2V_2O_7$, including the formalism developed by Matsumoto and Murakami. In Sec. 8.4, the thermal Hall conductivity data by Onose *et al.* is re-examined using this formalism, and the magnitude of the DM interaction is determined in this context. Chapter 9 summarizes this result, and it is argued that further investigation into the nature of spin-orbit coupling in $Lu_2V_2O_7$ is required.

Chapter 7

Microscopic model of $\mathrm{Lu_2V_2O_7}$

This chapter outlines the microscopic details and low-energy theory of $\mathrm{Lu_2V_2O_7}$. The chapter starts with an overview of rare-earth pyrochlores and the pyrochlore lattice in Sec. 7.1. A microscopic model for $\mathrm{Lu_2V_2O_7}$ is then motivated from microscopic principles in Sec. 7.2, and the DM interaction is discussed in detail in Sec. 7.3.

7.1 Rare-earth pyrochlore oxides

The past several decades have seen an immense interest in the magnetic properties of rare-earth pyrochlore oxides. The geometry of these these oxides allows for geometric frustration, leading to exotic magnetic phases of matter such as spin-liquid, spin-ice, and spin-glass phases [73–75].

The rare-earth pyrochlore oxides are described by the chemical formula $\mathrm{A_2B_2O_7}$, where $\mathrm{A^{3+}}$ denotes a rare-earth ion and $\mathrm{B^{4+}}$ typically denotes a transition metal ion, either of which can be magnetic. These materials crystallize in such a way that both the A and B sites independently form a lattice of corner-sharing tetrahedra, a configuration known as the pyrochlore lattice [74]. The pyrochlore lattice, as depicted in Fig. 7.1, is a face-centered cubic (FCC) lattice consisting of one tetrahedron (i.e. 4 sites) per unit cell, and is thus characterized by a single lattice constant a. By defining a set of FCC primitive lattice vectors

$$\boldsymbol{a}_1 = \frac{a}{2}\left(\hat{\boldsymbol{x}} + \hat{\boldsymbol{y}}\right) \qquad \boldsymbol{a}_2 = \frac{a}{2}\left(\hat{\boldsymbol{y}} - \hat{\boldsymbol{z}}\right) \qquad \boldsymbol{a}_3 = \frac{a}{2}\left(\hat{\boldsymbol{x}} - \hat{\boldsymbol{z}}\right), \tag{7.1}$$

the position of each point on the pyrochlore lattice can be written as $\boldsymbol{R}_{n_1 n_2 n_3 \alpha} = n_1 \boldsymbol{a}_1 + n_2 \boldsymbol{a}_2 + n_3 \boldsymbol{a}_3 + \boldsymbol{s}_\alpha$, where n_1, n_2, n_3 are integers labelling the position on the FCC lattice,
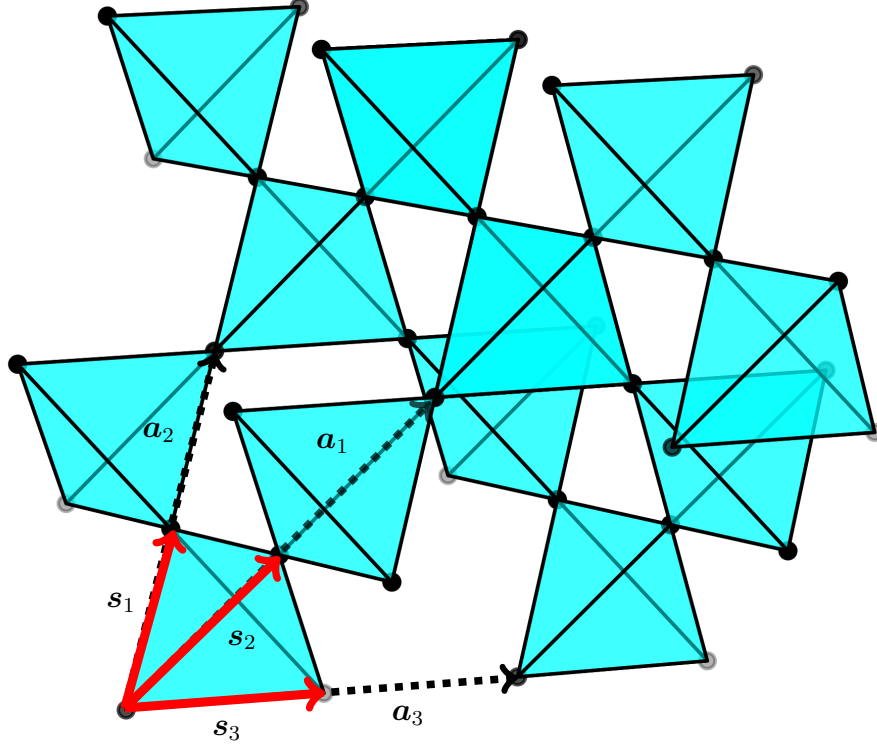
Figure 7.1: Diagram of the pyrochlore lattice, where the periodic arrangement of atoms form a network of corner-sharing tetrahedra. The FCC lattice vectors defined in Eq. (7.1) are depicted by the black dashed lines, while the sublattice vectors defined in Eq. (7.2) are depicted in red.

and $\boldsymbol{s}_\alpha$ ($\alpha = 0, 1, 2, 3$), is a sublattice vector that connects the site labelled 0 to the site labelled α within a single unit cell. We take the sublattice vectors to be

$$\boldsymbol{s}_0 = \boldsymbol{0} \qquad \boldsymbol{s}_1 = \frac{a}{4} \left(\hat{\boldsymbol{y}} - \hat{\boldsymbol{z}} \right) \qquad \boldsymbol{s}_2 = \frac{a}{4} \left(\hat{\boldsymbol{x}} + \hat{\boldsymbol{y}} \right) \qquad \boldsymbol{s}_3 = \frac{a}{4} \left(\hat{\boldsymbol{x}} - \hat{\boldsymbol{z}} \right). \qquad (7.2)$$

A single unit cell, along with the coordinate system defined by Eq. (7.2) is depicted in Fig. 7.3, along with a set of indirect DM vectors for pyrochlore lattice, which is discussed in Sec. 7.3. The remainder of this thesis is focused on the rare-earth pyrochlore $Lu_2V_2O_7$, in which the magnetic V^{4+} ions form a pyrochlore lattice.

7.2   An emergent $S = 1/2$ magnetic insulator

This section outlines and motivates an effective low-energy model to describe the magnetism in $Lu_2V_2O_7$. As described in Sec. 7.1, the Lu^{3+} and V^{4+} ions each crystallize to a pyrochlore lattice, with FCC lattice constant $a = 9.94$ Å. In the presence of spin-orbit coupling, which is generally strong in rare-earth ions, a good quantum number to describe the single-ion physics is the total angular momentum quantum number J, determined by Hund's rules. In the case of Lu^{3+}, the electronic configuration is given by

$$1s^2 2s^2 2p^6 3s^2 3p^6 4s^2 3d^{10} 4p^6 5s^2 4d^{10} 5p^6 4f^{14},$$

which clearly has $J = 0$ as every electronic subshell is filled. Alternatively, transition metal ions such as V^{4+} have a relatively weak spin-orbit interaction. The electronic configuration of V^{4+} is given by

$$1s^2 2s^2 2p^6 3s^2 3p^6 3d^1,$$

which would correspond to a total angular momentum $J = 3/2$ after an application of Hund's rules. It follows that only the V^{4+} ions carry a magnetic moment, arising from the single valence 3d-orbital electron. A very important subtlety here is that the V^{4+} ions do not exist in a vacuum. In general, there is electrostatic interactions with the surrounding Lu^{3+} and O^{2-} ions, which breaks the four-fold degeneracy corresponding to the $J = 3/2$ angular momentum states. In addition, these so-called *crystal field effects* mix the energy levels of the five states within the 3d subshell, although these effects are generally not strong enough to mix states in different shells. In transition metal ions, crystal field effects tend to dominate over the spin-orbit interactions, the total angular-momentum J is no longer a good quantum number. In this case, we must treat the spin and orbital angular momentum quantum numbers, denoted by S and L respectively, independent of one another. In the case of V^{4+}, these correspond to $S = 1/2$ and $L = 2$.

Many of the essential features of how the crystal field splits the energy levels can be determined through crystallographic symmetries that leave the V^{4+} atoms unchanged, known as *point-group symmetries*. In particular, the pyrochlore oxides correspond to the space group $Fd\bar{3}m$, which leads to a crystal field splitting of the d-orbitals with trigonal symmetry [76]. This crystal field splitting of the five d-orbital states is depicted in Fig. 7.2, with the lowest energy corresponding to a single d_{z^2} orbital, separated by a gap of $\Delta_0 \approx 4,600$ K [77, 78].

An important consequence of the trigonal field splitting scheme is that the orbital angular momentum becomes quenched when there is no longer mixing between orbitals [79], which we can assume to be the case at low enough temperature. Angular momentum
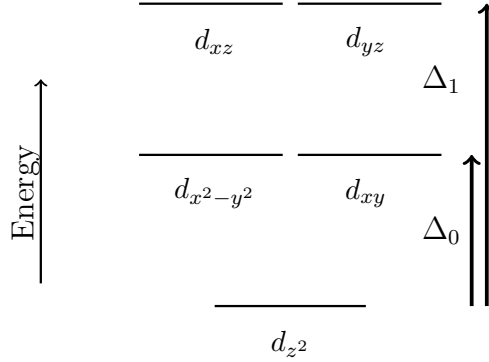
Figure 7.2: Crystal field splitting of the d-orbital V^{4+} ion in $Lu_2V_2O_7$, where $\Delta_0 \approx 4,600$ K and $\Delta_1 \approx 23,000$ K [77,78]

quenching occurs because the crystal field breaks full rotational symmetry, so that the components of the orbital angular momentum are not necessarily a conserved quantity. In cases where the crystal field splitting leads to a single orbital ground state configuration, which is the case for the trigonal field splitting depicted in Fig. 7.2, the corresponding ground state wavefunction will be real (up to a global phase), and the orbital angular momentum will average to zero [79]. Because of this, we may effectively ignore the orbital component of angular momentum, and expect that magnetic interactions occur only at the level of the $S = 1/2$ spin component of the single valence 3d electron of each V^{4+} atom. As a result, quantum effects are expected to be crucial as the low-energy physics maps onto a two-level model.

The final aspect to address is the nature of magnetic interactions in $Lu_2V_2O_7$. This material has been determined to order as a collinear ferromagnet below $T_c = 73$ K [80, 81]. It was suggested in Ref. [78] that the ferromagnetic correlations between V^{4+} ions arises from virtual hopping processes between the lowest energy d_{z^2} orbital, and the higher energy orbitals in Fig. 7.2.

This motivates the general form of a low-energy ferromagnetic spin-1/2 Hamiltonian for $Lu_2V_2O_7$ in a magnetic field as

$$\mathcal{H} = \sum_{\langle i,j \rangle} \sum_{\mu\nu} \mathcal{J}_{i,j}^{\mu,\nu} S_i^\mu S_j^\nu - \mu_B g \sum_i \boldsymbol{H} \cdot \boldsymbol{S}_i \tag{7.3}$$

where i, j label the sites on a pyrochlore lattice, μ, ν label the spin indices, and $\langle ... \rangle$ indicates the sum be taken over nearest neighbours. Here, $\boldsymbol{H}$ is an external magnetic field, $g \approx 2$ and μ_B is the Bohr magneton. The exchange matrix $\mathcal{J}_{i,j}^{\mu,\nu}$ has been studies from first principles

using DFT in Ref. [69], where it was determined that the off-diagonal symmetric exchange is relatively small compared with the other energy scales $\mathcal{J}_{i,j}^{\mu,\nu} + \mathcal{J}_{i,j}^{\nu,\mu} \approx 0$ for $\mu \neq \nu$. The Hamiltonian in Eq. (7.3) can thus be written as

$$\mathcal{H} = -J\sum_{\langle i,j \rangle} \boldsymbol{S}_i \cdot \boldsymbol{S}_j + \sum_{\langle i,j \rangle} \boldsymbol{D}_{ij} \cdot (\boldsymbol{S}_i \times \boldsymbol{S}_j) - \mu_{\mathrm{B}}g\sum_i \boldsymbol{H} \cdot \boldsymbol{S}_i, \qquad (7.4)$$

where $J > 0$ represents the ferromagnetic Heisenberg exchange, and $\boldsymbol{D}_{ij}$ is a set of vectors, representing the antisymmetric off-diagonal exchange. This antisymmetric exchange is known as the Dzyaloshinskii-Moriya (DM) interaction, and is discussed in more detail in the following Sec. 7.3.

7.3 The DM interaction

The discovery of antisymmetric magnetic exchange dates back to the 1950s, as an explanation by Dzyaloshinskii for measurements of weak ferromagnetic moments in the typically antiferromagnetic materials α-Fe_3O_3, $MnCO_3$, and $CoCO_3$ [63]. Subsequently, Moriya identified that the microscopic mechanism for this exchange to be of spin-orbit coupling origin [64]. In particular, it was shown that the term $\boldsymbol{D}_{ij} \cdot (\boldsymbol{S}_i \times \boldsymbol{S}_j)$ in Eq. (7.4) arises at lowest order in a perturbative analysis of the spin-orbit coupling term between two magnetic ions. This interaction has since become known as the Dzyaloshinskii–Moriya (DM) interaction, and the set of vectors $\boldsymbol{D}_{ij}$ are known as the DM vectors.

Another important aspect of the DM interaction, discussed in Moriya's original publication [64], is that the direction of the DM vectors $\boldsymbol{D}_{ij}$ are highly constrained by crystallographic symmetries. Specifically, Moriya determined a set of five rules to constrain the DM vector orientation, which are reproduced from Ref. [64] here. Let A and B denote the location of two magnetic ions, with the point bisecting the straight line between them $\overline{AB}$ denoted by C. The following rules apply to the DM vector $\boldsymbol{D}$ between the two ions:

1. When a center of inversion is located at C, $\boldsymbol{D} = 0$.

2. When a mirror plane perpendicular to $\overline{AB}$ passes through C, then $\boldsymbol{D} = 0$ is parallel to the mirror plane or $\boldsymbol{D}$ is perpendicular to $\overline{AB}$.

3. When there is a mirror plane including A and B, then $\boldsymbol{D}$ is perpendicular to the mirror plane.

4. When a two-fold rotation axis perpendicular to $\overline{AB}$ passes through C, then $\boldsymbol{D}$ is perpendicular to this two-fold axis.

5. When there is an $n-$fold axis ($n \geq 2$) along $\overline{AB}$, then $\boldsymbol{D}$ is parallel to $\overline{AB}$.

Moriya's rules, when applied to the pyrochlore lattice, lead to two possible configurations of the nearest-neighbour DM vectors [82]. These two configurations are simply related by a minus sign ($\boldsymbol{D} \to -\boldsymbol{D}$) and are referred to as *direct* and *indirect* cases [82]. DFT calculations have suggested that $Lu_2V_2O_7$ has an indirect DM vector configuration [69]. In the coordinates defined by the sublattice vectors in Eq. (7.2), the indirect DM vectors for the pyrochlore lattice are given by

$$\boldsymbol{D}_{01} = \frac{D}{\sqrt{2}} \left(-\hat{\boldsymbol{y}} - \hat{\boldsymbol{z}}\right) \qquad \boldsymbol{D}_{02} = \frac{D}{\sqrt{2}} \left(\hat{\boldsymbol{y}} - \hat{\boldsymbol{x}}\right) \qquad \boldsymbol{D}_{03} = \frac{D}{\sqrt{2}} \left(\hat{\boldsymbol{x}} + \hat{\boldsymbol{z}}\right) \qquad (7.5)$$

$$\boldsymbol{D}_{13} = \frac{D}{\sqrt{2}} \left(-\hat{\boldsymbol{x}} - \hat{\boldsymbol{y}}\right) \qquad \boldsymbol{D}_{12} = \frac{D}{\sqrt{2}} \left(\hat{\boldsymbol{x}} - \hat{\boldsymbol{z}}\right) \qquad \boldsymbol{D}_{23} = \frac{D}{\sqrt{2}} \left(\hat{\boldsymbol{y}} - \hat{\boldsymbol{z}}\right),$$

with the magnitude D a microscopic parameter that depends on the magnitude of spin-orbit coupling between magnetic ions. One of the DM vectors $\boldsymbol{D}_{01}$ is depicted in Fig. 7.3 for a single tetrahedron. Note that since the DM interaction in Eq. (7.4) is proportional to the cross product of two spin operators, so it is antisymmetric upon swapping two ions, which implies that $\boldsymbol{D}_{ij} = -\boldsymbol{D}_{ji}$.

Further theoretical work has been carried out more recently, to better understand the microscopic origin of the DM interaction in $Lu_2V_2O_7$. The existence of a finite DM interaction was reported in Ref. [69] using DFT calculations on a model of a d$-$orbital Mott insulator with spin-orbit coupling. A subsequent strong coupling analysis of this model was carried out in Ref. [83]. It was suggested that the DM interaction results from the superexchange between two neighbouring V^{4+} ions, mediated by an intermediate O^{2-} anion, and is strongly dependent on the angle of the V-O-V bond.

It was first predicted by Katsura *et al.* that the DM interaction can induce a thermal Hall effect [66]. This effect in the context of $Lu_2V_2O_7$ is the subject of Chapter 8.
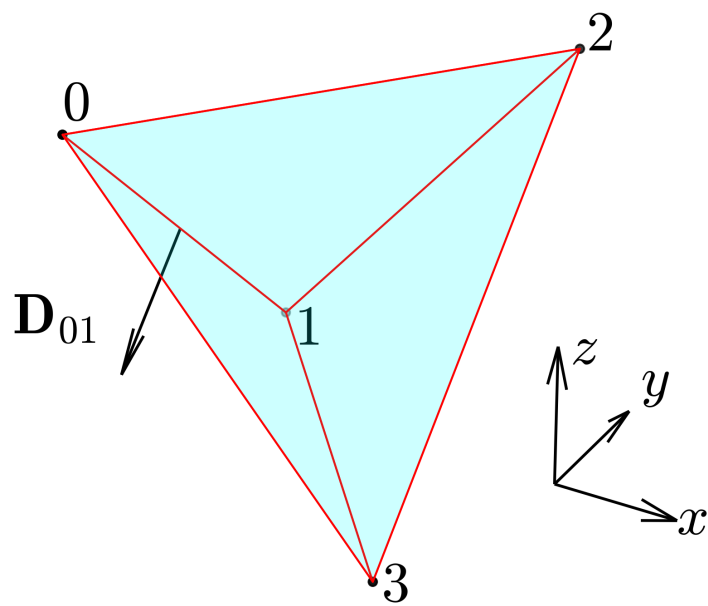
Figure 7.3: Example of an indirect DM vector $\boldsymbol{D}_{01}$ as defined in Eq. (7.5), depicted on a single tetrahedron of the pyrochlore lattice.

Chapter 8

Magnon Hall effect in $Lu_2V_2O_7$

With the low-energy description of $Lu_2V_2O_7$ developed in Chapter 7, this chapter describes the thermal Hall effect in this material, first measured in Ref. [67]. Section 8.1 is an introduction to magnons, followed by a derivation of an effective magnon Hamiltonian for $Lu_2V_2O_7$. Section 8.2 subsequently describes the theory of the magnon Hall effect, as developed in Ref. [71]. Section 8.3 and Sec. 8.4 describes the thermal Hall conductivity measurements from Ref. [67], where the data is fit to find the magnitude of the DM interaction. The result suggests that further investigation into the nature of spin-orbit coupling in $Lu_2V_2O_7$ is necessary.

8.1 Quantum spin-waves

When the magnetic moments in a material become ordered, such as the collinear ferromagnetic ordering of $Lu_2V_2O_7$ below $T_c = 73K$, thermal fluctuations distort the local magnetic ordering axis of an ion. To lowest order, these distortions propagate coherently through the lattice, creating a *spin-wave*, and the quantum of a spin-wave is known as a *magnon*. In the quantum picture, the eigenvalues of a spin operator always differ by an integer amount. A magnon, representing a change in spin, thus carry an integer spin and obey Bose-Einstein statistics. Although magnons do not carry charge, they do carry energy, as the change in an ordered spin configuration comes at an energy cost due to the magnetic exchange interactions.

Given that magnons correspond to fluctuations about an ordered spin configuration, it is most convenient to work in a basis that is locally oriented along the ordered spin of each

ion. For a spin located at position $\boldsymbol{r}_i$, define the orthonormal triad $\{\hat{\boldsymbol{u}}_i, \hat{\boldsymbol{v}}_i, \hat{\boldsymbol{w}}_i\}$, with $\hat{\boldsymbol{w}}_i$ the unit vector in the direction of the spin, and $\hat{\boldsymbol{u}}_i, \hat{\boldsymbol{v}}_i$ chosen such that $\hat{\boldsymbol{u}}_i \times \hat{\boldsymbol{v}}_i = \hat{\boldsymbol{w}}_i$.

The relationship between spin operators in a magnetically ordered state and the bosonic magnon operators was first suggested by Holstein and Primakoff [84], and is given by

$$
\begin{aligned}
S_i^+ &= \sqrt{2S - b_i^\dagger b_i} \, b_i \\
S_i^- &= b_i^\dagger \sqrt{2S - b_i^\dagger b_i} \\
S_i^{w_i} &= S - b_i^\dagger b_i,
\end{aligned}
\tag{8.1}
$$

with $b_i^\dagger$ (b_i) interpreted as a magnon creation (annihilation) operator, satisfying $[b_i, b_j] = 0$ and $\left[b_i, b_j^\dagger\right] = \delta_{ij}$. Here, $S_i^{w_i}$ corresponds to the spin operator oriented in the direction of $\hat{\boldsymbol{w}}_i$, and $S_i^{\pm} = S_i^{u_i} \pm i S_i^{v_i}$ are the corresponding spin raising and lowering operators. This transformation can be understood as a magnon being created by lowering the expected value of the operator $S_i^{w_i}$, due to fluctuations about the spin ordering axis. The operator appearing in the square root is necessary to account for the fact that the spectrum of the spin operators is bounded, while the spectrum of the bosonic operators is not. The Holstein-Primakoff transformation of spin operators results in a generic many-body Hamiltonian of bosonic operators, including interaction terms. To obtain a more useful low-energy theory, we assume that the spin-waves are linear, in the sense that we only consider terms up to quadratic order in the bosonic operators. This ignores the effective magnon self-interaction terms generated by the bounded spectrum of spin operators, which is a valid assumption whenever $\left\langle b_i^\dagger b_i \right\rangle \ll 2S$.

The regime of linear spin-waves is obtained by expanding in Eq. (8.1) in powers of $b_i^\dagger b_i / 2S$ to lowest order, leading to

$$
\begin{aligned}
S_i^+ &\approx \sqrt{2S} b_i \\
S_i^- &\approx \sqrt{2S} b_i^\dagger \\
S_i^{w_i} &= S - b_i^\dagger b_i.
\end{aligned}
\tag{8.2}
$$

We can then obtain an effective Hamiltonian for linear spin-waves in $Lu_2V_2O_7$ by plugging this transformation of spin operators into the Hamiltonian Eq. (7.4). It was found in Ref. [85] that the magnetic moments saturate to approximately $1\mu_B$ at magnetic fields above 1T, which is accessible experimentally, so we assume that the spins order parallel to the applied magnetic field, i.e. $\hat{\boldsymbol{w}}_i = \boldsymbol{H}/|\boldsymbol{H}|$ for every spin on the pyrochlore lattice. It

is thus be convenient to work in the *global basis* $\{\hat{\boldsymbol{u}}, \hat{\boldsymbol{v}}, \hat{\boldsymbol{w}}\}$, with $\hat{\boldsymbol{w}}$ parallel to the applied magnetic field and $\hat{\boldsymbol{u}} \times \hat{\boldsymbol{v}} = \hat{\boldsymbol{w}}$. The DM vectors defined in Eq. (7.5) can then be represented in this basis as

$$\boldsymbol{D}_{ij} = D_{ij}^u \hat{\boldsymbol{u}} + D_{ij}^v \hat{\boldsymbol{v}} + D_{ij}^w \hat{\boldsymbol{w}}. \tag{8.3}$$

The DM interaction, after substituting the linearized Holstein-Primakoff transformation from Eq. (8.2) becomes

$$\boldsymbol{D}_{ij} \cdot (\boldsymbol{S}_i \times \boldsymbol{S}_j) = S\sqrt{\frac{S}{2}} \left[i \left(b_i^\dagger - b_j^\dagger + b_j - b_i \right) D_{ij}^u - \left(b_i^\dagger + b_i - b_j^\dagger - b_j \right) D_{ij}^v \right] \tag{8.4}$$
$$+ iS \left(b_j^\dagger b_i - b_i^\dagger b_j \right) D_{ij}^w.$$

By rewriting

$$\boldsymbol{D}_{ij} \cdot (\boldsymbol{S}_i \times \boldsymbol{S}_j) = \frac{1}{2} \boldsymbol{D}_{ij} \cdot (\boldsymbol{S}_i \times \boldsymbol{S}_j - \boldsymbol{S}_j \times \boldsymbol{S}_i), \tag{8.5}$$

and plugging in the right-hand side of Eq. (8.4), each of the terms proportional to D_{ij}^u and D_{ij}^v vanish, such that only the component of the DM vector parallel to the applied magnetic field contributes to the linear spin-wave Hamiltonian. Furthermore, we have

$$\boldsymbol{S}_i \cdot \boldsymbol{S}_j \approx S^2 - S \left(b_i^\dagger b_i + b_j^\dagger b_j \right) + S \left(b_i^\dagger b_j + b_j^\dagger b_i \right), \tag{8.6}$$

and

$$\boldsymbol{H} \cdot \boldsymbol{S}_i = H \left(S - b_i^\dagger b_i \right), \tag{8.7}$$

where $H \equiv |\boldsymbol{H}|$ is the magnitude of the applied magnetic field. By setting $S = 1/2$, the full spin-wave Hamiltonian for $Lu_2V_2O_7$ is thus given by

$$\mathcal{H} = \mathcal{E}_0 - \sum_{\langle i,j \rangle} \left[\left(J + iD_{ij}^w \right) b_i^\dagger b_j + \left(J - iD_{ij}^w \right) b_j^\dagger b_i \right] + \sum_i \left(\mu_\mathrm{B} g H + 3J \right) b_i^\dagger b_i, \tag{8.8}$$

where $\mathcal{E}_0 \equiv -3JN - 2\mu_\mathrm{B} g H N$ is the ground state energy and N is the number of unit cells (i.e. $4N$ is the number of V^{4+} ions). This can be simplified further by defining $J_{ij} \equiv \sqrt{J^2 + \left(D_{ij}^w \right)^2}$ and $\phi_{ij} \equiv \tan^{-1} \left(D_{ij}^w / J \right)$, so that

$$\mathcal{H} = \mathcal{E}_0 - \sum_{\langle i,j \rangle} J_{ij} \left[e^{i\phi_{ij}} b_i^\dagger b_j + e^{-i\phi_{ij}} b_j^\dagger b_i \right] + \sum_i \left(\mu_\mathrm{B} g H + 3J \right) b_i^\dagger b_i. \tag{8.9}$$

To diagonalize this Hamiltonian, we can take the Fourier transform of the magnon operators corresponding to each sublattice type. Suppose that a given site labelled by index i

corresponds to a site on sublattice type α as defined in Fig. 7.3, then the Fourier transform is given by

$$b_i = \frac{1}{\sqrt{N}} \sum_{\boldsymbol{k}} e^{i\boldsymbol{k}\cdot\boldsymbol{R}_i} b_\alpha(\boldsymbol{k}), \tag{8.10}$$

where the sum is taken over all crystal momenta $\boldsymbol{k}$ in the first Brillouin zone of the FCC lattice. It follows that

$$\sum_{i\in\alpha} b_i^\dagger b_i = \sum_{\boldsymbol{k}} b_\alpha^\dagger(\boldsymbol{k}) b_\alpha(\boldsymbol{k}). \tag{8.11}$$

Furthermore, if we define $\boldsymbol{s}_{\alpha\alpha'} \equiv \boldsymbol{s}_{\alpha'} - \boldsymbol{s}_\alpha$, with $\boldsymbol{s}_\alpha$ defined in Eq. (7.2), to be the nearest-neighbour vector that connects a site of sublattice type α to a site of sublattice type α', then

$$\sum_{i\in\alpha} b_i^\dagger b_{i+\boldsymbol{s}_{\alpha\alpha'}} = \sum_{\boldsymbol{k}} e^{i\boldsymbol{k}\cdot\boldsymbol{s}_{\alpha\alpha'}} b_\alpha^\dagger(\boldsymbol{k}) b_{\alpha'}(\boldsymbol{k}). \tag{8.12}$$

By defining a generalized magnon operator

$$B(\boldsymbol{k}) \equiv \begin{pmatrix} b_0(\boldsymbol{k}) & b_1(\boldsymbol{k}) & b_2(\boldsymbol{k}) & b_3(\boldsymbol{k}) \end{pmatrix}^T,$$

and noting that $J_{ij} = J/\cos(\phi_{ij})$, the spin wave Hamiltonian becomes

$$\mathcal{H} = \mathcal{E}_0 + \sum_{\boldsymbol{k}} B^\dagger(\boldsymbol{k}) \mathcal{M}(\boldsymbol{k}) B(\boldsymbol{k}), \tag{8.13}$$

with

$$\mathcal{M}(\boldsymbol{k}) \equiv \begin{pmatrix} 3J + \mu_{\mathrm{B}}gH & -Je^{i\phi_{12}}\frac{\cos(\boldsymbol{k}\cdot\boldsymbol{s}_{12})}{\cos(\phi_{12})} & -Je^{i\phi_{13}}\frac{\cos(\boldsymbol{k}\cdot\boldsymbol{s}_{13})}{\cos(\phi_{13})} & -Je^{i\phi_{14}}\frac{\cos(\boldsymbol{k}\cdot\boldsymbol{s}_{14})}{\cos(\phi_{14})} \\ -Je^{-i\phi_{12}}\frac{\cos(\boldsymbol{k}\cdot\boldsymbol{s}_{12})}{\cos(\phi_{12})} & 3J + \mu_{\mathrm{B}}gH & -Je^{i\phi_{23}}\frac{\cos(\boldsymbol{k}\cdot\boldsymbol{s}_{23})}{\cos(\phi_{23})} & -Je^{i\phi_{24}}\frac{\cos(\boldsymbol{k}\cdot\boldsymbol{s}_{24})}{\cos(\phi_{24})} \\ -Je^{-i\phi_{13}}\frac{\cos(\boldsymbol{k}\cdot\boldsymbol{s}_{13})}{\cos(\phi_{13})} & -Je^{-i\phi_{23}}\frac{\cos(\boldsymbol{k}\cdot\boldsymbol{s}_{23})}{\cos(\phi_{23})} & 3J + \mu_{\mathrm{B}}gH & -Je^{i\phi_{34}}\frac{\cos(\boldsymbol{k}\cdot\boldsymbol{s}_{34})}{\cos(\phi_{34})} \\ -Je^{-i\phi_{14}}\frac{\cos(\boldsymbol{k}\cdot\boldsymbol{s}_{14})}{\cos(\phi_{14})} & -Je^{-i\phi_{24}}\frac{\cos(\boldsymbol{k}\cdot\boldsymbol{s}_{24})}{\cos(\phi_{24})} & -Je^{-i\phi_{34}}\frac{\cos(\boldsymbol{k}\cdot\boldsymbol{s}_{34})}{\cos(\phi_{34})} & 3J + \mu_{\mathrm{B}}gH \end{pmatrix}. \tag{8.14}$$

The spin wave dispersion is then obtained by diagonalizing $\mathcal{M}(\boldsymbol{k})$ for each $\boldsymbol{k}$ in the first Brillouin zone. Since the magnetic field enters in a term proportional to the identity matrix, it is clear that this term simply leads to an overall gap in the magnon spectrum. The dispersion is shown in Fig. 8.1 for both the case of no DM interaction ($D/J = 0$) and a finite DM interaction ($D/J = 0.18$). The finite value of $D/J = 0.18$ corresponds to the result from Mena *et al.* [70] obtained by fitting the magnon dispersion to inelastic neutron scattering data, in agreement with Fig. 8.1(b).
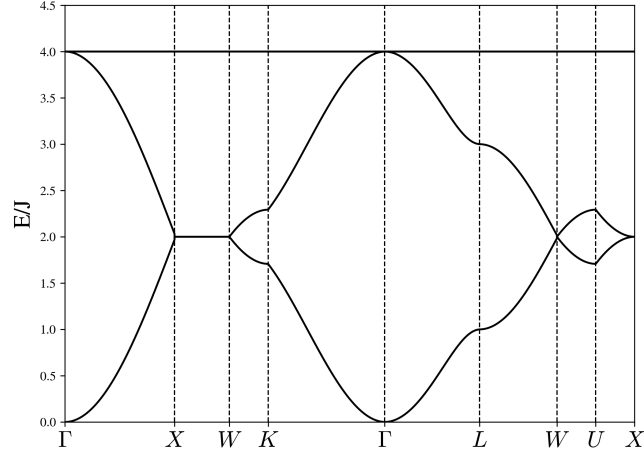
(a)
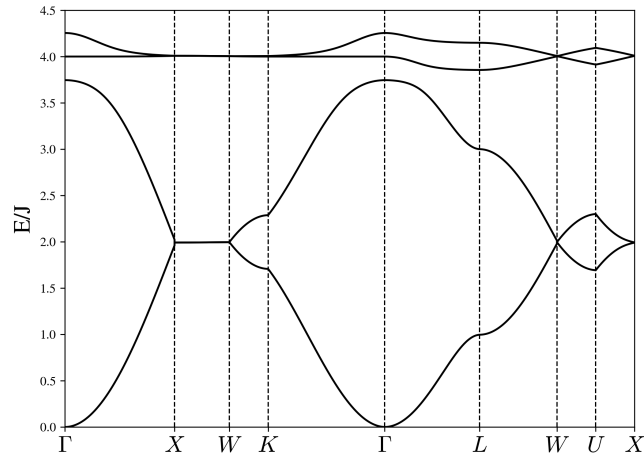
(b)

Figure 8.1: Calculated magnon dispersion for $Lu_2V_2O_7$, obtained by diagonalizing the matrix in Eq. (8.14) for (a) $D/J = 0$ and (b) $D/J = 0.18$. Plotted is the energy relative to the magnon gap $g\mu_B H$, in units of J.

In the case where there is no DM interaction ($\boldsymbol{D}_{ij} = 0$), we can obtain an exact expression for the magnon dispersion by diagonalizing Eq. (8.14) using Mathematica. The solution corresponds to two degenerate flat bands at $E = 4J + \mu_{\mathrm{B}} g H$, and two dispersive bands, given by

$$E_{\pm}(\boldsymbol{k}) = 2J + \mu_{\mathrm{B}} g H$$
$$\pm J \sqrt{1 + \cos\left(\frac{k_x a}{2}\right) \cos\left(\frac{k_y a}{2}\right) + \cos\left(\frac{k_x a}{2}\right) \cos\left(\frac{k_z a}{2}\right) + \cos\left(\frac{k_y a}{2}\right) \cos\left(\frac{k_z a}{2}\right)}.$$

Because the magnons obey Bose-Einstein statistics, the low-energy dynamics are governed by states in the vicinity of the Γ high symmetry point ($\boldsymbol{k} = 0$). Expanding the lowest energy band around this point, we obtain a low-energy quadratic dispersion

$$E_-(\boldsymbol{k}) \approx \mu_{\mathrm{B}} g H + \frac{J a^2}{16} |\boldsymbol{k}|^2. \tag{8.15}$$

By including a finite DM interaction ($\boldsymbol{D}_{ij} \neq 0$), the two flat bands at finite energy become dispersive, while the lowest energy magnon band remains unchanged around the Γ high symmetry point ($\boldsymbol{k} = 0$), as seen in Fig. 8.1. This is confirmed by numerically diagonalizing Eq. (8.14) in the presence of a finite DM interaction, where it is found that Eq. (8.15) remains valid up to second order in $|\boldsymbol{k}|$.

8.2   Theory of the Magnon Hall effect

Perhaps the simplest example of a topological insulator is a two-dimensional Chern insulator, discussed briefly in Sec. 2.2. In such a system, an in-plane electric field $\boldsymbol{E} = E_y \hat{\boldsymbol{y}}$ generates an electrical current with components that are perpendicular to $\boldsymbol{E}$. The transverse component of the electrical current in this case, is given by $j_x = \sigma_{xy} E_y$, with quantized Hall conductivity

$$\sigma_{xy} = \frac{e^2}{h} \nu, \tag{8.16}$$

where ν is an integer. This is an example of the so-called integer quantum Hall effect. One can similarly generate a heat current by applying a temperature gradient $\boldsymbol{\nabla} T$ across the same system. The heat current density $\boldsymbol{j}_Q$ is then related by the linear-response

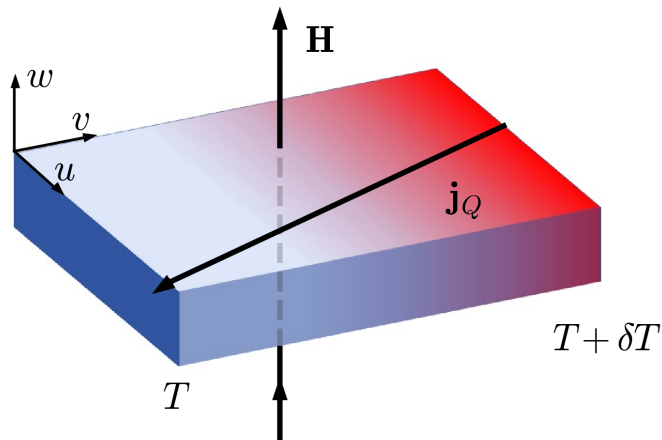$$\boldsymbol{j}_Q = -\kappa \boldsymbol{\nabla} T, \tag{8.17}$$

Figure 8.2: Schematic depicting the thermal Hall effect. In the presence of a magnetic field, a temperature gradient produces a heat current with both a longitudinal component along the u-axis, and a transverse component along the v-axis, in the plane perpendicular to the magnetic field.

where κ is a matrix known as the thermal conductivity tensor. In the example of a two-dimensional electron gas, the thermal gradient generates a heat current with components that are perpendicular to $\boldsymbol{\nabla}T$. In analogy to the purely electrical effect, this is known as the thermal Hall effect. In this case, the thermal Hall conductivity given by the Wiedemann–Franz law

$$\kappa_{xy} = T\frac{\pi^2 k_{\mathrm{B}}^2}{3e^2}\sigma_{xy} = T\frac{\pi^2 k_{\mathrm{B}}^2}{3h}\nu, \tag{8.18}$$

at any finite temperature T. A schematic depicting the thermal Hall effect is shown in Fig. 8.2.

As described in Sec. 8.1, magnons are quasiparticles corresponding to fluctuations in the spin ordering. As such, magnons are electrically neutral and do not carry an electrical current. Magnons do carry energy however, and can thus produce a heat current in the presence of a thermal gradient. The thermal Hall effect of magnons, which is henceforth referred to as the magnon Hall effect, was first predicted theoretically by Katsura *et al.* [86], who calculated and expression for the thermal Hall conductivity of magnons explicitly using the Kubo formula. In particular, the authors showed that the magnon Hall effect arises from the Berry curvature associated with the magnon wavefunctions, which can become

non-zero in the presence of DM interactions. Matsumoto and Murakami subsequently found that there should be a correction term to the thermal Hall conductivity, owing to the orbital motion of magnons [71, 72]. It was found that the thermal Hall conductivity of magnons for a model with M energy bands is given by

$$\kappa_{\mu\nu} = \frac{-k_{\mathrm{B}}^2 T}{\hbar V} \sum_{\boldsymbol{k}} \sum_{n=1}^{M} c_2\left(\rho(E_{n\boldsymbol{k}})\right) F_{\mu\nu}^{(n)}(\boldsymbol{k}), \qquad (8.19)$$

where V is the sample volume and $F_{\mu\nu}^{(n)}(\boldsymbol{k})$ is the Berry curvature of the nth magnon band, as defined in Eq. (2.12). Here, $E_{n\boldsymbol{k}}$ is the dispersion of the nth energy band, $\rho(E) = 1/\left(e^{E/k_{\mathrm{B}}T} - 1\right)$ is the Bose distribution function and

$$c_2(\rho) \equiv \int_0^\rho \mathrm{d}t \ln^2\left(\frac{1+t}{t}\right) \qquad (8.20)$$

is a function that increases monotonically from $c_2 = 0$ for $\rho = 0$ and $c_2 \to \pi^2/3$ as $\rho \to \infty$. The function $c_2(\rho)$ effectively re-weights the Bose distribution function.

In the case of $\mathrm{Lu_2V_2O_7}$, we may estimate the Berry curvature in the vicinity of the Γ point by treating the DM interaction as a perturbation, similar to the calculation in Ref. [87]. We take the magnon Hamiltonian defined in Eq. (8.14), and decompose it as $\mathcal{M}(\boldsymbol{k}) = \mathcal{M}_0 + \mathcal{M}'(\boldsymbol{k})$, where

$$\mathcal{M}_0 \equiv \mathcal{M}(\boldsymbol{0})\bigg|_{\boldsymbol{D}_{ij}=0} \qquad (8.21)$$

is the magnon Hamiltonian evaluated at the Γ point in the absence of DM interactions, and $\mathcal{M}'(\boldsymbol{k}) \equiv \mathcal{M}(\boldsymbol{k}) - \mathcal{M}_0$. From the low-energy dispersion calculated in Eq. (8.15), we see that the eigenvector of the lowest band at $\boldsymbol{k} = 0$ is given by

$$\left|E_-^{(0)}(\boldsymbol{0})\right\rangle = \frac{1}{2}\begin{pmatrix} 1 \\ 1 \\ 1 \\ 1 \end{pmatrix}, \qquad (8.22)$$

corresponding to the lowest magnon excitation energy $E_-^{(0)}(\boldsymbol{0}) = \mu_{\mathrm{B}}gH$. The eigenstates in the vicinity of $\boldsymbol{k} = 0$ can then be estimated to first order in perturbation theory as

$$\left|E_-^{(1)}(\boldsymbol{k})\right\rangle = \left(1 + \left(E_-^{(0)}(\boldsymbol{0}) - \mathcal{M}_0\right)^{-1}\left(1 - \left|E_-^{(0)}(\boldsymbol{0})\right\rangle\left\langle E_-^{(0)}(\boldsymbol{0})\right|\right)\mathcal{M}'(\boldsymbol{k})\right)\left|E_-^{(0)}(\boldsymbol{0})\right\rangle. \qquad (8.23)$$

Next, the Berry connection may be estimated as

$$A_\mu(\boldsymbol{k}) = -i \left\langle E_-^{(1)}(\boldsymbol{k}) \left| \frac{\partial}{\partial k^\mu} \right| E_-^{(1)}(\boldsymbol{k}) \right\rangle, \tag{8.24}$$

and the Berry curvature can subsequently be computed using Eq. (2.12). This calculation is quite complicated, so it was carried out using symbolic computations in Mathematica. The resulting expression for the Berry curvature in the vicinity of $\boldsymbol{k} = 0$ is

$$F_{\mu\nu}(\boldsymbol{k}) = -\frac{D}{8\sqrt{2}J} \epsilon_{\mu\nu\lambda} w_\lambda \left(|\boldsymbol{k}|^2 + k_\lambda^2 \right), \tag{8.25}$$

to first order in perturbation theory, where w_λ are the components of the unit vector $\hat{\boldsymbol{w}}$ pointing in the direction of spin ordering (i.e. the direction of the external magnetic field). The thermal Hall conductivity of magnons can then be computed using Eq. (8.19) in the thermodynamic limit, as

$$\begin{aligned} \kappa_{\mu\nu} &= \frac{-4k_B^2 T}{\hbar a} \int \frac{\mathrm{d}^3 k}{(2\pi)^3} c_2 \left(\rho(E_-^{(0)}(\boldsymbol{k})) \right) F_{\mu\nu}(\boldsymbol{k}) \\ &= \frac{k_B^2 T}{\hbar a} \frac{D}{2\sqrt{2}J} \epsilon_{\mu\nu\lambda} w_\lambda \int \frac{\mathrm{d}^3 k}{(2\pi)^3} c_2 \left(\rho(E_-^{(0)}(\boldsymbol{k})) \right) \left(|\boldsymbol{k}|^2 + k_\lambda^2 \right). \end{aligned} \tag{8.26}$$

It is clear that this expression only has non-zero components in the plane perpendicular to the spin ordering direction $\hat{\boldsymbol{w}}$, so we evaluate this integral in terms of the (u, v, w) coordinates defined in Sec. 8.1. The thermal Hall conductivity then becomes

$$\begin{aligned} \kappa_{uv} &= \frac{k_B^2 T}{\hbar a} \frac{D}{16\pi^3 \sqrt{2}J} \int \mathrm{d}^3 k \, c_2 \left(\rho(E_-^{(0)}(\boldsymbol{k})) \right) \left(|\boldsymbol{k}|^2 + k_w^2 \right) \\ &= \frac{k_B^2 T}{\hbar a} \frac{D}{16\pi^3 \sqrt{2}J} \int_0^\infty \mathrm{d}|\boldsymbol{k}| \int_0^\pi \mathrm{d}\theta \int_0^{2\pi} \mathrm{d}\varphi \, c_2 \left(\rho(E_-^{(0)}(|\boldsymbol{k}|)) \right) |\boldsymbol{k}|^4 \sin\theta \left(1 + \cos^2\theta \right), \end{aligned} \tag{8.27}$$

where the last line is obtained by transforming to spherical coordinates relative to the (u, v, w) coordinate system, as the magnons disperse isotropically. The integral over θ is evaluated to

$$\int_0^\pi \mathrm{d}\theta \sin\theta \left(1 + \cos^2\theta \right) = \frac{8}{3}, \tag{8.28}$$

which simplifies the Hall conductivity to

$$\kappa_{uv} = \frac{D}{J} \frac{k_B^2 T}{3\sqrt{2}\pi^2 \hbar a} \int_0^\infty \mathrm{d}k \, k^4 c_2 \left(\rho(E_-^{(0)}(k)) \right), \tag{8.29}$$

where

$$\rho(E_-^{(0)}(k)) = \frac{1}{\exp\left(\frac{\mu_{\mathrm{B}} g H + J a^2 k^2/16}{k_{\mathrm{B}} T}\right) - 1}.$$ (8.30)

The integral in Eq. (8.29) must then be evaluated numerically for a given temperature. This result indicates that the magnitude of the DM interaction D/J can be calculated directly from thermal Hall conductivity measurements. Such an an experiment is discussed in Sec. 8.3.

8.3   Experimental evidence

The magnon Hall effect was first observed in a single crystal of $\mathrm{Lu_2V_2O_7}$ by Onose *et al.* using thermal transport measurements [67]. The magnetic field dependence of these thermal Hall conductivity measurements at various temperatures is shown in Fig. 8.3. Longitudinal electrical conductivity measurements were also taken, from which the electronic contribution to the thermal conductivity can be inferred using the the Wiedemann-Franz law (Eq. (8.18)). It was determined that the electronic contribution to the thermal conductivity is less than 10^{-5} W/(K·m) at temperatures below 100 K, suggesting that the heat current is carried by either phonons or magnons below the ordering temperature.

We see that the Hall conductivity vanishes at high temperature, consistent with the critical ordering temperature of $T_c = 73$ K, as well as at low temperature, where we expect that magnon states are no longer populated.

Magnetization measurements for magnetic fields aligned along the [100], [110], and [111] directions were taken and showed nearly isotropic magnetization curves that saturate to a maximum of $1\mu_{\mathrm{B}}$ for magnetic fields larger than approximately 0.2 T. These measurements are consistent with the sharp increase in thermal conductivity at low field seen in Fig. 8.3, due to the increase in magnons from the spins becoming ordered, followed by a gradual decrease due to the magnon gap, which decreases the population of magnons. A phonon origin for the thermal Hall effect is ruled out, as the thermal Hall conductivity is expected to increase monotonically with magnetic field for phonons, due to reduced scattering with magnetic fluctuations [88].
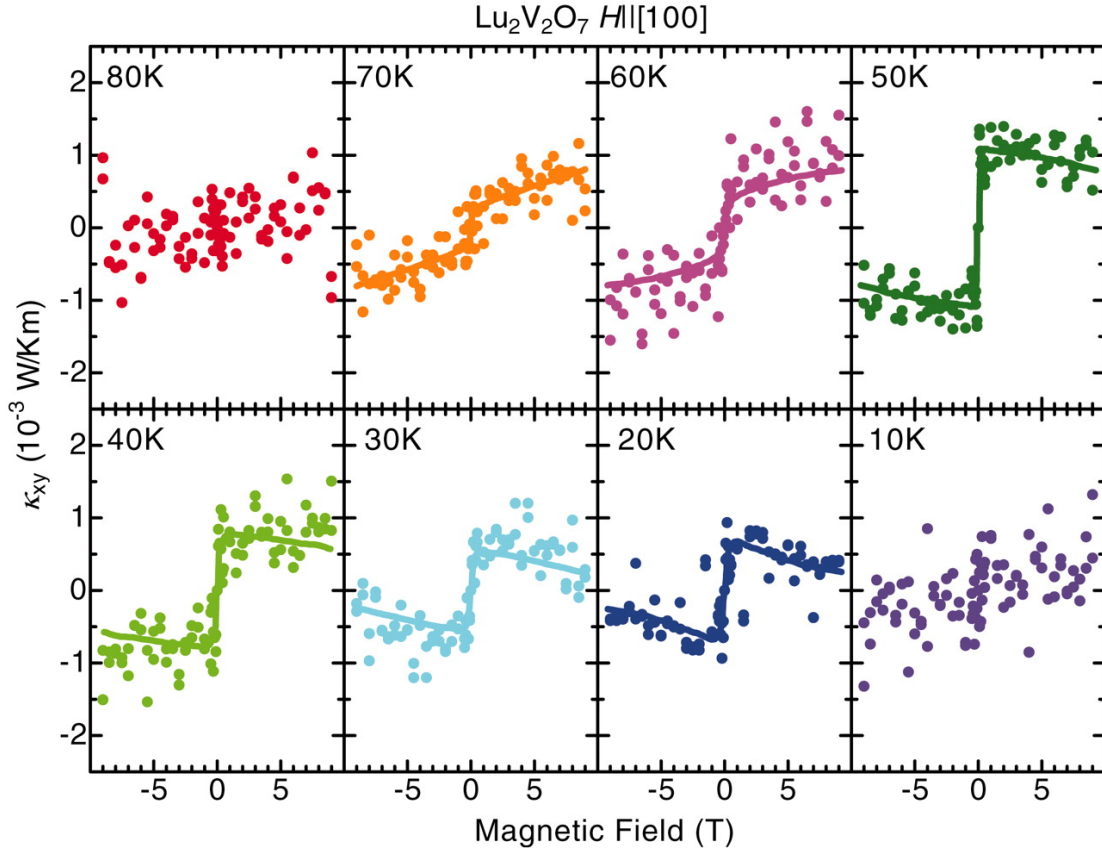
Figure 8.3: Magnetic field dependence of the thermal Hall conductivity in $Lu_2V_2O_7$ at various temperatures. The Hall conductivity was measured in the plane perpendicular to the applied magnetic field. Figure reprinted from Ref. [67] with permission granted by the American Association for the Advancement of Science (AAAS) guidelines.

8.4 Calculation of the DM interaction

In the original paper by Onose *et al.* [67], the authors fit the thermal Hall conductivity measurements depicted in Fig. 8.3 to extract the magnitude of the DM interaction $D/J = 0.32$. By fitting the magnon spectrum to inelastic neutron scattering measurements, a magnitude of the DM interaction $D/J = 0.18$ was found in Ref. [70], at odds with the value reported by Onose *et al.* [67]. The thermal Hall conductivity fit by Onose *et al.* [67] was carried out using the magnon Hall conductivity derived by Katsura *et al.* in Ref. [66],

determined to be

$$\kappa_{uv}^E = -\frac{D}{J}\frac{k_{\mathrm{B}}^2 T}{8\sqrt{2}\pi^{3/2}J\hbar a}\left(2 + \frac{g\mu_{\mathrm{B}}H}{J}\right)^2\sqrt{\frac{k_{\mathrm{B}}T}{J}}\mathrm{Li}_{\frac{5}{2}}\left(\exp\left(-\frac{g\mu_{\mathrm{B}}H}{k_{\mathrm{B}}T}\right)\right), \qquad (8.31)$$

where $\mathrm{Li}_s(z) = \sum_{p=1}^{\infty}\frac{z^p}{p^s}$ is the polylogarithm function. The thermal Hall conductivity in Eq. (8.31) results from the magnon edge current at the sample boundary, however, it was later determined that there should be an extra contribution to the Hall conductivity arising from the orbital motion of magnons [71, 72], which has not been accounted for when determining the DM interaction. A re-investigation of the thermal Hall conductivity data for $Lu_2V_2O_7$ is presented here, taking into account this correction, to calculate the magnitude of the DM interaction D/J.

The contribution to the thermal Hall conductivity from the orbital motion of magnons κ_{uv}^O can be calculated from Eq. (8.31) and Eq. (8.29) as

$$\kappa_{uv}^O = \kappa_{uv} - \kappa_{uv}^E. \qquad (8.32)$$

The components of the thermal Hall conductivity using $J = 8.2$ meV and $D/J = 0.18$, determined from inelastic neutron scattering in Ref. [70], are plotted in Fig. 8.4(a) at $T = 20$ K. The orbital contribution κ_{uv}^O corresponds to the correction to the thermal Hall conductivity that was not accounted for in the analysis by Onose *et al.* [67]. This correction is seen to lower the overall Hall conductivity, a result consistent with Ref. [71]. The total corrected Hall conductivity is plotted in Fig. 8.4(b), along with the conductivity measurements from Onose *et al.* [67]. We see that these conductivity measurements are inconsistent with the parameters determined by inelastic neutron scattering. The conductivity measurements are therefore re-fit using the corrected Hall conductivity formula in Eq.(8.29).

The thermal Hall conductivity was fit using the magnetic field dependent data from Ref. [67] at the fixed temperature $T = 20$ K, using a minimum chi-square estimation. The temperature chosen is justified by the fact that in Ref. [87], the mean-free path of both phonons and magnons was estimated using the longitudinal thermal conductivity data to be $\ell \approx 35$ Å at 20 K, which is an order of magnitude larger than the distance between neighbouring V^{4+} atoms ≈ 3.5 Å. As temperature increases, the mean-free path of these quasiparticles decreases, and the corresponding Bloch waves are no longer well defined.

In the original work by Onose *et al.* [67], magnetic specific heat data was fit to estimate a value of the ferromagnetic Heisenberg exchange $J = 3.4$ meV in Eq. (7.4). More recently however, inelastic neutron scattering measurements [70] and DFT calculations [69] have resulted in an estimated exchange coupling of $J = 8.2$ meV. Both values are used to fit the thermal transport data independently. In the case where $J = 3.4$ meV, we find a magnitude

$D/J = 0.42$ for the DM interaction, in contrast to the magnitude $D/J = 0.32$ calculated by Onose *et al.* [67]. In the case where $J = 8.2$ meV, it is found that $D/J = 2.51$. The result of this fit is shown in Fig. 8.5.

This result exacerbates an apparent discrepancy regarding the value of the DM interaction in $Lu_2V_2O_7$. On one hand, the DM interaction is expected to be small, as V^{4+} is a transition metal ion where spin-orbit coupling is weak. This expectation is consistent with various DFT calculations, where values of $D/J = 0.05$ [68] and $D/J = 0.07$ [69] were found, and arguably with inelastic neutron scattering measurements, which found $D/J = 0.18$ [70]. On the other hand, this seems to be inconsistent with the thermal Hall conductivity measurements from Ref. [67], where the existence of the DM interaction in $Lu_2V_2O_7$ was inferred in the first place. This inconsistency leaves an open question as to the elusive nature of spin-orbit coupling in this material, that requires further attention.
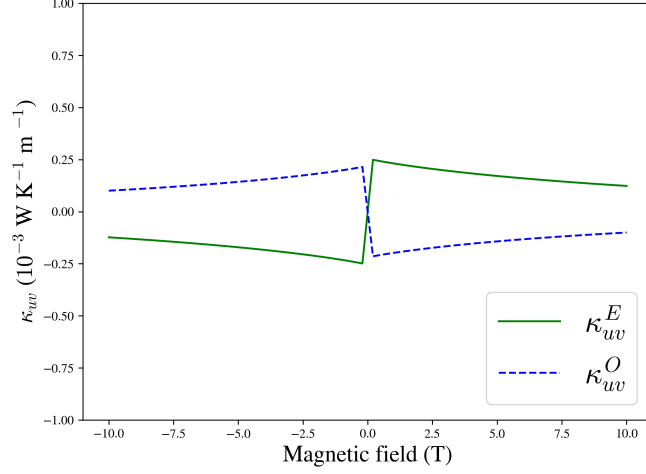
(a)
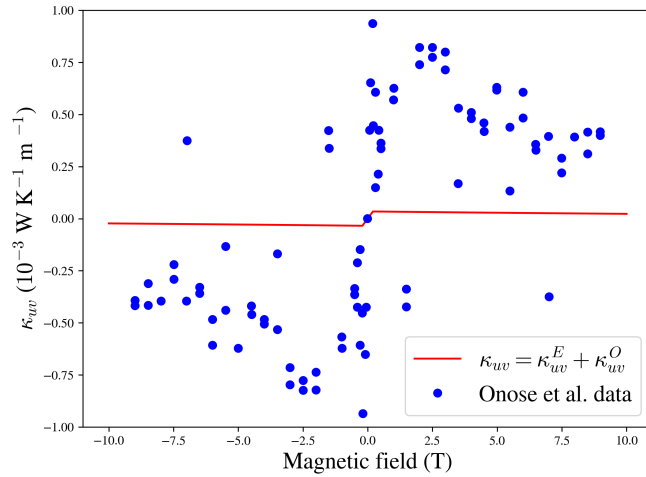
(b)

Figure 8.4: Thermal Hall conductivity of magnons in $Lu_2V_2O_7$ as a function of magnetic field at $T = 20$ K. Plotted for $J = 8.2$ meV and $D/J = 0.18$, corresponding to the values from Ref. [70] determined by inelastic neutron scattering measurements. (a) The contributions to the Hall conductivity due to the magnon edge current κ_{uv}^E and the orbital motion of magnons κ_{uv}^O (see Eq. (8.29) and Eqs. (8.31-8.32)). (b) The calculated thermal Hall conductivity κ_{uv} from Eq. (8.29), superimposed on the Hall conductivity measurements by Onose et al. [67]
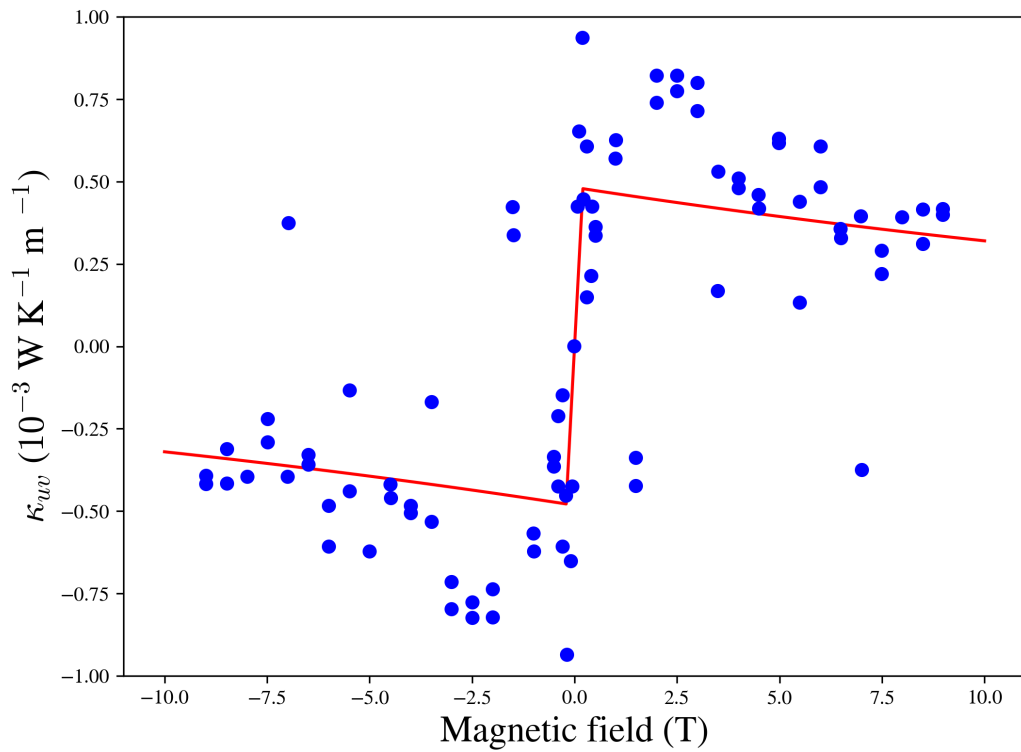
Figure 8.5: Fit of the thermal Hall conductivity data for $Lu_2V_2O_7$ as a function of magnetic field at $T = 20$ K. The data points from Ref. [67] are depicted in blue, while the fit using Eq. (8.29) is shown in red.

Chapter 9

Conclusion

In Part II of this thesis, a re-investigation of the thermal transport data from for $Lu_2V_2O_7$ was carried out, using a corrected theory of the magnon Hall effect described in Sec. 8.2. For the case of an exchange interaction $J = 3.4$ meV, determined from thermal conductivity measurements in Ref. [67], we find a magnitude $D/J = 0.42$ for the DM interaction. In the case where $J = 8.2$ meV, determined from DFT calculations [69] and inelastic neutron scattering [70], it is found that $D/J = 2.51$. These result highlight a discrepancy regarding the value of the DM interaction in $Lu_2V_2O_7$, where values in the range $D/J = 0.05 - 0.18$ were found using DFT and neutron scattering data. Given that V^{4+} is a transition metal ion where spin-orbit coupling is weak, it is expected that the thermal transport data is overestimated the DM interaction.

This discrepancy motivates several avenues of future work needed to better understand the microscopic description of $Lu_2V_2O_7$. For one, the approximations made in Sec. 8.2 do not take into account magnon self-interactions, that may influence the thermal Hall conductivity. It would also be worthwhile to investigate whether magnon-phonon interactions are consistent with the thermal conductivity data, as such an interaction has recently been shown to contribute to the thermal Hall conductivity in quantum ferromagnets [89].

This also leaves open the possibility of additional interactions in the low-energy spin model of $Lu_2V_2O_7$ that were not accounted for in the Hall conductivity calculations. It was also shown in Ref. [90] that dipolar interactions contribute to the Berry curvature of magnons, and can lead to a magnon Hall effect. A single-ion anisotropy term considered in Ref. [68] may be ruled out, as this is a spin-1/2 system, and the square of any Pauli operator is proportional to the identity operator. The DFT calculations in Ref. [69] have also suggested that there may be a small off-diagonal symmetric exchange in the low-energy

spin model, however, this is not expected to contribute much to the transport coefficients as the energy scale of this interaction was found to be about 50 times smaller than the Heisenberg exchange, and thus will not contribute significantly to the Berry curvature of magnons.

Finally, the discrepancy in the DM interaction described in Sec. 8.4 motivates further thermal Hall conductivity measurements in $Lu_2V_2O_7$. In particular, further measurements at various temperatures in the range of $20 - 30$ K may result in a DM interaction that is more consistent with the inelastic neutron scattering data [70].

References

[1] L. Landau and E. Lifshitz, *Statistical Physics: Volume 5* (Elsevier Science, 2013).

[2] J. E. Moore, "The birth of topological insulators," Nature **464**, 194–198 (2010).

[3] M. Z. Hasan and J. E. Moore, "Three-Dimensional Topological Insulators," Annu. Rev. Condens. Matter Phys. **2**, 55–78 (2011).

[4] S.-Q. Shen, "The family of topological phases in condensed matter," Natl. Sci. Rev. **1**, 49–59 (2014).

[5] X. Wen, *Quantum Field Theory of Many-Body Systems: From the Origin of Sound to an Origin of Light and Electrons* (Oxford University Press, 2004).

[6] B. A. Bernevig and T. L. Hughes, *Topological Insulators and Topological Superconductors* (Princeton University Press, 2013).

[7] A. A. Burkov, "Topological semimetals," Nat. Mater. **15**, 1145–1148 (2016).

[8] C. Wang, L. Gioia, and A. A. Burkov, "Fractional Quantum Hall Effect in Weyl Semimetals," Phys. Rev. Lett. **124**, 096603 (2020).

[9] A. A. Burkov, M. D. Hook, and L. Balents, "Topological nodal semimetals," Phys. Rev. B **84**, 235126 (2011).

[10] S. T. Ramamurthy and T. L. Hughes, "Quasitopological electromagnetic response of line-node semimetals," Phys. Rev. B **95**, 075138 (2017).

[11] J. J. Sakurai and J. Napolitano, *Modern Quantum Mechanics*, 3rd ed. (Cambridge University Press, 2020).

[12] M. Born and V. Fock, "Beweis des Adiabatensatzes," Zeitschrift für Phys. **51**, 165–180 (1928).

[13] D. R. Hofstadter, "Energy levels and wave functions of bloch electrons in rational and irrational magnetic fields," Phys. Rev. B **14**, 2239–2249 (1976).

[14] M. V. Berry, "Quantal phase factors accompanying adiabatic changes," Proc. R. Soc. London. A. Math. Phys. Sci. **392**, 45–57 (1984).

[15] Y. Aharonov and D. Bohm, "Significance of Electromagnetic Potentials in the Quantum Theory," Phys. Rev. **115**, 485–491 (1959).

[16] C. Kane, "Chapter 1 - topological band theory and the $\mathbb{Z}_2$ invariant," in *Topological Insulators*, Contemporary Concepts of Condensed Matter Science, Vol. 6, edited by M. Franz and L. Molenkamp (Elsevier, 2013) pp. 3–34.

[17] F. D. M. Haldane, "Model for a Quantum Hall Effect without Landau Levels: Condensed-Matter Realization of the "Parity Anomaly"," Phys. Rev. Lett. **61**, 2015–2018 (1988).

[18] C. L. Kane and E. J. Mele, "Quantum Spin Hall Effect in Graphene," Phys. Rev. Lett. **95**, 226801 (2005).

[19] C. L. Kane and E. J. Mele, "$\mathbb{Z}_2$ Topological Order and the Quantum Spin Hall Effect," Phys. Rev. Lett. **95**, 146802 (2005).

[20] J. E. Moore and L. Balents, "Topological invariants of time-reversal-invariant band structures," Phys. Rev. B **75**, 121306 (2007).

[21] S. Murakami, "Phase transition between the quantum spin Hall and insulator phases in 3D: emergence of a topological gapless phase," New J. Phys. **9**, 356–356 (2007).

[22] L. Fu, C. L. Kane, and E. J. Mele, "Topological Insulators in Three Dimensions," Phys. Rev. Lett. **98**, 106803 (2007).

[23] Y. Xia, D. Qian, D. Hsieh, L. Wray, A. Pal, H. Lin, A. Bansil, D. Grauer, Y. S. Hor, R. J. Cava, and M. Z. Hasan, "Observation of a large-gap topological-insulator class with a single Dirac cone on the surface," Nat. Phys. **5**, 398–402 (2009).

[24] L. Isaev, Y. H. Moon, and G. Ortiz, "Bulk-boundary correspondence in three-dimensional topological insulators," Phys. Rev. B **84**, 075444 (2011).

[25] N. P. Armitage, E. J. Mele, and A. Vishwanath, "Weyl and Dirac semimetals in three-dimensional solids," Rev. Mod. Phys. **90**, 015001 (2018).

[26] P. A. M. Dirac, *The Principles of Quantum Mechanics*, 4th ed. (Clarendon Press, 1981).

[27] B. Béri, "Topologically stable gapless phases of time-reversal-invariant superconductors," Phys. Rev. B **81**, 134515 (2010).

[28] A. A. Burkov and L. Balents, "Weyl Semimetal in a Topological Insulator Multilayer," Phys. Rev. Lett. **107**, 127205 (2011).

[29] A. A. Burkov, "Quantum anomalies in nodal line semimetals," Phys. Rev. B **97**, 165104 (2018).

[30] J.-M. Carter, V. V. Shankar, M. A. Zeb, and H.-Y. Kee, "Semimetal and Topological Insulator in Perovskite Iridates," Phys. Rev. B **85**, 115105 (2012).

[31] C. Fang, Y. Chen, H.-Y. Kee, and L. Fu, "Topological nodal line semimetals with and without spin-orbital coupling," Phys. Rev. B **92**, 081201 (2015).

[32] Q.-F. Liang, J. Zhou, R. Yu, Z. Wang, and H. Weng, "Node-surface and node-line fermions from nonsymmorphic lattice symmetries," Phys. Rev. B **93**, 085427 (2016).

[33] Y. Chen, Y. Xie, S. A. Yang, H. Pan, F. Zhang, M. L. Cohen, and S. Zhang, "Nanostructured Carbon Allotropes with Weyl-like Loops and Points," Nano Lett. **15**, 6974–6978 (2015).

[34] H. Weng, Y. Liang, Q. Xu, R. Yu, Z. Fang, X. Dai, and Y. Kawazoe, "Topological node-line semimetal in three-dimensional graphene networks," Phys. Rev. B **92**, 045108 (2015).

[35] Y. Kim, B. J. Wieder, C. L. Kane, and A. M. Rappe, "Dirac Line Nodes in Inversion-Symmetric Crystals," Phys. Rev. Lett. **115**, 036806 (2015).

[36] Y.-H. Chan, C.-K. Chiu, M. Y. Chou, and A. P. Schnyder, "Ca_3P_2 and other topological semimetals with line nodes and drumhead surface states," Phys. Rev. B **93**, 205132 (2016).

[37] D. J. Thouless, M. Kohmoto, M. P. Nightingale, and M. den Nijs, "Quantized Hall Conductance in a Two-Dimensional Periodic Potential," Phys. Rev. Lett. **49**, 405–408 (1982).

[38] C.-K. Chiu and A. P. Schnyder, "Classification of reflection-symmetry-protected topological semimetals and nodal superconductors," Phys. Rev. B **90**, 205136 (2014).

[39] S. T. Ramamurthy and T. L. Hughes, "Patterns of electromagnetic response in topological semimetals," Phys. Rev. B **92**, 085105 (2015).

[40] A. A. Zyuzin and A. A. Burkov, "Topological response in Weyl semimetals and the chiral anomaly," Phys. Rev. B **86**, 115133 (2012).

[41] J. D. Jackson, *Classical electrodynamics*, 3rd ed. (Wiley, New York, NY, 1999).

[42] S. Ryu and Y. Hatsugai, "Topological Origin of Zero-Energy Edge States in Particle-Hole Symmetric Systems," Phys. Rev. Lett. **89**, 077002 (2002).

[43] M. M. Hosen, G. Dhakal, B. Wang, N. Poudel, K. Dimitri, F. Kabir, C. Sims, S. Regmi, K. Gofryk, D. Kaczorowski, A. Bansil, and M. Neupane, "Experimental observation of drumhead surface states in SrAs$_3$," Sci. Rep. **10**, 2776 (2020).

[44] R. Jackiw and C. Rebbi, "Solitons with fermion number $\frac{1}{2}$," Phys. Rev. D **13**, 3398–3409 (1976).

[45] L. M. Schoop, M. N. Ali, C. Straßer, A. Topp, A. Varykhalov, D. Marchenko, V. Duppel, S. S. P. Parkin, B. V. Lotsch, and C. R. Ast, "Dirac cone protected by non-symmorphic symmetry and three-dimensional Dirac line node in ZrSiS," Nat. Commun. **7**, 11696 (2016).

[46] R. Lou, J.-Z. Ma, Q.-N. Xu, B.-B. Fu, L.-Y. Kong, Y.-G. Shi, P. Richard, H.-M. Weng, Z. Fang, S.-S. Sun, Q. Wang, H.-C. Lei, T. Qian, H. Ding, and S.-C. Wang, "Emergence of topological bands on the surface of ZrSnTe crystal," Phys. Rev. B **93**, 241104 (2016).

[47] D. Takane, K. Nakayama, S. Souma, T. Wada, Y. Okamoto, K. Takenaka, Y. Yamakawa, A. Yamakage, T. Mitsuhashi, K. Horiba, H. Kumigashira, T. Takahashi, and T. Sato, "Observation of Dirac-like energy band and ring-torus Fermi surface associated with the nodal line in topological insulator CaAgAs," npj Quantum Mater. **3**, 1 (2018).

[48] J. Nayak, N. Kumar, S.-C. Wu, C. Shekhar, J. Fink, E. D. L. Rienks, G. H. Fecher, Y. Sun, and C. Felser, "Electronic properties of topological insulator candidate CaAgAs," J. Phys. Condens. Matter **30**, 045501 (2018).

[49] D. Takane, Z. Wang, S. Souma, K. Nakayama, C. X. Trang, T. Sato, T. Takahashi, and Y. Ando, "Dirac-node arc in the topological line-node semimetal HfSiS," Phys. Rev. B **94**, 121108 (2016).

[50] G. Bian, T.-R. Chang, H. Zheng, S. Velury, S.-Y. Xu, T. Neupert, C.-K. Chiu, S.-M. Huang, D. S. Sanchez, I. Belopolski, N. Alidoust, P.-J. Chen, G. Chang, A. Bansil, H.-T. Jeng, H. Lin, and M. Z. Hasan, "Drumhead surface states and topological nodal-line fermions in TlTaSe$_2$," Phys. Rev. B **93**, 121113 (2016).

[51] G. Bian, T.-R. Chang, R. Sankar, S.-Y. Xu, H. Zheng, T. Neupert, C.-K. Chiu, S.-M. Huang, G. Chang, I. Belopolski, D. S. Sanchez, M. Neupane, N. Alidoust, C. Liu, B. Wang, C.-C. Lee, H.-T. Jeng, C. Zhang, Z. Yuan, S. Jia, A. Bansil, F. Chou, H. Lin, and M. Z. Hasan, "Topological nodal-line fermions in spin-orbit metal PbTaSe$_2$," Nat. Commun. **7**, 10556 (2016).

[52] S.-Y. Guan, P.-J. Chen, and T.-M. Chuang, "Topological surface states and superconductivity in non-centrosymmetric PbTaSe$_2$," Jpn. J. Appl. Phys. **60**, SE0803 (2021).

[53] J. Bardeen, L. N. Cooper, and J. R. Schrieffer, "Microscopic Theory of Superconductivity," Phys. Rev. **106**, 162–164 (1957).

[54] P. W. Anderson, *Basic Notions Of Condensed Matter Physics* (CRC Press, 2018) p. 564.

[55] C. Kallin and J. Berlinsky, "Chiral superconductors," Reports Prog. Phys. **79**, 054502 (2016).

[56] N. Read and D. Green, "Paired states of fermions in two dimensions with breaking of parity and time-reversal symmetries and the fractional quantum Hall effect," Phys. Rev. B **61**, 10267–10297 (2000).

[57] V. Gurarie and L. Radzihovsky, "Zero modes of two-dimensional chiral p-wave superconductors," Phys. Rev. B **75**, 212509 (2007).

[58] A. Abrikosov, "The magnetic properties of superconducting alloys," J. Phys. Chem. Solids **2**, 199–208 (1957).

[59] G. E. Volovik, "Fermion zero modes on vortices in chiral superconductors," J. Exp. Theor. Phys. Lett. **70**, 609–614 (1999).

[60] G. Möller, N. R. Cooper, and V. Gurarie, "Structure and consequences of vortex-core states in p-wave superfluids," Phys. Rev. B **83**, 014513 (2011).

[61] D. A. Ivanov, "Non-Abelian Statistics of Half-Quantum Vortices in p-Wave Superconductors," Phys. Rev. Lett. **86**, 268–271 (2001).

[62] J. G. Rau and M. J. Gingras, "Frustrated Quantum Rare-Earth Pyrochlores," Annu. Rev. Condens. Matter Phys. **10**, 357–386 (2019).

[63] I. Dzyaloshinsky, "A thermodynamic theory of "weak" ferromagnetism of antiferromagnetics," J. Phys. Chem. Solids **4**, 241–255 (1958).

[64] T. Moriya, "Anisotropic Superexchange Interaction and Weak Ferromagnetism," Phys. Rev. **120**, 91–98 (1960).

[65] I. F. Sharafullin, M. K. Kharrasov, and H. T. Diep, "Dzyaloshinskii-Moriya interaction in magnetoferroelectric superlattices: Spin waves and skyrmions," Phys. Rev. B **99**, 214420 (2019).

[66] H. Katsura, N. Nagaosa, and P. A. Lee, "Theory of the Thermal Hall Effect in Quantum Magnets," Phys. Rev. Lett. **104**, 066403 (2010).

[67] Y. Onose, T. Ideue, H. Katsura, Y. Shiomi, N. Nagaosa, and Y. Tokura, "Observation of the Magnon Hall Effect," Science **329**, 297—-299 (2010).

[68] H. J. Xiang, E. J. Kan, M.-H. Whangbo, C. Lee, S.-H. Wei, and X. G. Gong, "Single-ion anisotropy, Dzyaloshinskii-Moriya interaction, and negative magnetoresistance of the spin-$\frac{1}{2}$ pyrochlore R_2V_2O7," Phys. Rev. B **83**, 174402 (2011).

[69] K. Riedl, D. Guterding, H. O. Jeschke, M. J. P. Gingras, and R. Valentí, "*Ab initio* determination of spin Hamiltonians with anisotropic exchange interactions: The case of the pyrochlore ferromagnet $Lu_2V_2O_7$," Phys. Rev. B **94**, 014410 (2016).

[70] M. Mena, R. S. Perry, T. G. Perring, M. D. Le, S. Guerrero, M. Storni, D. T. Adroja, C. Rüegg, and D. F. McMorrow, "Spin-Wave Spectrum of the Quantum Ferromagnet on the Pyrochlore Lattice $Lu_2V_2O_7$," Phys. Rev. Lett. **113**, 047202 (2014).

[71] R. Matsumoto and S. Murakami, "Rotational motion of magnons and the thermal Hall effect," Phys. Rev. B **84**, 184406 (2011).

[72] R. Matsumoto and S. Murakami, "Theoretical Prediction of a Rotating Magnon Wave Packet in Ferromagnets," Phys. Rev. Lett. **106**, 197202 (2011).

[73] S. T. Bramwell and M. J. P. Gingras, "Spin Ice State in Frustrated Magnetic Pyrochlore Materials," Science **294**, 1495–1501 (2001).

[74] J. S. Gardner, M. J. P. Gingras, and J. E. Greedan, "Magnetic pyrochlore oxides," Rev. Mod. Phys. **82**, 53–107 (2010).

[75] M. J. P. Gingras, "Observing Monopoles in a Magnetic Analog of Ice," Science **326**, 375–376 (2009).

[76] A. Haghighirad, C. Gross, and W. Assmus, "Powder synthesis and crystal growth of $Y_2V_2O_7$ under high pressure and its physical properties," J. Cryst. Growth **310**, 2277–2283 (2008).

[77] H. Ichikawa, L. Kano, M. Saitoh, S. Miyahara, N. Furukawa, J. Akimitsu, T. Yokoo, T. Matsumura, M. Takeda, and K. Hirota, "Orbital Ordering in Ferromagnetic $Lu_2V_2O_7$," J. Phys. Soc. Japan **74**, 1020–1025 (2005).

[78] S. Miyahara, A. Murakami, and N. Furukawa, "Orbital ordering induced ferromagnetism in $Lu_2V_2O_7$," J. Mol. Struct. **838**, 223–226 (2007).

[79] P. Fazekas, *Lecture Notes On Electron Correlation And Magnetism* (World Scientific Publishing Company, 1999) p. 796.

[80] L. Soderholm and J. Greedan, "Relationship between crystal structure and magnetic properties of $(RE)_2V_2O_7$; RE=Lu, Yb, Tm," Mater. Res. Bull. **17**, 707–713 (1982).

[81] S.-i. Shamoto, T. Nakano, Y. Nozue, and T. Kajitani, "Substitution effects on ferromagnetic Mott insulator $Lu_2V_2O_7$," J. Phys. Chem. Solids **63**, 1047–1050 (2002).

[82] M. Elhajal, B. Canals, R. Sunyer, and C. Lacroix, "Ordering in the pyrochlore antiferromagnet due to Dzyaloshinsky-Moriya interactions," Phys. Rev. B **71**, 094420 (2005).

[83] N. Arakawa, "Microscopic theory of Dzyaloshinsky-Moriya interaction in pyrochlore oxides with spin-orbit coupling," Phys. Rev. B **94**, 155139 (2016).

[84] T. Holstein and H. Primakoff, "Field Dependence of the Intrinsic Domain Magnetization of a Ferromagnet," Phys. Rev. **58**, 1098–1113 (1940).

[85] T. Ideue, Y. Onose, H. Katsura, Y. Shiomi, S. Ishiwata, N. Nagaosa, and Y. Tokura, "Effect of lattice geometry on magnon Hall effect in ferromagnetic insulators," Phys. Rev. B **85**, 134411 (2012).

[86] H. Katsura, N. Nagaosa, and P. A. Lee, "Theory of the Thermal Hall Effect in Quantum Magnets," Phys. Rev. Lett. **104**, 066403 (2010).

[87] Y. Onose, T. Ideue, H. Katsura, Y. Shiomi, N. Nagaosa, and Y. Tokura, "Supporting Online Material for Observation of the Magnon Hall Effect," (2010), 10.1126/science.1188260.

[88] Y. Kagan and L. A. Maksimov, "Anomalous Hall Effect for the Phonon Heat Conductivity in Paramagnetic Dielectrics," Phys. Rev. Lett. **100**, 145902 (2008).

[89] G. Go, S. K. Kim, and K.-J. Lee, "Topological Magnon-Phonon Hybrid Excitations in Two-Dimensional Ferromagnets with Tunable Chern Numbers," Phys. Rev. Lett. **123**, 237207 (2019).

[90] R. Matsumoto, R. Shindou, and S. Murakami, "Thermal Hall effect of magnons in magnets with dipolar interaction," Phys. Rev. B **89**, 054420 (2014).